Science Bulletin 64 (2019) 1348–1380

Contents lists available at ScienceDirect

Science Bulletin

journal homepage: www.elsevier.com/locate/scib

Science Bulletin
www.scibull.com

Review

Current progress in developing metal oxide nanoarrays-based photoanodes for photoelectrochemical water splitting

Yongcai Qiu [a,b,1], Zhenghui Pan [a,c,1], Haining Chen [d,1], Daiqi Ye [a], Lin Guo [e,*], Zhiyong Fan [f,*], Shihe Yang [g,h,*]

[a] Guangdong Provincial Key Laboratory of Atmospheric Environment and Pollution Control, School of Environment and Energy, South China University of Technology, Guangzhou 510006, China
[b] State Key Laboratory of Luminescent Materials and Devices, South China University of Technology, Guangzhou 510640, China
[c] Department of Materials Science and Engineering, National University of Singapore, Singapore 117574, Singapore
[d] School of Materials Science and Engineering, Beihang University, Beijing 100191, China
[e] School of Chemistry and Environment, Beihang University, Beijing 100191, China
[f] Department of Electronic and Computer Engineering, The Hong Kong University of Science and Technology, Hong Kong, China
[g] Department of Chemistry, The Hong Kong University of Science and Technology, Hong Kong, China
[h] Guangdong Key Lab of Nano-Micro Material Research, School of Chemical Biology and Biotechnology Shenzhen Graduate School, Peking University, Shenzhen 518055, China

ARTICLE INFO

Article history:
Received 3 June 2019
Received in revised form 27 June 2019
Accepted 3 July 2019
Available online 16 July 2019

Keywords:
Photoelectrochemical water splitting
Metal oxide based nanoarray photoanodes
Preparation strategies and growth mechanism

ABSTRACT

Solar energy driven photoelectrochemical (PEC) water splitting is a clean and powerful approach for renewable hydrogen production. The design and construction of metal oxide based nanoarray photoanodes is one of the promising strategies to make the continuous breakthroughs in solar to hydrogen conversion efficiency of PEC cells owing to their owned several advantages including enhanced reactive surface at the electrode/electrolyte interface, improved light absorption capability, increased charge separation efficiency and direct electron transport pathways. In this Review, we first introduce the structure, work principle and their relevant efficiency calculations of a PEC cell. We then give a summary of the state-of the-art research in the preparation strategies and growth mechanism for the metal oxide based nanoarrays, and some details about the performances of metal oxide based nanoarray photoanodes for PEC water splitting. Finally, we discuss key aspects which should be addressed in continued work on realizing high-efficiency metal oxide based nanoarray photoanodes for PEC solar water splitting systems.

1. Introduction

Energy and environment challenges pose a growing threat to the sustainable development of mankind in the 21st century [1,2]. The current global energy consumption is still mainly dependent on the fossil fuel, which brings out the emissions of CO_2 in large quantities and consequencely promotes global warming and climate change. Global CO_2 emissions from fossil fuel use were 35.9 Gt in 2014. The world economic development has brought about a growing demand for energy. Therefore, the urgent need to find clean and renewable energy sources is of great importance for releasing sustainable developing society.

Hydrogen fuel as an energy carrier is abundant, the most efficient and produces no CO_2 emissions when used in a fuel cell [3,4]. It is not a greenhouse gas and can be generated from renewable resources. Therefore, hydrogen fuel represents one of the most promising alternatives that can simultaneously reduce a country's dependence on fossil fuels and significantly reduce environmental pollution [5–17].

2. Towards photoelectrochemical cell

2.1. The principle of photoelectrochemical cell

Solar energy as a kind of clean and renewable energy source holds the great potential for tackling the energy and environment issues in future. The solar energy irradiates the surface of the Earth (up to 1.2×10^5 TW) every year. Thus, the amount of solar energy reaching the surface of the Earth every hour can fully supply the global energy consumption over a whole year. However, the solar energy is the form of intermittency, spatial and temporal variability, and geographical dispersion, suggesting that a solar energy harvesting and storage system must be more energy efficient and cost effective.

* Corresponding authors.
E-mail addresses: guolin@buaa.edu.cn (L. Guo), eezfan@ust.hk (Z. Fan), chsyang@ust.hk (S. Yang).
[1] These authors contributed equally to this work.

https://doi.org/10.1016/j.scib.2019.07.017
2095-9273/

Photoelectrochemical (PEC) water splitting is one of the most promising ways towards solar energy utilization, which can use semiconductors to convert solar light and water to hydrogen fuel. The pioneering work in 1972 was made using TiO_2 by Fujishima and Honda [18]. A PEC cell consists of two electrodes separated by an ion-exchange membrane (Fig. 1a), where the photoanode is made of an n-type semiconductor and the photocathode is made of a dark metal electrode. The family of the PEC semiconductor materials is not very big, and the common materials and their band edge positions relative to water redox potentials are also shown in Fig. 1b. When the semiconductors are irradiated by sunlight, the n-type material is used in photoanode to produce holes for the oxygen evolution reaction (OER) (Eq. (1)), while electrons flow to the photocathode for the hydrogen evolution reaction (HER) (Eq. (2)). There are some p-type materials that have been developed to construct a tandem cell [8]. The former is a four-electron reaction, which is much more difficult than the latter with a two-electron reaction. The overall water splitting reaction is shown in Eq. (3), which is an endoenergetic reaction with a Gibbs free energy $\Delta G^0 = 237.2\ kJ\ mol^{-1}$ per mole of H_2 produced (according to the Nernst equation, $\Delta E = 1.23\ V$). In addition, the OER undergoes thermodynamic limitations, the conduction band minimum (CBM) for the semiconductor should be more negative than the H^+/H_2 energy level, whereas the valence band maximum (VBM) must be more positive than the O_2/H_2O energy level. Meanwhile, they also have intrinsic kinetic constraints and the resulting semiconductors were widely reported with absorbing photons energies greater than 2.0 eV [19,20].

$$2H_2O + 4h^+ \rightarrow O_2 + 4H^+ \quad E^0_{O_2/H_2O} = 1.23\ V\ vs.\ RHE \tag{1}$$

$$2H^+ + 2e^- \rightarrow H_2 \quad E^0_{H^+/H_2} = 0\ V\ vs.\ RHE \tag{2}$$

$$H_2O \rightarrow H_2 + 1/2O_2 \quad \Delta E = 1.23\,V \tag{3}$$

For a PEC cell, the semiconductor materials need to meet some critical requirements such as suitable band gap for optical absorption, charge transfer at the electrode/electrolyte interfaces, the catalytic behavior of the electrode materials, and appropriate valence and conduction band positions relative to water oxidation and reduction potential, high resistance to photocorrosion. Despite large efforts have been made, the reported solar-to-hydrogen efficiency (STH) efficiency is still far below the practical requirement. For example, Si and III–V compounds can achieve high photoresponse, they still suffer from photocorrosion in water electrolyte even using passivation/protection layers [10]. Metal oxides with their advantages including low cost, good chemical stability, and environmental friendliness, therefore, most of the PEC studies are mainly focused on metal oxide based photoanodes to enhance their PEC performances [21–23].

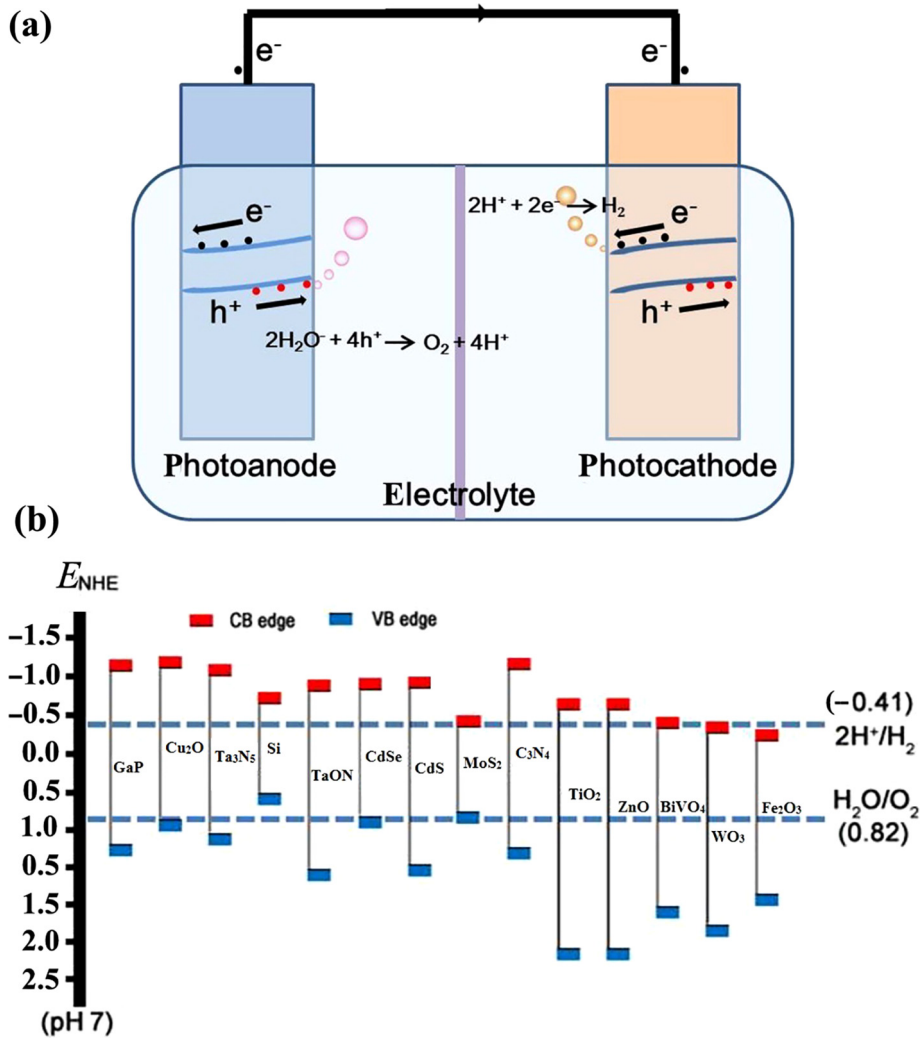

Fig. 1. (Color online) (a) Schematic diagram of a photoelectrochemical cell. (b) Band edge positions of semiconductors in contact with an aqueous electrolyte at pH 7, relative to NHE and to the vacuum level.

For metal oxide photoanodes, only few wide band-gap metal oxide materials (such as TiO_2 and ZnO) can straddle the water reduction and oxidation potentials. However, their large band gaps impose restrictions on the absorption of visible light. For the narrow band-gap metal oxides (such as Fe_2O_3 and $BiVO_4$), their CBMs are more positive than the H^+/H_2 energy level, and therefore, the external bias is needed to apply to split water. In addition, their poor electronic conductivity and short carrier diffusion length lead to significant electron-hole recombination loss. In conclusion, most of the PEC studies have been focused on addressing these limitations by various strategies such as chemically surface modifications through elemental doping, co-catalyst deposition, ultra-thin overlayer protection, anchoring organic dyes, plasmonic materials or quantum dots, as well as the nanostructuring of photoelectrode material.

There are some excellent documented review papers to address the critical issues in recent years. For example, most works about fundamental principles of PEC cells and nanostructured designs with various morphologies for enhanced PEC water splitting have been reviewed [2,21,24]. More recently, one-dimensional (1D) nanoarray structures with tailorable morphologies, elemental doping and homo/heterogeneous junction were reviewed [23,25,26]. The fundamental aspects of protection strategies and protection layer approaches and their stabilities for achieving stable solid/liquid interfaces and the charge transfer mechanism through the protection layers for both photoanodes and photocathodes have also been documented [27].

2.2. Calculation of solar-to-hydrogen conversion efficiency

To provide cross-comparisons of the performances of innovative materials, the standard calculations need to be established. In the PEC cell, several measurements have been used to declare the figures of merit of photoelectrode materials. The evaluation properties have the following parameters such as: (i) the applied bias photon-to-current efficiency (ABPE), (ii) incident photon-to-current efficiency (IPCE), (iii) absorbed photon-to-current efficiency (APCE), and (iv) solar-to-hydrogen conversion efficiency (STH).

The comparisons of ABPE and STH require that the measurements are performed under illumination by artificial light sources with an Air Mass 1.5 Global Filter at a given power density of 100 mW cm^{-2}. Usually, ABPE, IPCE and APCE are measured under applied bias in a 3-electrode PEC configuration. To unify the electrochemical parameters in the 3-electrode PEC configuration, the calculations can be addressed by referring the applied bias to the Reversible Hydrogen Electrode (RHE) according to the Nernst equation:

$$E_{RHE} = E_{ref} + E^0_{ref} + 0.059\ pH, \tag{4}$$

where E_{ref} is the measured potential referred to the used reference electrode (RE) (e.g., Saturated Calomel Electrode (SCE), Ag/AgCl, Hg/HgO, etc.); E^0_{ref} is the potential of E_{ref} with respect to the Standard Hydrogen Electrode (SHE) at 25 °C and the pH is that of the electrolyte.

Basically, the photoelectrode conversion efficiency is usually determined with external bias applying between the working (WE) and the counter electrodes (CE). The so-called ABPE for a water-splitting photoelectrode that requires an applied bias can be evaluated using the equation:

$$\mathrm{ABPE} = \frac{J_{Ph} \times (1.23 - V_{app})}{P_{light}}, \tag{5}$$

where V_{app} is the applied voltage versus RHE; J_{Ph} is the externally measured photocurrent density under bias V_{app}, and P_{light} is the power density of the illumination.

Another evaluation measurement of PEC properties of a photoelectrode material is represented by IPCE. IPCE is a measure of how efficiently the PEC cell converts the incident light into electrical energy at a given wavelength. It is usually used for understanding current generation, charge recombination, and diffusion mechanism in the PEC cell. IPCE is relative to three important efficiencies using the equation:

$$\mathrm{IPCE}(\lambda) = \mathrm{LHE} \times \eta_{cs} \times \eta_{ct}, \tag{6}$$

where LHE is light harvesting efficiency of a photoelectrode (LHE = $1 - 10^{-A}$, A is the absorbance at certain wavelengths); η_{cs} is charge separation efficiency of a photoelectrode; η_{ct} is charge transfer efficiency at the semiconductor–electrolyte interface. The measured IPCE can be expressed as:

$$\mathrm{IPCE}(\lambda) = \frac{1240 \times J_{Ph}}{\lambda \times P_{light}} \times 100\%, \tag{7}$$

where J_{ph} is photocurrent density (mA cm^{-2}), P_{light} is light power density (mW cm^{-2}) at λ, and λ is wavelength of incident light (nm).

By integrating the photoelectrode of incident photon flux density and IPCE(λ) over the wavelength (λ) of the incident light, the short-circuit photocurrent density (J_{SC}) of the PEC cell under AM 1.5 G illumination are generally calculated as:

$$J_{SC} = \int q \times F(\lambda) \times \mathrm{IPCE}(\lambda) \times \mathrm{d}\lambda, \tag{8}$$

where q is the electron charge, and $F(\lambda)$ is the incident photon flux density of AM 1.5 G at wavelength (λ).

APCE is also a powerful measurement way for determining the collected current per incident photon absorbed, which is relative to IPCE and the number of charge pairs generated per incident photon. Therefore, when referring to the Lambert–Beer's law ($A = -\log(I/I^0)$), APCE can be expressed as:

$$\mathrm{APCE}(\lambda) = \frac{J_{Ph}(\lambda)}{eI(\lambda) \times \left(1 - 10^{-A}\right)} \times 100\%. \tag{9}$$

The overall STH water-splitting efficiency of a PEC cell should be estimated under solar AM 1.5 G illumination and unbiased operation. There are three types of connections for overall PEC water splitting. One is that the photoanode and the photocathode are connected together in a short-circuited way, the other is that the photoanode or the photocathode is integrated with a photovoltaic cell to achieve a self-driven PEC cell. The STH conversion efficiency can be expressed as:

$$\eta_{STH} = \frac{J_{Ph} \times 1.23 \times \eta_F}{P_{light}} \times 100\%, \tag{10}$$

where J_{Ph} is the photocurrent density during unbiased operation, 1.23 V is the standard-state potential for water splitting, η_F is the Faradaic efficiency of evolved hydrogen, and P_{light} is the power of the incident illumination, taken here as 100 mW cm^{-2} for the AM 1.5 G spectrum at one sun intensity. η_F can be calculated by:

$$\eta_F = \frac{\text{Hydrogen evolution measured}}{\text{Hydrogen evolution based on photocurrent}} = \frac{\text{Hydrogen evolution measured}}{(J_{Ph} \times S \times t)/2F} \times 100\%, \tag{11}$$

where J_{ph} is the photocurrent density (A cm^{-2}) generated during the measurement time t (s); S is the illumination area of the photoelectrode (cm^2); F is Faraday constant (96,485.3 C mol^{-1}). The amounts of evolved gases can be analysed by gas chromatography (GC). In addition, the STH conversion efficiency can also be determined by the calculation of the amount of H_2 molecules.

$$\eta_{STH} = \frac{r_{H_2} \times \Delta G}{P_{light} \times S} \times 100\%, \quad (12)$$

where r_{H_2} is the average rate of hydrogen production (mmol s^{-1}) measured with a gas chromatograph or mass spectrometer, ΔG is the change in Gibbs free energy per mole of H_2 produced (237 kJ mol^{-1}), and S is the illuminated electrode area (cm^2).

Besides, the Mott–Schottky (MS) analysis is also an important tool to evaluate the properties of photoelectrodes. It can be commonly used to determine both dopant density and flat band potential at semiconductor/liquid contacts. In flat electrodes the capacitance per unit area of surface is expressed as:

$$\frac{1}{C^2} = \frac{2}{e\varepsilon\varepsilon_0 N_d}\left[(V - V_{FB}) - \frac{\kappa T}{e}\right], \quad (13)$$

where e is the electron charge, ε is the dielectric constant of photoelectrode material, ε_0 is the permittivity of vacuum, N_d is the dopant density, V is the potential difference across the semiconductor space charge region, V_{FB} the flat band potential, and $\frac{\kappa T}{e}$ is a temperature-dependent correction term.

When extrapolating $1/C_2$ to zero, the intercept at the X-axis corresponds to the flat band potential. The positive slope means an n-type semiconductor property, otherwise it behaves as p-type. For the dopant density (N_d), the following equation can be used for calculation:

$$N_d = \frac{2}{e\varepsilon\varepsilon_0}\left[\frac{dV}{d\left(\frac{1}{C^2}\right)}\right]. \quad (14)$$

2.3. Briefing of the review

In this Review, we first provide details about the importance of hydrogen energy. The second part is the introduction of the structure, work principle and their relevant efficiency calculations of a PEC cell. The following three parts are a summary of the state-of the-art research in the preparation strategies and growth mechanism for the metal oxide based nanoarrays. The four part gives details about the performances of metal oxide based nanoarray photoanodes for PEC water splitting, mainly including TiO_2 based photoanodes, ZnO based photoanodes, WO_3 based photoanodes, $BiVO_4$ based photoanodes, Fe_2O_3 based photoanodes. The article will end with an overall conclusion and our outlook to the future direction in the metal oxide based nanoarray photoanodes.

3. Various methodologies and mechanisms for preparation of metal oxide based nanoarrays

Metal oxide based nanoarrays are emerged as one of the most promising structures, as it can offer several advantages to boost the performances for PEC water splitting. Specifically, the kind of nanoarray electrodes can have efficient charge transfer at the semiconductor/electrolyte interface despite a short hole diffusion length because the hole only needs to diffuse across the radius of the nanoarrays. However, owing to poor optical absorption or bad chemical stability of some semiconductors, various strategies have been used to prepare the metal oxide based nanoarrays for enhanced PEC water splitting activities. In addition, the low electron mobility in metal oxide nanoarrays can be an obstacle because electrons must transport along the nanoarrays to reach the electrical contact. In this section, we will introduce the various methodologies and mechanisms developed for the synthesis of metal oxide based nanoarrays, including homo/heterogeneous branched structures and core/shell architectures. These unique structures, involving 1D nanowires, nanorods, nanotubes, nanospikes and nanocones, 2D nanoflakes and nanowalls, 3D inversed opals (IO), have been designed and prepared by a variety of techniques, ranging from vapour-phase growth, solution-based growth, and vapour-solution combination growth. The strategies can be classified into different categories as follows (Fig. 2).

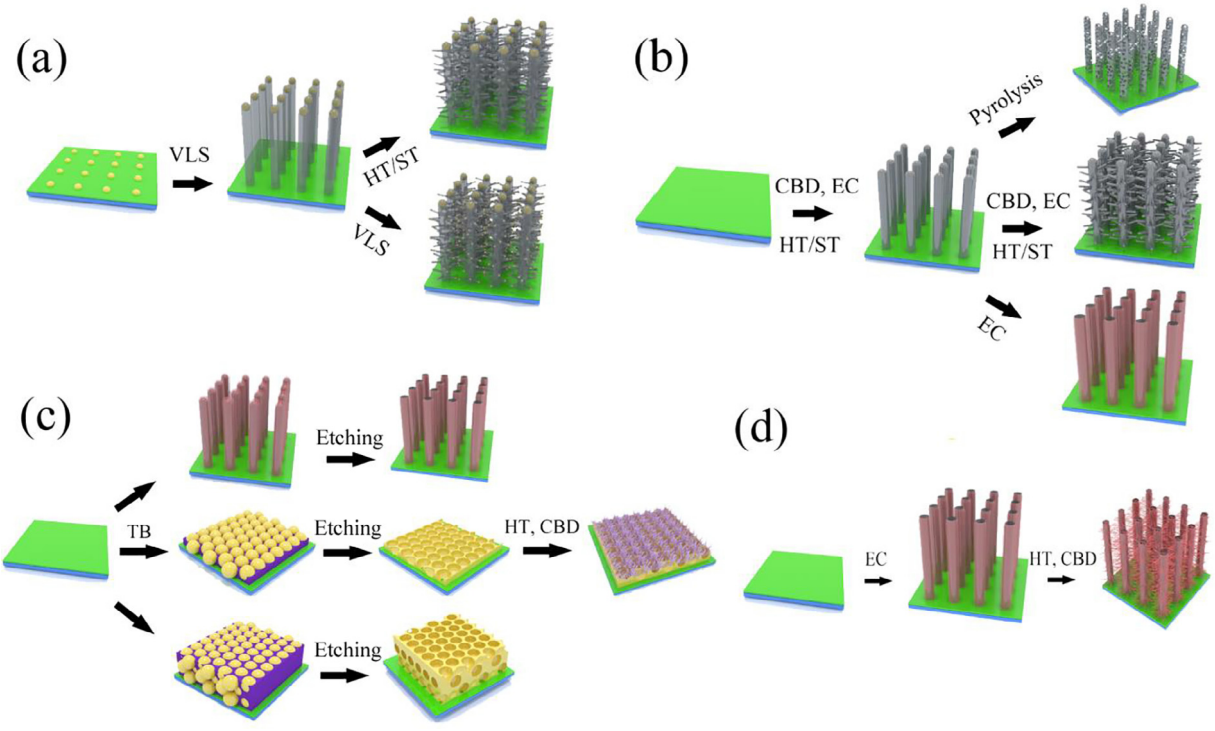

Fig. 2. (Color online) Various strategies (a–d) for preparing metal oxide based nanoarrays. VLS (vapor-liquid-solid growth), VS (vapor-solid growth), HT/ST (hydro/solvothermal growth), CBD (chemical bath deposition growth), TB (template-based growth), and EC (electrochemical growth).

3.1. Preparation of metal oxide nanoarrays

As shown in Fig. 2, the first step involved in all categories is to prepare 1D, 2D and 3D metal oxide semiconductor nanoarrays by mainly using vapor-liquid-solid (VLS) or vapor-solid (VS) growth, solid-liquid-solid (SLS) growth, hydro/solvothermal (HT/ST) growth, chemical bath deposition (CBD) growth, template-based (TB) growth, and electrochemical (EC) growth.

3.1.1. Vapor-liquid-solid (VLS) or vapor-solid (VS) growth

The VLS/VS growth has been well developed and often used for 1D metal oxide synthesis with high-quality crystallinity. Recently, several comprehensive reviews on 1D metal oxide nanomaterials synthesized by the VLS/VS growth can be found in the literature [28–35].

In 1960s, the VLS synthetic method was first proposed by Wagner and Ellis [36]. The process of the VLS method can be classified into three important steps: (i) metal alloying, (ii) crystal nucleation, and (iii) axial growth. Firstly, to form metal alloying by the VLS growth method, the proper choice of a metal catalyst is one of the important steps for growth of nanowire arrays. The selected metal catalysts should be inert and must form a eutectic mixture with the target material. In addition, they should be a low vapor pressure at the growth temperature. Therefore, gold as the catalyst is frequently used for the VLS method. In this regard, when using patterned metal catalysts on the growth substrate, nanowire arrays with different patterns can be prepared. Secondly, after alloying the metal catalyst and target material to form the liquid alloy droplet, the vapor precursor which contain the target material is easily absorbed into the droplet due to a high sticking probability and a large accommodation coefficient at the droplet surface [37]. Continuous absorption of the vapor precursor leads to achieving supersaturation. When the concentration of target material continuously increases, crystal nucleation starts at the solid–liquid interface. Finally, because the nucleation requires less energy, the further dissolution of target materials induces axial growth of nanowire arrays on the substrate. While the VS growth takes place when the nanowire crystallization originates from the direct condensation from the vapor phase without the use of a catalyst. Under high temperature condition, the source materials are vaporized and then directly condensed on the substrate in the low temperature region. The initially condensed molecules form seed crystals which serve as the nucleation sites for further condensation. The VLS/VS method presents many advantages such as production of highly anisotropic single-crystalline structures on different substrates, growth at a specific site with a uniform size and relatively mild synthetic conditions.

By using the VLS/VS growth method, for example, ZnO [34,38,39], WO_3 [40,41], Sb:SnO_2 [35,42], and Sn:In_2O_3 (ITO) [43–45] nanoarrays have been synthesized to enhance their performances for PEC water splitting. Some cases will be described in detail below. For instance, a dense ZnO nanowire array on a thick film has been homogeneously synthesized on a-plane sapphire substrates over large areas through one-step VLS growth [38,39]. The vertically aligned ZnO nanowires on the a-plane sapphire substrate have straight and smooth sidewalls. The diameter of the ZnO nanowires is uniformly distributed around 60 nm with a length of the nanowires of about 2 μm. The roots of the ZnO nanowires are electrically connected through a thick ZnO underlayer [26,27]. Similarly, Lee et al. [45] reported that ITO nanowires can be grown vertically on ITO substrates with the length up to 50 μm and the diameter of ~100 nm by the VLS method. The length of the grown ITO nanowires is almost proportional to the consumed source amount.

Additionally, by hot-filament-assisted VS growth, WO_3 nanowires array film grown on FTO substrates are typically 2–3 μm length with diameters in the range of 40–70 nm. While the morphology of some WO_3 samples grown on tungsten substrates exhibited vertically oriented platelets that are 400–500 nm wide and 80–100 nm thick. The synthesis involves the chemical-vapor transport of metal oxide vapor-phase species using air or oxygen flow over hot filaments onto substrates kept at a distance [40]. Recently, a similar synthesis, namely flame vapor deposition (FVD), has been developed by Zheng group for growing 1-D metal oxide arrays [46–50]. The method has several advantages over other physical methods: (1) high material crystallinity and purity, (2) rapid growth rates due to the high temperature achieved by flames, (3) low-cost and scalability due to the atmospheric condition, volumetric chemical heat generation, and continuous operation, and (4) great flexibility in tuning the oxidation states and morphologies of as-grown nanostructures by varying various flame synthesis parameters. In particular, they present an improved version of FVD that decouples the substrate temperature and WO_x vapor concentration, and opens up a new regime of fast, uniform and dense growth of 1-D nanoarrays at low substrate temperatures. Interestingly, the as-grown WO_3 nanowires on FTO glass substrate have a diameter down to 30 nm and a length of more than 3 μm.

Thermal oxidation VS growth method is also developed to prepare metal oxide nanoarrays on metal substrates [51,52]. The direct thermal oxidation of metals to metal oxide nanoarrays is a simple approach with large-scale growth capabilities. The first case of oxidation of metals was established in 1950s [53]. Recently, the oxidation of Fe forms α-Fe_2O_3 nanoarrays, respectively, which show potential in PEC cells [54–58]. Specifically, doped iron oxide nanoflakes grew on an FTO glass substrate can be operated at relatively low temperature (<500 °C). The procedure comprises steps of magnetron sputtering of alloyed thin film and thermal oxidation treatment in air. The hematite nanoflakes can form a large area and uniform film with a thickness of ~50 nm [57].

There are also other physical vapor deposition methods (e.g. active ballistic deposition [59,60] and oblique-angle deposition) is another very important method for vapor deposition of oxides to prepare metal oxide nanoarrays for use in PEC water splitting. For example, the high-density and aligned TiO_2 nanorod arrays with well-defined lengths were grown on ITO substrates via oblique-angle deposition. The as-obtained TiO_2 nanorods have lengths of 800–1,100 nm and widths of 45–400 nm with an anatase crystal phase [61].

3.1.2. Solid-liquid-solid (SLS) growth

For the SLS growth, it is a solution synthesis of single-crystalline III–V, II–VI, IV–VI semiconductor nanowires, which was first proposed by Buhro's group in 1995 [62]. The process of SLS method is similar to the VLS method. The difference is that the catalyst is a metal with a low melting point (<350 °C) such as In, Sn, and Bi and organometallic precursors are served as the source of the target material [28,63]. The SLS growth has been proposed to explain the formation mechanism of ZnO grown on Zn substrate [64]. The continuous oxidation growth of ZnO nuclei on ZnO substrate and a polar hexagonal and highly anisotropic crystalline of ZnO itself lead to the ZnO nanorod arrays. The nanorods are single crystalline wurtzite structure with a length longer than 10 μm. In addition, the method has been also applied to synthesis of metal chalcogenide branching onto metal oxide nanoarrays, which exhibits improved photocurrent in PEC cells [63,65].

Interestingly, without any catalysts, the electrical field can be applied to achieve the anisotropy growth. For example, Shin et al. [66] have prepared Cu_2O nanorod arrays by electrochemical flow-based solution-solid growth in a flowing electrolyte of ultra-dilute $CuSO_4$. They found that the Cu_2O nanorods can reach

4 μm in length by the prolonged deposition time up to 24 h, while the lateral growth was effectively suppressed.

3.1.3. Hydro/solvothermal (HT/ST) growth

The HT/ST growth is a general solution method of preparing metal oxide nanoarrays on various substrates for applications in PEC cells [33,34,67]. In 1845, the first case of the hydrothermal growth of crystals was reported by German geologist Karl Emil von Schafhäutl, who grew microscopic quartz crystals in a pressure cooker [68]. The reaction process involves the soluble metal salts in an aqueous/organic solution or a mixed aqueous and organic solution in an autoclave under high temperature and high pressure conditions. During the HT/ST reaction process, supersaturation can be achieved by cooling down the temperature. The crystal nucleation starts on the surface of growth substrate (with/without seeds) and subsequent oriented growth leads to the crystals alignment on the desired substrate. In general, the target nanoarrays tend to grow on its seed layer through an Ostwald ripening process and then convert a stable state with lower energy.

With the aid of the method, for instance, ZnO [69–77], TiO_2 [61,78–87], WO_3 [88–93], α-Fe_2O_3 [94–98] and $BiVO_4$ [99–101] nanoarrays have been fabricated and used in PEC water splitting cells. Specially, the ZnO nanowires can be vertically well aligned on a fluorine-doped tin oxide (FTO) glass substrate with the nanowire density of $\sim 3 \times 10^9$ wires cm^{-2}. Homogeneous growth of these nanowire arrays can be obtained in the diameters of 80–130 nm and the lengths of 1–2 μm, which depends on the growth time [70]. Additionally, the homogeneous and dense film of rutile TiO_2 nanowire arrays can be prepared on an FTO glass substrate. The as-prepared nanowire lengths are 2–3 μm, and the nanowire diameters are in the range of 100–200 nm, consisting of a bundle of smaller nanowires with diameters of 10–20 nm, which largely relies on the preparation conditions [78]. Photocorrosion stable WO_3 nanowire arrays were synthesized by the ST technique on an FTO glass. WO_3 morphologies of hexagonal and monoclinic structure, ranging from nanowire to nanoflake arrays, can be tailored by adjusting solution composition with growth along the (0 0 1) direction. The nanowire length varies from 500 to 1,500 nm, tapering in width from base (100 nm) to tip (30 nm). While the nanoflake is a thickness of 20–30 nm and a height of 1–6 μm [89].

Another hydrothermal ion exchange method is crucial for preparing metal oxide nanoarrays. Vast achievements have been made by some groups using this powerful strategy in creating inorganic nanomaterials with charming morphologies and compositions [102]. For example, Gong group describes a simple hydrothermal anion exchange method to synthesize Bi-based binary metal oxides with controlled morphologies. This synthesis process uses BiOI as the template and Bi source, which is eventually converted to Bi-based porous nanoflake photoanodes upon reaction with MO_x (M = W, V, and Mo)-containing precursors [103].

3.1.4. Chemical bath deposition (CBD) growth

The CBD growth is also a useful method that is able to grow metal oxide nanoarrays. The synthetic method requires in its simplest solution containers, which thus can be employed for large-area batch processing or continuous deposition. The growth of array thin films strongly depends on parameters like bath temperature, pH of the solution, molarity of concentration and time. The formation mechanism of the method is based on solution-solid growth, also involving two steps, nucleation and oriented crystal growth.

There are many cases with high-quality arrays that can be grown by the CBD technique. For instance, Wang et al. [104] reported different Sb_2O_3 nanoarrays, which were prepared by controlling the $SbCl_3$ concentration during the synthesis process. By controlling the $SbCl_3$ concentration during the synthesis process, dense rod-like nanobars, nanoprism arrays and needle-like nanocrystals can be observed. Oh et al. [105] reported that the ZnO nanorod arrays also can be grown on a ZnO seed layered FTO glass using the microwave-CBD method. When the growth time was prolonged from 5 to 40 min, the ZnO nanorods varied from 120 to 1,100 nm in length and 50 to 200 nm in diameter.

3.1.5. Template-based (TB) growth

The TB growth is a popular method for the preparation of metal oxide arrays for PEC use [106–114]. It employs a template on the substrate to grow/deposit the desired materials via a certain chemical or physical approach, following by removing the template. The porous anodic aluminum oxide (AAO), silica nanosphere and polystyrene (PS) nanosphere films are widely used as templates [115]. For examples, a facile method was successfully developed to fabricate TiO_2 nanotube and nanowire arrays through an AAO template-based $Ti(OC_4H_9)_4$ hydrolysis process. The wall thickness of the TiO_2 nanotubes can be controlled by adjusting the concentration of Ti $(OC_4H_9)_4$ solutions [115]. $BiVO_4$ inverse opal (IO) photoanodes were prepared by depositing a precursor solution into an assembled PS colloidal crystal template and subsequent solidification and template removal by calcination. The as-prepared $BiVO_4$ IO photoanode consisted of wormlike particles with sizes of 50–100 nm with the thickness of about 500 nm [116,117]. In the same way, the mesoscopic IO was prepared using 100 nm PS colloidal crystal templates. TiO_2 was deposited into the interstices of the colloidal crystals by CVD using $TiCl_4$ and water vapor precursors or an atomic layer deposition (ALD) technique. The TiO_2 IO structure was then obtained by removal of the polymer colloidal crystal template by calcination [106,118]. The thickness and size of TiO_2 IO structure depend on the PS template. Recently, we have tried to use an inverse nanocone AAO template to fabricate a FTO nanocone array grown on glass. The AAO template with filling with FTO nanocone array was prepared by an ultrasonic spray pyrolysis (USP) method using Sn and F salt precursor. The resultant FTO nanocone array on glass was achieved by heat treatment and subsequent template removal [119]. In the ordered structure, the cones have uniformly a bottom diameter of around 1 μm and a height of 1.5 μm with a pitch of 1.5 μm. More recently, a Nb-doped SnO_2 (NTO) nanobowl array was prepared, using a monolayered SiO_2 template formed by the Langmuir-Blodgett method. The FTO glass with the SiO_2 template was sprayed with the NTO precursor and then subjected to annealing at high temperature. The ~300 nm thick NTO bowls was obtained via calcination and SiO_2 removal [108].

Another TB growth of metal oxide arrays was achieved by the self-sacrificed template method [120,121]. In general, during forming the target materials, the template easily reacted with the precursor solution simultaneously. The result was that the tubular nanostructures were formed. In virtue of this method, ZnO nanoarrays were widely used as self-sacrificed templates for preparing other metal oxide tubular arrays. For instance, when NH_4TiF_6 and HBO_3 were selected as reagents, TiO_2 nanotubes formed with the simultaneous dissolution of the ZnO backbone [121,122]. In addition, the sol–gel reaction of a Ti precursor with a ZnO array lead to the formation of a well-aligned and freestanding TiO_2 nanotube array by controlling the rate of hydrolysis of the Ti precursor [123].

3.1.6. Electrochemical (EC) growth

The EC growth of metal oxide arrays mainly involves anodization, electrodeposition (ED) and electrochemical etching. The anodization technique is widely used because of its controllable and reproducible results, as well as the feasibility to tune the size and shape of tubular arrays. In addition, it is a cost-effective method and the nanotube arrays prepared via this method have

good adherent strength. Over the last decades, nanotube arrays such as TiO_2 [124–126], Fe_2O_3 [127–130] and Ta_2O_5 [131] have been prepared and used in PEC cells. The formation of tubular structures through electrochemical anodization is a complicated process, mainly including the following steps: (i) formation of oxide layer, (ii) pore formation and deepening of the pore, (iii) incorporation of adjacent small pores into a big pore, (iv) earlier nanotube arrays formation, and (V) formation of perfect nanotube arrays [132,133].

There are excellent review papers reported on the preparation and applications of anodic TiO_2 nanotubes [134,135]. Specifically, in a typical experiment, a clean Ti foil is anodized in a fluoride-based electrolyte using carbon rod as counter electrode under 10–60 V. Usually, acetic acid, HNO_3, H_3PO_4, H_2SO_4 or citric acid are used to adjust the acidity. The crystalline TiO_2 nanotubes are obtained by annealing at high temperature. In general, the diameter and length of the as-formed nanotubes can be adjusted over a wide range with applied voltage, electrolyte, anodization time, temperature, etc. [84,124–126,136–138]. Similarly, α-Fe_2O_3 nanotubes can be prepared by potentiostatic anodization of iron foil in an ethylene glycol electrolyte containing NH_4F and deionized water [139].

Besides the tubular structure, other morphologies and structures can be achieved by anodization technique, including nanosheets, nanowires and nanospikes. For example, Peerakiatkhajohn et al. [130] have prepared the vertically aligned α-Fe_2O_3 nanosheets on Fe foil substrates by changing anodization parameters. The nanosheets with average lateral size of around 200 nm and heights of 500–700 nm are interconnected to form house-of-cards structure.

The ED growth is also a powerful technique for synthesizing metal oxide arrays, which has been widely used in PEC cells [96,140–143]. The formation of metal oxide arrays using ED growth has the following steps: (i) nucleation on conductive substrates or on seed surfaces; (ii) oriented growth of metal oxide arrays, which depends on their intrinsic structures. Photoactive ZnO nanoarrays have been widely prepared and investigated their photocatalytic properties [144,145]. The ZnO nanoarrays formed by the ED method exhibit different shapes and morphologies by simply changing the deposition potential, deposition temperature, time, and composition of the precursor solution [146,147]. In addition, a series of *p*-type $BiOI_xCl_{1-x}$ nanoplatelets have been synthesized with the assistance of *p*-benzoquinone. The thickness of the as-obtained thin film is about 1 μm. The electrochemical reduction of *p*-benzoquinone has more positive potential than Bi^{3+} to make the electrodeposition of $BiOI_xCl_{1-x}$ possible. In the deposition process, when the *p*-benzoquinone was reduced to hydroquinone at the working electrode, it consumes H^+ ions and results in the local pH increase, which triggers the precipitation of $BiOI_xCl_{1-x}$ [148]. CeO_2 nanorod arrays grown on Ti substrates in a large scale based on a seed-assisted electrochemical growth mechanism by a facile template-free electrochemical approach. The nanorods with about 200 nm in diameter and about 7.2 μm in length grew vertically from a CeO_2 layer [149].

Electrochemical etching can be applied to grow ZnO nanotube arrays for PEC water splitting [150–152]. Briefly, ZnO nanorod arrays were firstly prepared by HT or ED methods mentioned above. The subsequent tubular morphology was formed by the proton generated from anodic splitting of water and defect-selective etching of the ZnO nanorods along the *c*-axis. The prepared ZnO nanotube arrays have a wall thickness of few tens of nanometers.

3.1.7. Precursor arrays based growth

The precursor array based growth is also a vital candidate for the formation of metal oxide arrays. The key of the method is to construct the precursor arrays. The subsequent metal oxide arrays can be obtained by heat treatment or other treatment [153,154]. For example, for the HT/ST preparation of α-Fe_2O_3 nanowire/rod arrays, in general, the FeOOH nanowire arrays were first grown on various substrates, such as Pt, W, Ti, and FTO glass, following by annealing to form α-Fe_2O_3 nanowires/rod with their (1 1 0) direction perpendicular to the substrate. The growth aqueous salt solution contains $FeCl_3$ and $NaNO_3$ or urea instead of $NaNO_3$ [155,156]. The thickness of α-Fe_2O_3 arrays formed on FTO depends on the reaction parameters. Additionally, α-$FeF_3{\cdot}3H_2O$ can be grown on FTO-coated glass in large quantity at a low supersaturation level by a facile solution growth. The subsequent thermal treatment in air leads to porous semiconducting α-Fe_2O_3 nanowires with a high aspect ratio. 150 independent measurements on the length and diameter of α-Fe_2O_3 nanowires yield an average length of (6.5 ± 2.3) μm, an average diameter of (84 ± 38) nm, and an average aspect ratio of 99 ± 70 [157]. Similarly, FeOCl nanosheet arrays were deposited on FTO glass substrates through a CVD method and further converted to porous α-Fe_2O_3 nanosheet arrays by heat treatment [158]. The thickness of the nanosheet is typically 50–60 nm, with a height of around 1 μm. After the annealing treatment, the nanosheet surface becomes much rougher with porous morphologies, mainly consisting of nanoparticles of 60 nm.

3.2. Preparation of homo/heterogeneous branching structures

A single metal oxide array structure is difficult to meet the requirements such as sufficient optical absorption and strong light trapping capability. A smart design of new architectures is of great importance for enhancing PEC water splitting performance. Compared with 1D metal oxide nanoarrays, the arrays with homo/heterogeneous branching structures are one of the promising candidate architectures due to the increased contact surface at the electrode/electrolyte interface and the direct charge carrier transport pathway in both the trunks and branches. The VLS, HT, CBD, ED methods and their combinations have been developed to prepare a wide variety of homo/heterogeneous branches on metal oxide array structures with improved PEC performance.

The preparation mainly contains three-step processes: (i) the first step is to prepare the metal oxide arrays as backbones/stems through the above-mentioned methods; (ii) the subsequent process is to generate the intermediate metal catalysts, seeds, defects on the surfaces of backbones; (iii) the final VLS, SLS, HT, CBD, ED growth of different branching structures onto the backbones are utilized. The key is the second process, which determines the quality of the branching growth. Without the intermediate metal catalysts, seeds and defects, no branches can be observed [159].

The intermediate metal catalysts are usually utilized to prepare homo/heterostructured branching arrays [160–162]. For example, a combination of the reductive successive-ionic-layer-adsorption-reaction (SILAR) and the SLS growth approach were implemented to assemble a 1D oxide-1D chalcogenide heterostructured photoactive film. Bi nanoparticles derived from bismuth precursor were used as catalysts to grow chalcogenide nanowires on anodized 1D TiO_2. The as-grown chalcogenide branched nanowires has a length ranging from 200 nm to several micrometers, depending on their growth time. The resulting "treelike" photoactive architecture demonstrates improved PEC performance [65].

The intermediate seed growth is also a popular method to prepare homo/heterostructured branching arrays [73,163–165]. The seed layers can be generated by seed nanoparticles/layers coating and precursor converted methods [54,143,163–167]. The former mainly involves spin coating, magnetron sputtering, and ALD of seed nanoparticles/layers [143,160,167,168]. For example, Ren et al. [143] studied the ZnO branching growth by various seed coating methods. They found that a ZnO nanorod cluster structure formed when a partially covered seed layer was applied to the

nanorods. On the partially covered seed layer, high solution concentrations or application of an electric field gave rise to a nanotree structure. When a completely covered seed layer was applied to the nanotrees, a nanotree structure was always formed. Kargar et al. [54] prepared ZnO/CuO heterojunction nanowire branches, where the ZnO branches were achieved by the seeding layer assisted HT method. The thin ZnO seeding layer deposited on CuO nanowire substrates was obtained through RF magnetron sputtering using a 99.99% ZnO target and in argon gas. The as-obtained ZnO branches have an average diameter of 25 nm and a length of ~ 120 nm.

The latter is that the seed layers are prepared from the different precursors, including sol solution precursors, hydrolysable compounds, and other precursors. The sol solutions are useful for the seeded growth. For instance, the ZnO sol solution (zinc acetate and ethanolamine in 2-methoxyethanol) was used to grow ZnO seed layers onto photoactive metal oxide trunks (such as TiO_2, ZnO, FeOOH, etc.) by calcination [164,165,169]. In the same way, Pang et al. [135] used the TiO_2 polymeric sol to make the TiO_2 seed layers for growing the secondary TiO_2 branches. The as-grown branches possess a cone shape with an average length of 90 nm and a base diameter around 15 nm. Heat-induced hydrolysable compounds are usually used to form seeds or direct branching growth [170]. For instance, our group used a diluted $TiCl_4$ solution that was hydrolyzed to the deposition of a dense seed layer. The subsequent HT and CBD growth leads to 3D hyperbranched hierarchical TiO_2 nanowires [171]. The as-obtained hierarchical nanowires are approximately 150 nm in length and 50 nm in diameter. The hyperbranches have an average diameter and length of about 10 and 50 nm. Wang et al. [111] reported the heterostructured TiO_2 nanorod@nanobowl arrays consisting of rutile TiO_2 nanorods grown on the inner surface of arrayed anatase TiO_2 nanobowls. The branched TiO_2 nanorods were formed through the HT growth using an aqueous mixture of tetrabutyl titanate and hydrochloric acid. After 5 h growth, both the bottom and the walls of the bowls are covered by the arrayed nanorods about 100–200 nm in width and 1–2 μm in length. The reaction involves seed nucleation and Cl-induced *c*-axis growth. The acidic precursors consisting of Fe^{2+}/Fe^{3+} salt and nitrate salt are often used to construct hierarchical heterogeneous arrays [121,169]. The thermal-induced hydrolysis will lead to FeOOH seed nucleation and subsequent growth of FeOOH nanostructures on stems. The as-grown FeOOH nanorod branches have 30–50 nm in diameter and 200–300 nm in length. The similar experiments can be also found in other reports [35,42,169,170,172]. For other precursors, for example, Zhang et al. [163] reported that a ZnS shell structure formed by ion-exchanging reaction in S^{2-} contained solution could be converted to a ZnO layer, which was served as a seed layer to grow secondary branching. The average lengths and diameters of the ZnO secondary branches were measured to be about 200 and 30 nm, respectively. ZnO spines generated by a CBD method using a stirred aqueous solution of NaOH and zinc acetate at appropriate temperature can be also acted as seeds for secondary branching growth [159,173]. After 3.5 h stirring, the lengths and diameters of the branches are ~200 and 20–50 nm, respectively. Furthermore, when these spines were acted as seeds, they can even be developed into multi-junction nanowires.

The surface defects have been well recognized for realizing the branching array structures [174,175]. It is noted that a one-pot synthesis can generate the branching structure. For example, Yang et al. [175] have grown ordered tree-like rutile TiO_2 nanoarrays on the surface of Ti film by an acid vapour oxidation method. Each of the trees can reach ca. 3 μm in height and has a diameter of ca. 280 nm. The HCl acid played an important role that it acted not only as catalyst for the generation of rutile phase but also the corrosive agent to introduce defects on the trunk. The branches form a 4-fold symmetry with the trunk due to a homoepitaxial interface originated from defects.

In general, two-step synthetic methods are usually carried out to prepare the branching nanoarrays. For instance, we have synthesized homoepitaxial ZnO nanowire/nanodisk arrays by a two-step HT method. The first HT growth generates defects on the surface of ZnO nanowires. With these surface defects, the nanodisk growth solution containing $Zn(NO_3)_2$, hexamethylenetetramine and sodium citrate can induce the secondary growth of ZnO nanodisks [73]. The as-grown nanodisks have the lateral diameter of the nanodisks of about 150–250 nm, and the thickness can be decreased to about (17 ± 5) nm through controlling the concentration of sodium citrate. Zhang et al. [176] reported the screw-like SnO_2 nanostructure formed by growing thread-like SnO_2 nanosheets (SNSs) onto rod-like single-crystalline SnO_2 nanowires (SNWs). First, the CVD growth method was used to prepare SnO_2 nanowire arrays with Au layers as catalysts. Second, the screw-threads made of SnO_2 nanosheets were prepared by a HT method. The outer diameter of the SNWs@SNSs was increased up to 300–340 nm compared to the pristine SNWs (80–100 nm). Additionally, a two-step ED growth was applied to synthesize hierarchical ZnO nanoarays [177]. Firstly, ZnO microsheets were grown on FTO substrate by cathodic deposition. And then, the hierarchical ZnO nanorod arrays were obtained through sequential electrodeposition on the FTO substrate coated with ZnO microsheets. These ZnO nanorods have a diameter of 200–300 nm and a length of about 1.7 μm. More recently, MoS_2 nanosheets were deposited on IO-$BiVO_4$ photoanode by a facile HT method. The growth solution was sodium molybdate dihydrate and thioacetamine were dissolved in deionized water [117]. After the deposition of MoS_2, the MoS_2 nanosheets are uniformly coated on the IO-$BiVO_4$ samples. The wall thickness was increased to 30 nm for the MoS_2/IO-$BiVO_4$ sample, and the pore diameter decreased to 150 nm accordingly.

Besides the above strategies, it is noted that the crystal epitaxial growth can realize the branching structures. For example, Gu et al. [166] reported that a seeded heteroepitaxial growth of ZnO nanorods can be selectively grown on TiO_2 nanorod tips by restricting crystal growth on highly hydrophobic TiO_2 nanorod film surfaces. Because the lattice mismatch between the (0 0 1) planes of rutile TiO_2 and the (0 0 2) planes of wurtzite ZnO is lower. Another case is β-FeOOH/SnO_2, which can form heteroepitaxial interface [178]. Because the (3 3 0) planes of FeOOH and the (1 0 1) planes of the SnO_2 have the lower interfacial lattice mismatch. Interestingly, the distinct crystallographic planes of SnO_2 trunk can induce different preferential growth directions of secondary FeOOH nanorod branches, leading to six-fold symmetry. The FeOOH can be transformed into α-Fe_2O_3 by heat treatment. Inspired from the idea, Sn-doped α-Fe_2O_3 nanorod branches supported on SnO_2 nanowire arrays were prepared with enhanced PEC performance [162]. The average length of the nanorods is estimated to be about 70, 130, and 160 nm for 2, 4, and 12 h, respectively. The diameter of the NRs is found to be 40, 50, and 60 nm for 2, 4, and 12 h, respectively.

3.3. Preparation of core/shell metal oxide array architectures

To increase the PEC performance and stability for solar water splitting, the core/shell metal oxide arrays with particular functions at the semiconductor–water interface are often proposed. They mainly contain the forms of type-II junction, p-n junction, Z-scheme system and hot-electron injection. Some of shell layers also play important roles in resistance photocorrosion, surface state passivation, and HER or OER activity enhancement.

3.3.1. Type-II junction

As schematically depicted in Fig. 3a, the type-II heterojunction is defined to be the staggered alignment of the energy bands at

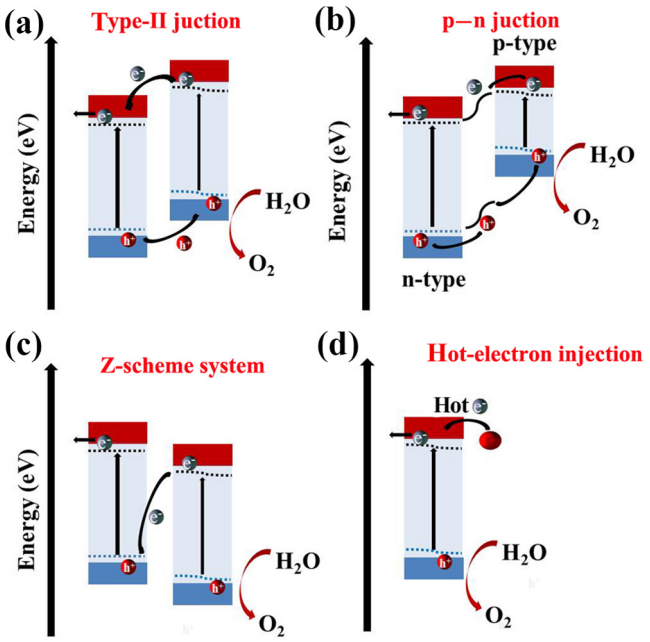

Fig. 3. (Color online) Schematic diagrams of the forms of (a) type-II junction, (b) p–n junction, (c) Z-scheme system and (d) hot-electron injection.

the interface. This type of heterojunction can reduce recombination losses and accelerate electron transport and extraction, which is beneficial to the PEC water splitting cells. To realize the heterojunction structures, solution methods including SILAR, CBD, HT, ED, ALD, ultrasonic spray pyrolysis (USP) and the combination of solution coating and subsequent calcination, have been employed usually to deposit the functional layers onto the trunk arrays [141,179].

The SILAR method is one of the most popular coating methods for achieving core/shell structures. During last two decades, the SILAR method has emerged as one of the solution methods to deposit a variety of metal chalcogenide thin films on metal oxide arrays for PEC water splitting. The SILAR method is inexpensive, simple and convenient for large area deposition. The prime requirement for obtaining good quality metal chalcogenide thin film is the optimization of preparation parameters such as concentration of the precursors, nature of complexing agent, pH of the precursor solutions and adsorption, reaction and rinsing time durations etc. [118,180–183]. CdS, CdSe, ZnS, ZnSe or their composites were usually deposited on ZnO, TiO_2 and SnO_2 arrays [73,176,182,184–187]. For example, Zhang et al. [188] reported on the preparation and PEC performance of the CdS/CdSe@ZnO core/shell nanoarrays. The photoanode comprising of a ZnO nanowire array decorated by conformal CdS/CdSe composite shells was prepared by a spin-SILAR method in which different ionic (cation: Cd^{2+}, anion: S^{2-} or $SeSO_3^{2-}$) precursors were spin-coated sequentially onto ZnO nanowire arrays without rinsing steps and the CdS or CdSe quantum dot layers were built up layer by layer. The thickness of CdS or CdSe can be controlled by changing the spin-SILAR cycles. Kim et al. [186] deposited an approximately 8 nm thick CdS layer onto TiO_2 nanowires by SILAR method, exhibiting an improved PEC water splitting performance.

The CBD and HT growth methods are also adopted to fabricate the type-II heterojunction array structures [189]. For example, the TiO_2 sheath on Sb-doped SnO_2 (ATO) nanowire array was achieved using a facile CBD method [42]. The growth solution was a $TiCl_4$ aqueous solution with high pH. The shell layer thickness increased from 10 nm at 24 h growth to 70 nm at 144 h growth. The spherical TiO_2 particles of about 3–15 nm in diameter were uniformly attached to the nanowire along its entire length. Fan et al. [189] demonstrated that the shell g-CN structure on TiO_2 nanorod arrays was achieved by ST growth. The ST reaction was implemented using 25 mL of acetonitrile as the solvent, variable concentrations of cyanuric chloride and melamine with a fixed molar ratio of 2:1 as the precursor. Zhang et al. [190] have synthesized $SrTiO_3$ shell on TiO_2 nanotube arrays by the HT method. Here, the TiO_2 nanotube arrays acted as a structure-directed template for the formation of the TiO_2–$SrTiO_3$ heterostructure. A piece of a TiO_2 nanotube array stripe was immersed in the solution of strontium hydroxide. The autoclave was sealed and placed in an oven at 180 °C for different reaction times. The $SrTiO_3$ shell was evidenced by XPS, XRD, and STEM-EDS.

ED is also a promising technique for achieving type-II heterojunction array structures [191,192]. For instance, Cu_2ZnSnS_4 nanorods modified TiO_2 nanotube arrays with enhanced visible-light activity were synthesized by using electrodeposition followed by adopting a sulfurization treatment [192].

The ALD technique can be used in the preparation of controllable ultrathin films [193]. Interestingly, the ALD coating usually forms doping at the interface after post-annealing, leading to the formation of heterojunctions [194]. For example, Liu et al. [193] have synthesized $ZnFe_2O_4$/α-Fe_2O_3 heterojunctions by depositing ZnO films on α-Fe_2O_3 nanorods through the ALD technique, followed by annealing in air. Similarly, Xi e al. [194] have fabricated the Fe_2O_3/Fe_2TiO_5 heterojunction nanorods by a sequential process of hydrothermal reaction, ALD coating, and post-annealing treatment. Here, TiO_2 thin films were deposited onto FeOOH nanorods using a home-made ALD system at 150 °C for 90 cycles, with tetrakis (ethylmethylamino) titanium (IV) and H_2O as precursors. Afterward, the FeOOH/TiO_2 nanorods were annealed in air at 550 °C for 2 h and another 10 min at 750 °C to form the $ZnFe_2O_4$/α-Fe_2O_3 heterojunction [195]. These thin film layers can be controlled from few tens of nanometers to a few nanometers. Yuan et al. [168] demonstrated that the WO_3 nanosheets were coated conformably by amorphous ZnO layers with the thickness of about 30 nm through thermal ALD at 200 °C. After further annealing in the air, the easy diffusion of Zn^{2+} ions into WO_3 lattices led to the formation of WO_3/$ZnWO_4$/ZnO heterojuctions. The intermediate $ZnWO_4$ layer is only a few nanometers in thickness.

The USP method is a simple and facile preparation method, which can be used for large-scale production of the thin shell films. The preparation requires a precursor solution, which is easily obtainable and has adjustable component content. Since we first developed this USP method to achieve uniform films of FTO and Fe_2O_3 on the periodic nanoarrays [119,196], some researchers also adopted this method to deposit other thin films to construct heterojuncion structures [197–199]. For example, Hussain et al. [197] prepared $ZnFe_2O_4$ and $NiFe_2O_4$ shells on Fe_2O_3 nanospikes by the USP method. The precursor solution contains the calculated amounts of $FeCl_3{\cdot}6H_2O$ and $ZnCl_2{\cdot}2H_2O$/$NiCl_2{\cdot}6H_2O$ in different molar ratios dissolved in ethanol. It was followed by the addition of an appropriate amount of acetyl acetone or sodium citrate as a complexing agent for making the metallic ion more volatile during the USP process. A small amount of prepared precursor solution was transferred to the evaporation chamber of USP setup, and the resulting mist was transferred to the decomposition chamber. The temperature in the chamber was kept at high temperature [197–199]. The thickness of the shell growth can be controlled by the concentration of precursor solution and deposition time.

Recently, we reported that the periodic Al/Al_2O_3/Ti/Pt/FTO core/shell nanospikes can be prepared by nanoimprint, anodization, selective wet etching, magnetron sputtering and USP. The pitch and height can be precisely controlled and it is directly related to the thickness of AAO and anodization time. The modification Ti/Pt/FTO layers have some important functionalities, including

acting as protection layers against electrolyte corrosion of the inside structure (Al and Al_2O_3), as back reflection layers to reutilize the transmission light and as electronic injection and transport layers [196]. The photonic structure is periodically adjustable, which can enhance broadband absorption of the desired photoactive layers such as TiO_2, α-Fe_2O_3 and $BiVO_4$ [29,122,200].

The process of solution coating and subsequent calcination is widely used in the synthesis of core/shell structures [193,201–203]. The coating mainly involves a mixed precursor solution and a simplex salt solution. For the former, for instance, to complete the WO_3/$BiVO_4$ core/shell nanowires, a solution containing 50 mmol L^{-1} bismuth and 46.5 mmol L^{-1} vanadium prepared by dissolving bismuth nitrate pentahydrate and vanadyl acetylacetonate in 20:1 (v/v) acetic acid/acetyl acetone was coated onto the WO_3 nanowires by drop-casting. After six cycles of coating, the sample was allowed to dry at room temperature and then briefly annealed on a hot plate at 450 °C for 2 min. Finally, they were annealed in air at 550 °C in a box furnace for 2 h. The as-formed layer has an average thickness of 60 nm [204]. Similarly, to prepare $FeVO_4$ shell layers, the 0.04 μL infiltration of the precursor solution consisting of 0.2 mol L^{-1} iron nitrate nonahydrate and 0.2 mol L^{-1} NH_4VO_3 was spin-coated on IO-$BiVO_4$, the samples were then kept under air atmosphere at 500 °C about 2 h [205]. After growing the $FeVO_4$ shell, the average wall thickness of $FeVO_4$ shell on IO-$BiVO_4$ film is ~26 nm. Concerning the latter, Hou et al. [206] have reported an $MgFe_2O_4$/Fe_2O_3 core-shell heterojunction structure achieved by a simple wet impregnation method followed by annealing. Typically, the α-Fe_2O_3 nanorod film was immersed into a 0.06 mol L^{-1} $Mg(NO_3)_2$ aqueous solution for 1 h and then dried with a nitrogen stream. Such an immersion and drying cycle was repeated three times to arrive a desired absorption amount of $Mg(NO_3)_2$ on the surface of α-Fe_2O_3 nanorods [206]. The final $MgFe_2O_4$ shell has a thickness of ~10 nm. Furthermore, wet impregnation is also usually applied to coating of quantum dots (QD) and ultrasmall nanoparticles. For example, Xiao et al. [203] reported on the preparation of the MoS_2 QDs-modified WO_3 nanoplatelet arrays photoanode, where the ultrasmall MoS_2 QDs were prepared by a spontaneous mild oxidant (H_2O_2)-triggered exfoliation process. The MoS_2 QDs transparent solution were obtained by centrifugation for several times [203]. In the same way, Hou et al. [179] coated C_3N_4 nanosheet onto WO_3 nanosheet array by wet impregnation. The C_3N_4 nanosheets was prepared by exfoliation of bulk C_3N_4 obtained from directly heating low-cost melamine.

Some physical methods such as CVD [39,207] and PVD [30,185] also were utilized to synthesize the heterojunction array structures. For example, Ai et al. [30] reported that the type-II TiO_2/CdS, TiO_2/CdTe and TiO_2/CdS_xTe_{1-x} heterostructured core/shell nanowire arrays on FTO substrates were synthesized via PVD of CdS, CdTe and the alloyed CdS_xTe_{1-x} layer onto the hydrothermally pre-grown TiO_2 nanowire arrays. Zhong et al. [39] adopted a two-step CVD method to prepare a dense array of ZnO–$ZnGa_2O_4$ core–shell nanowires. After shell coating, the average diameter of the ZnO–$ZnGa_2O_4$ core–shell nanowires was estimated to increase to about 90 nm from the initial 60 nm.

Metal-organic frameworks (MOFs) derivatives can also be used to form a heterojunction structure. For instance, Zhou et al. [208] demonstrated the sulfurization of MOFs onto the semiconductor ZnO to fabricate heterojunctions. Cellular ZnO@ZnS, ZnO@CoS, and ZnO@ZnS/CoS heterostructured catalysts can be obtained through the direct sulfurization of ZnO@zeolitic-imidazolate-frame works (ZnO@ZIFs) composites exhibit excellent PEC performances. After sulfurization treatment, the ZnO@ZnCo-ZIF was gradually etched into hierarchically structured ZnO@ZnS/CoS along with the color changes from light purple to gray, where the cellular ZnO@ZnS/CoS nanorods with the uniform structured ZnS/CoS shell were observed.

3.3.2. P-N junction

As schematically depicted in Fig. 3b, to increase the photogenerated electron–hole pairs separation efficiency of photoanodes, employing a p-n junction structure to separate the electron–hole pairs has paid great attention [209–215]. The p-n junction has been proven to be an efficient way of separating electron–hole pairs due to the built-in potential with the direction from an n-type semiconductor to a p-type semiconductor. The growth of shell layer on metal oxide arrays mainly includes HT, CBD, and ALD. For example, Yuan et al. [210] conformably grew an ultrathin and continuous coating of Cu_2O on TiO_2 nanowire array to form a truly core/shell TiO_2@Cu_2O NWA via a new facile, economical, and scalable polymer-mediated self-assembly approach, in which the polymer serves as a stabilizer, reductant, and linker simultaneously. HT was carried out to grow a Cu_2O shell around TiO_2 nanowires. The self-assembly of Cu_2O shows a highly uniform shell with a thickness of ~22 nm. Hao et al. [212] fabricated nanostructured TiO_2@-Ag_2O p-n heterojunction arrays by combining the hydrothermal method with the chemical-bath method. The Ag_2O nanoparticle shell around the TiO_2 nanowire array was achieved in an aqueous solution of silver nitrate and sodium hydroxide at 50 °C for 8 h. Huang et al. [216] coated a Co_3O_4 thin layer onto well-aligned anodized TiO_2 nanotubes via ALD. The ultrathin Co_3O_4 film uniformly coated onto the inner wall of the high aspect ratio (>100:1) TiO_2 nanotubes with film thickness precisely controlled by the number of ALD deposition cycles. The composite structure with ~4 nm Co_3O_4 coating revealed optimal photoelectrochemical (PEC) performance.

3.3.3. Z-scheme system

As schematically depicted in Fig. 3c, the Z-scheme system possesses the great potential to achieve larger separation rate of photogenerated electrons and holes. In general, the artificial heterogeneous Z-scheme consists of two different semiconductor photocatalysts with suitable band gaps and an electron mediator. However, for a photoanode comprised of a hybrid array (e.g., α-Fe_2O_3/WO_3, α-Fe_2O_3/TiO_2), its work mechanism is slightly different [217–219]. For a case of α-Fe_2O_3/TiO_2 core-shell array, when the hybrid array is irradiated, both are excited and generate photogenerated electrons and holes, respectively. The photogenerated holes on the valance band of TiO_2 rapidly transport to the surface and participate in the oxidation of water. Meanwhile, the photogenerated electrons from the conduction band of TiO_2 recombine with holes from the valance band of α-Fe_2O_3 at the interface contact, completing the relay of the called "Z-scheme". As a result, the photogenerated charge recombination can be efficiently decreased, and more photogenerated electrons on Fe_2O_3 are available to reduce H^+ to H_2, leading to the enhanced PEC performance. Recently, many "Z-scheme" nanoarray photelectrodes were made and exhibited their improved PEC performances [121,169,220]. The synthetic methods are mainly based on HT and CBD.

3.3.4. Hot-electron injection

As schematically presented in Fig. 3d, with the coating of nanometals (e.g., Au, Ag and Pt) on metal oxide arrays, the hot-electron injection mechanism was used to explain the enhanced performances of PEC cells [29,76,163,221–233]. Owning to the positive effect of surface plasmon resonance (SPR), the coherent oscillations of free conduction band electrons near metal surfaces of nanometals can be stimulated by a wide range of electromagnetic waves. The excited energy transfer from the nano-metals that could improve the absorption efficiency of the adjacent semiconductors, the hot charge injection to the semiconductor and the enhanced local electric field are responsible for the PEC performance improvement. For example, Zhang et al. [223] deposited Au nanocrystals onto the photonic structured TiO_2 nanotubes by

a facile photocatalytic reduction method, which was judiciously chosen as the plasmonic wavelength of the in situ synthesized Au nanocrystals matched the photonic band gap of the TiO_2 nantubes. Here, the Au nanocrystals essentially act as a sensitizer, absorbing resonant photons, generating the energetichot electrons from the process of the SPR excitation, and injecting them into the conduction band of the adjacent photonic structured TiO_2 nanotubes, finally leading to the enhancement of PEC performance. Chen et al. [224] fabricated Au nanoparticles sensitized ZnO nanopencil arrays by an aqueous chemical growth and subsequent photoreduction method. The distribution of the Au nanoparticles over ZnO nanopencil arrays is fairly uniform with an average diameter of (15 ± 5) nm. The deposition of Au nanoparticles not only enhances the light-harvesting efficiency caused by the SPR effect of Au nanoparticles, but also prolongs the lifetime of the photogenerated electron–hole pairs.

3.3.5. Other functionality

It is well known that the coated layer is also more frequently considered as a protective coating against photocorrosion, a passivation layer to reduce charge recombination at surface states and increase the reaction kinetics, and an electrocatayst to boost OER/HER activities (Fig. 4).

Depositing a protective coating can create a physical barrier between electrolyte and the photoactive material, which enhances the stability of photoanodes in PEC process [234–237]. In addition, some of protective layers can also play a crucial role in surface state passivation. The photogenerated holes can be easily captured by the surface states and cause significant electron–hole recombination within the space-charge layer, the passivation layer can decrease the surface recombination velocity, leading to improved PEC water splitting performances [86,136,238,239].

In order to improve stability and enhance photocurrent of the PEC cell, two strategies are usually adopted. One is to deposit a hole-conducting material that is stable in electrolyte and has a valence band level that is located between that of the photoanode and the oxygen evolution potential of water. In this case, the charge carriers can easily transfer from the bulk semiconductor to the coating layer and, subsequently, to oxidize with water in the electrolyte [240–242]. The other is to deposit the material (mostly the conducting material) with a thin layer that is thick enough to provide electrode protection but thin enough to allow tunneling of holes through it or form heterojunctions. Several efforts to improve the stability of some metal oxide arrays (e.g. ZnO) have included using protective layers of NiO_x, TiO_2, WO_3 and MOFs [114,243–245].

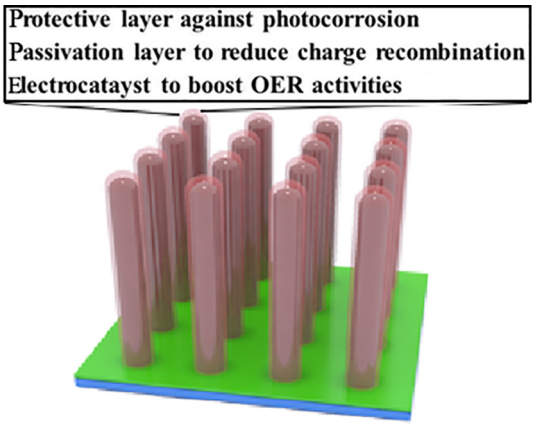

Fig. 4. (Color online) Other functionality of the coated layer.

The coating methods contain sol-gel, precursor and heat treatment, HT/ST, and CVD. For example, Hernanez et al. [246] deposited a shell of anatase TiO_2 onto an array of vertically aligned ZnO nanowires using a non-acid sol–gel synthesis solution. The TiO_2 shell with a variable thickness (between 20 and 50 nm) uniformly covering the ZnO nanowires surface, after both the air and N_2 atmosphere treatments. The ZnO@TiO_2 core–shell nanowires based photoanode exhibited improved PEC performance even working in basic media. Similar improvements were also found in other reports [75,247,248]. Carbon coating is also an alternative strategy for building up a protective layer against photocorrosion [249]. For instance, Tong et al. [250] conformably coated with an ultrathin nitrogen-doped (N-doped) carbon film on hydrogen-treated TiO_2 nanotube arrays via the carbonization of a polyimide film deposited by molecular layer deposition. The N-doped carbon film was only ~1 nm thick, which can not only provides a large heterojunction interface to substantially reduce the recombination of photogenerated electron–hole pairs, but also act as a protective film to prevent hydrogen-treated TiO_2 nanotube oxidation by electrolyte or air. Similarly, Zhang et al. [234] reported glucose as the carbon precursor coating and subsequent carbonization strategy to form a thin protective carbon layer on Cu_2O nanowire arrays. The Cu_2O nanowire arrays coated with a carbon layer of 20 nm thickness were found to give an optimal water splitting performance.

Besides the coating methods mentioned above, ALD has also been proved to be a powerful coating technique that can passivate surface states to significantly decrease the surface recombination velocity [239,251–254]. The method can achieve the thickness of the thin layer with only several nanometers. The ultra-thin coatings permit tunneling of holes or electrons. For example, Hwang et al. [238] demonstrated that an ALD coated the epitaxial of rutile TiO_2 shell on TiO_2 nanowires can increase the photocurrent by approximately 1.5 times due to reduced surface trapping. The TiO_2 shells were deposited on nanowire arrays by using a home-made ALD system at 300 °C with $TiCl_4$ and pure DI water as the precursors. Gui et al. [136] reported that the PEC performances of TiO_2 nantube electrodes with ALD-coated Al_2O_3 overlayers have systematically been functions of processing temperature and deposition cycle. The coating was performed at different temperatures (100, 200, 300, and 400 °C) using trimethylaluminum ($Al(CH_3)_3$) and DI water as the precursors. The optimized ALD coating delivered an enhanced photocurrent density by 0.8 times with respect to the pristine TiO_2 nanotube electrodes, mainly contributed by the remarkably increased photoresponse in the UV region. Li et al. [255] deposited an ultrathin TiO_2 layer on conventional hydrothermal grown hematite nanorod arrays by ALD. ALD TiO_2 was conducted on a Fiji 200 system with Tetrakis dimethylamino titanium and H_2O as precursors at 120 °C. The increased PEC performance is mainly attributed to the enhanced hole transfer via surface trap at the hematite–electrolyte interface when an amorphous TiO_2 layer is observed.

Additionally, a facile precursor-treatment approach can be an effective candidate for effective surface passivation. The approach was demonstrated by treating rutile TiO_2 nanowires with titanium precursor solutions ($TiCl_4$, $Ti(OBu)_4$, or $Ti(OiP)_4$) followed by a postannealing process, which resulted in the additional deposition of anatase TiO_2 layer on the nanowire surface. Among the three precursor-treated samples, $Ti(OBu)_4$-treated TiO_2 nanowires achieved the largest enhancement of photocurrent generation, which is approximately a 3-fold increase over pristine TiO_2 [86].

The coating of co-catalysts on the surfaces of metal oxide arrays has also attracted great interest due to its enhanced HER/OER activity [256,257]. In most cases, Ni-, Fe- and Co-based electrocatalysts have been widely used in electro-water splitting owing to their high catalytic activity, chemical stability, and low toxicity.

There are various methods to deposit electrocatalysts onto metal oxide array photoelecrodes, including HT/ST, ED, CBD, drop-casting/spin-coating [258–262]. Typically, Feng et al. [261] reported that $Ni(OH)_2$ can be decorated on the surface of H-ZnO nanorods by a CBD method. The coating is a layer of amorphous $Ni(OH)_2$ with a thickness of ~10 nm. In comparison to the pristine ZnO and H-ZnO nanorods, the $Ni(OH)_2$/H-ZnO nanorods grown on FTO glass substrates exhibit substantially higher photocurrent density.

Amongst these methods, ED is widely used to prepare coating layers on various photoanodes due to some advantages such as its simplicity, cost-effectiveness, easy control of the coating composition and forming a very uniform coating thickness without porosity [233]. For instance, Mao et al. [145] reported an effective approach to improve the PEC performance of ZnO nanorod-based photoanodes by introducing low-crystalline $Ni(OH)_2$ electrocatalyst nanosheets onto the ZnO surfaces. ZnO nanorod arrays and $Ni(OH)_2$ nanosheets were grown sequentially by ED, forming a core–shell structure. Here the wrinkled $Ni(OH)_2$ nanosheets largely increased the surface area and facilitated the PEC process by lowering the energy barrier of water oxidation and suppressing electron–hole recombination. Similarly, Shao et al. [258] prepared Co/Ni based layered double hydroxide (LDH) nanoplatelets shell on ZnO nanowires via a facile electrosynthesis method. The resulting ZnO@CoNi–LDH core–shell nanoarray exhibits promising behavior in PEC water splitting, giving rise to a largely enhanced photocurrent density as well as stability. Cobalt phosphate (Co–Pi) is photo-electrodeposited on TiO_2 nanowire arrays in Co^{2+} containing phosphate buffer. The resulting composite photoanode shows a generally enhanced photocurrent near the flat band potential region, and represents a 2.3 times improved photoconversion efficiency compared to that of pristine TiO_2 in a neutral electrolyte [263].

To further boost the PEC performances of photoanodes, the design also usually involves coating cocatalsts on various heterostructures with different functions mentioned above [29,109,179,264–267]. Typically, Peng et al. [268] fabricated the p-$LaFeO_3$/n-Fe_2O_3 heterojunction structure to improve the PEC water oxidation performance of hematite. An ALD technique is adopted to deposit La_2O_3 controllably on β-FeOOH nanorods, and the p-$LaFeO_3$/n-Fe_2O_3 heterojunction is achieved by post-thermal treatment. The heterojunction is further modified by CoO_x cocatalyst to improve the surface water oxidation kinetics.

In summary, vapour-phase and solution-phase are the two competitive methods for growing metal oxide arrays but both have their advantages and drawbacks. The former provides precise control of the structures and ordering but requires high temperatures and complicated growth equipments. The obtained structures as photoanodes exhibit enhanced PEC performances of water splitting, where a high crystalline quality and a well-defined interface is generally required. Compared to vapor phase synthesis, solution phase techniques have many advantages such as scalability, low-cost, and easy of handling. More importantly, solution synthesis methods allow for a greater choice of substrates, including both inorganic and organic substrates, since solution phase reactions occur at relatively low temperatures (25–200 °C).

4. Nanoarray photoanodes for PEC applications

4.1. TiO_2 photoanodes

TiO_2 has been widely studied as photoelectrodes for PEC water splitting since it was first used in PEC by Fujishima et al. [18] in 1972. TiO_2 naturally exhibits four different types of polymorphs, i.e., rutile, anatase, brookite, and TiO_2(B). For application, anatase and rutile polymorphs were the commonly used phases in PEC, which show the bandgaps of 3.2 and 3.0 eV, respectively. Since a large surface area is desired for enhancing charge separation and performance in PEC, TiO_2 photoelectrodes have been widely nanostructured. Among various nanostructured TiO_2 photoelectrodes, nanoarray photoelectrodes, such as nanowire-based arrays, nanotube-based arrays, and nanosheet-based arrays, are always promising because of efficient charge transport without obviously compromising surface area.

4.1.1. Nanowire-based arrays

Nanowire (NW)-based arrays are the most common kind of TiO_2 nanoarrays for PEC application, which not only offer large surface area for water splitting reaction but also provide a direct and rapid electron transport pathway toward the collection substrate. Feng et al. [269] for the first time grew single crystal rutile TiO_2 nanowire arrays on FTO glass via a non-polar solvent/hydrophilic substrate interfacial reaction under mild hydrothermal conditions. The reaction solution mainly contained containing toluene, tetrabutyl titanate, titanium tetrachloride and hydrochloric acid. The nanowires about 5 μm in length and tens of nanometers in width were densely packed which grew vertically oriented from the substrate with a preferred (0 0 1) orientation (Fig. 5a, b). The TiO_2 NW array achieved a photocurrent density of 0.8 mA cm^{-2} at 0.2 V vs. Ag/AgCl in a 1 mol L^{-1} KOH electrolyte under standard testing conditions (AM 1.5 G illumination, 100 mW cm^{-2}, Fig. 5c).

As shown above, the reported STH conversion efficiencies of TiO_2 NW arrays were much lower than the theoretical value (2%), which should be mainly attributed to the high charge recombination loss for limiting charge separation and collection efficiency. To solve this problem, Wang et al. [78] developed a hydrogenation treatment to incorporate oxygen vacancies to suppress charge recombination loss (or forming reduced TiO_2 NW arrays). The hydrogenation treatment well extended and enhanced light absorption. The photocurrent density was significantly increased, which was mainly due to the enhanced photoactivity in the UV region. Therefore, the improved charge separation and charge collection efficiency should contribute to the enhanced photocurrent. Under the optimized conditions, the TiO_2 NW arrays obtained a photocurrent density of at 1.23 V vs. RHE under standard testing conditions, affording a STH conversion efficiency of around 1.1%. Further studies indicated that the carrier densities were boosted enhanced by orders of magnitude, which could facilitate charge transport and charge separation at the interface. Chen et al. [82] have studied the nature of electron transport in the reduced TiO_2 NW arrays that was obtained by an electrochemical reduction by using intensity-modulated photocurrent spectroscopy technique. As indicated, the electron transport in pristine TiO_2 NWs displays a single trap-limited mode, whereas two electron-transport modes were detected in the reduced TiO_2 NWs, a trap-free transport mode at the core, and a trap-limited transport mode near the surface. The considerably higher diffusion coefficient of the trap-free transport mode grants a more rapid electron transport in the reduced TiO_2 NWs. Due to the significantly high PEC performance, more and more reduced TiO_2 NW arrays have been fabricated by various methods to enhance PEC performance, such as flame reduction [83], in-situ hydrothermal reduction [270].

The large bandgap of TiO_2 is the major limitations in solar energy conversion, and the theoretical solar energy conversion efficiency for rutile TiO_2 is only ~2.5% depending on its bandgap. Element doping is a typical approach to extend light absorption spectrum of TiO_2 nanowire arrays photoelectrodes into visible light region. For example, Hoang et al. [271] reported the doping of TiO_2 nanowire arrays with N element for PEC water oxidation application. N-doping was achieved by the nitridation of TiO_2 NW arrays in ammonia gas flow at temperature of 500 °C. Compared to pris-

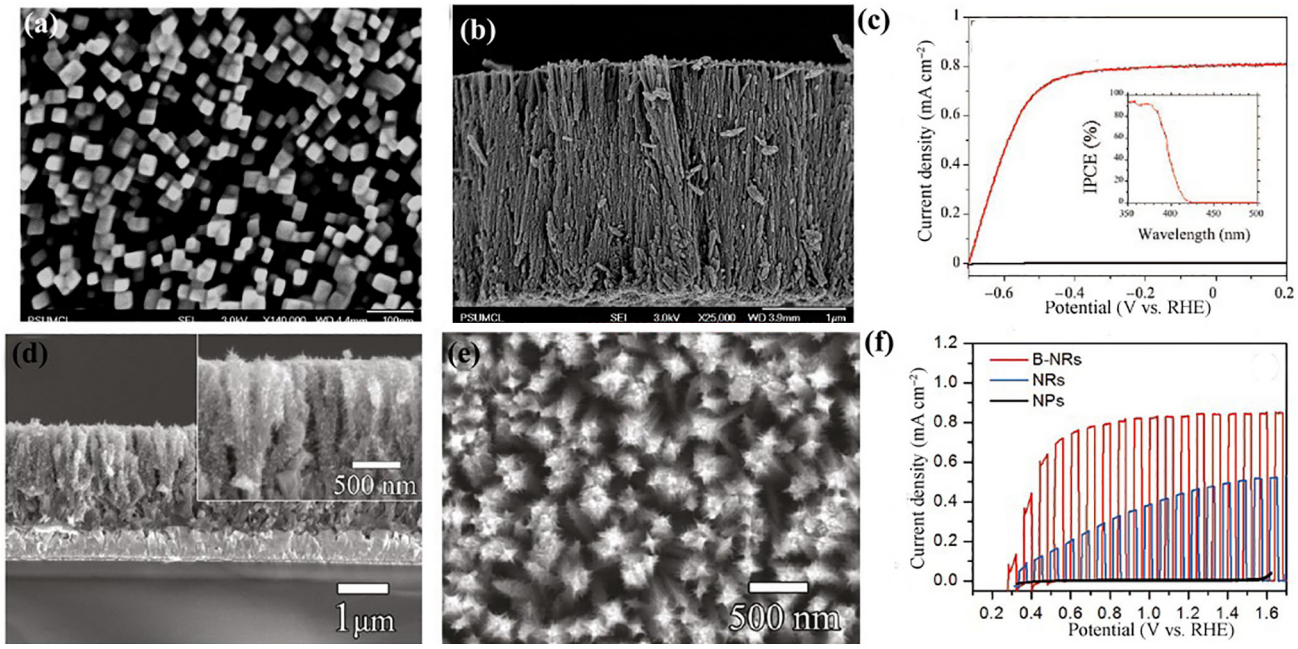

Fig. 5. (Color online) (a, b) Top-view SEM images of vertically oriented self-organized TiO_2 nanowires grown on FTO coated glass at 180 °C for 24 h. (c) Photocurrent density and photoconversion efficiency of a TiO_2 nanowire array electrode as a function of measured potential (vs. Ag/AgCl) in 1 mol L^{-1} KOH under AM 1.5 G illumination. Reprinted with permission from Ref. [269]. Copyright (2008) American Chemical Society. (d, e) SEM images of branched TiO_2 nanowire. (f) Chopped *J-V* curves under Xenon lamp illumination using three electrode setup (TiO_2 working, Pt counter, Ag/AgCl reference electrode). Reprinted with permission from Ref. [174]. Copyright (2011) American Chemical Society.

tine TiO_2 nanowire arrays, N-doped TiO_2 NW arrays extended light absorption region to 500 nm, which was attributed to the introduction of N impurity states in the electronic band structure of TiO_2. Soon after, Hoang et al. [272] reported the hydrogenation of N-TiO_2 NW arrays, which could further extend light absorption region to 570 nm and increase the PEC performance. Though N-doping could improve the visible light utilization, it might induce higher charge recombination loss in UV region, which suppresses the whole PEC performance. Besides N, many other elements have been applied to dope TiO_2 NW arrays for improving light absorption ability, including C, P, F [79,273–275], Sn [276], Fe [277], Mn [277], Co [277], Nb [278], (W, C) [279], (C, Sn) [280]. Among these doping elements, transition metals have been proved to the most effective ones. For example, Wang et al. [277] studied the Fe-, Mn-, and Co-doped TiO_2 NW arrays PEC photoelectrodes that were synthesized through a hydrothermal method. All doped TiO_2 NW arrays show obviously enhanced light absorption ability and achieved obviously higher photocurrent density. IPCE spectra indicated the doped TiO_2 NW arrays could convert the visible light (up to 570 nm) to photocurrent. Fe-doped NW arrays show the highest efficient PCE performance and the optimized Fe-doped NW arrays achieved a photocurrent density of 2.92 mA cm^{-2} at 0.25 V vs. Ag/AgCl in 1 mol L^{-1} KOH electrolyte, affording a STH conversion efficiency of 1.35%, which has been a highly promising value for TiO_2 PEC photoelectrodes.

In addition to element doping, sensitization was another effective way to increase light absorption. Plasmonic metal (such as Ag, Au and Cu) can harvest visible light due to localized surface plasmon resonance and they could can facilitate fast transfer of photoinduced electrons to TiO_2 NWs. Pu et al. [281] have used Au NPs and Au NRs to modify TiO_2 NW arrays. As indicated, Au nanoparticles could enhance electric field intensity by two and five times in magnitude at 390 and 550 nm, respectively, while Au NRs show 15 times enhancement at 750 nm. The combination of Au NPs and NRs significantly enhanced light photoactivity in both the UV and visible regions and improved the PEC performance. Until now, Au nanoparticle-modified TiO_2 NW array photoelectrodes have been well reported [282]. In addition, new attempts on other metal nanoparticles have also been studied, such as Ag [283]. In addition to plasmonic metal, dyes or semiconductors with narrow band gaps have also been used to enhance the photoresponse of TiO_2 NW arrays. The commonly used dyes for TiO_2 is Ru-based complexes [284,285], while many types of semiconductor sensitizers have been adopted, such as Ag_2O [212], $BiVO_4$ [286,287], graphitic carbon nitride [288], carbon quantum dots [289].

Though NW arrays have shown much promise in PEC, the large grain size of NWs still limits the surface area for water splitting. To address this issue, branching the NWs arrays with small crystals is a promising solution. Cho et al. [174] first branched TiO_2 NW arrays with small NRs (about 50 nm long and 10 nm wide) by a seed-assisted hydrothermal method (Fig. 5d–f). Compared to pristine TiO_2 NW arrays, the branched TiO_2 NW arrays boosted the roughness factor from 32 to 130. As a result, the photocurrent density was significantly improved from 0.31 to 0.83 mA cm^{-2} at 0.8 V (vs. RHE). Furthermore, the *J-V* curve for branch-TiO_2 NW arrays exhibited a steeper increase in current as the potential scanning in positive direction with a saturated photocurrent density at 0.6 V (vs. RHE), suggesting the much more efficient charge separation and transport. Such successful demonstration have attracted much attention and more and more branched TiO_2 NW arrays have been fabricated for PEC application. By growing omnidirectional, densely packed branches on TiO_2 nanowires, we have demonstrated a 3D hyperbranched hierarchical TiO_2 nanowire (HHNW) architecture that could significantly enhance the performance of PEC water splitting (Fig. 6). Under a solar simulator with chopped AM 1.5 G light of 100 mW cm^{-2} intensity, the HHNW electrode yielded a photocurrent density of 1.21 mA cm^{-2} at 1.23 V with respect to the RHE, which was about four times higher than that of TiO_2 nanowires (0.34 mA cm^{-2}) [171].

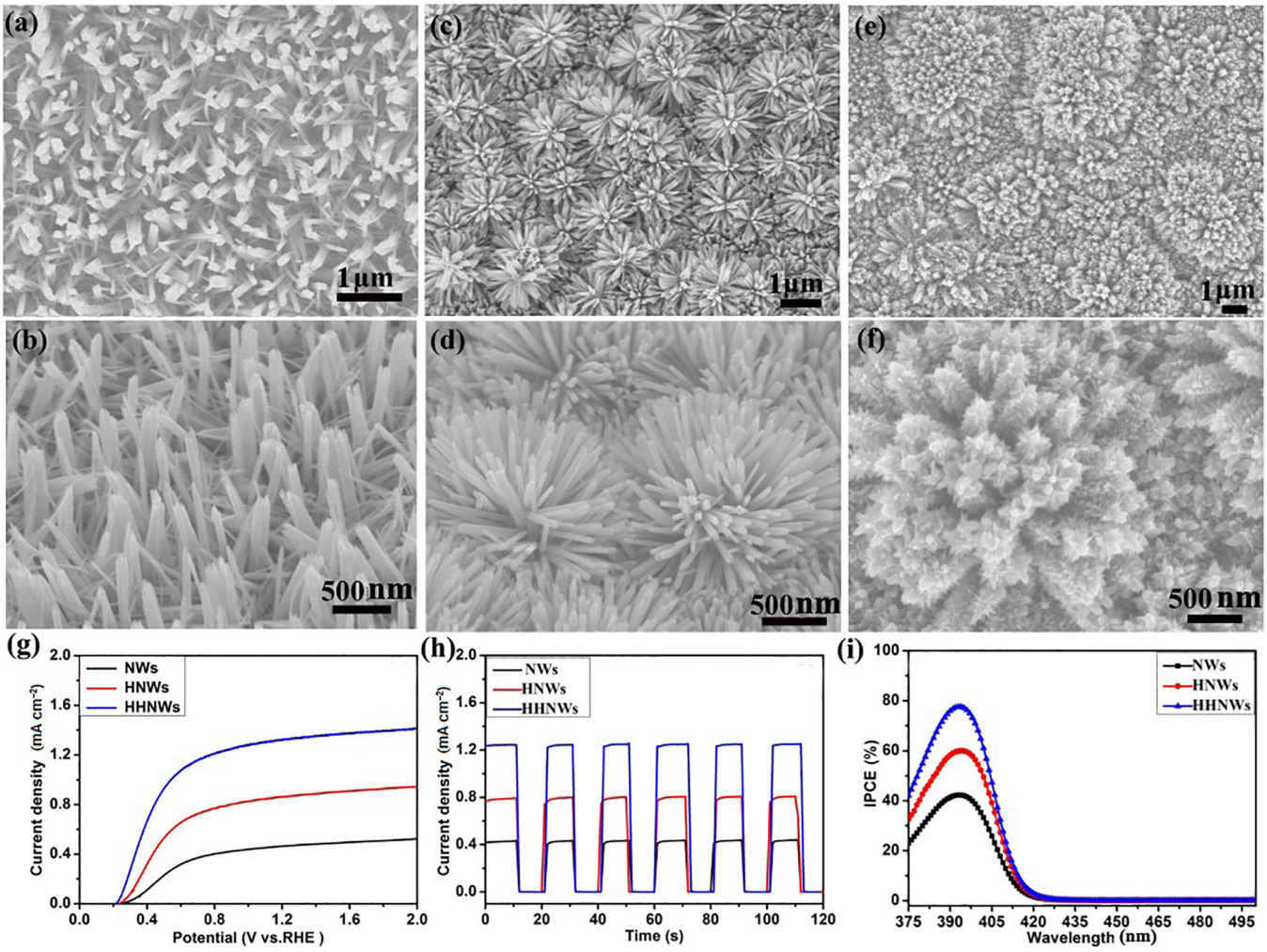

Fig. 6. (Color online) Top-view and side-view SEM images of (a and b) TiO_2 NWs, (c and d) HNWs, and (e and f) HHNWs. (g–i) Photoelectrochemical properties of NWs, HNWs, and HHNWs on FTO substrates. Reproduced from Ref. [171] with permission from the Royal Society of Chemistry.

4.1.2. Nanotube-based arrays

Compared with NW-based arrays, NT-based arrays seem to be more promising because the thin nanotube walls would enlarge surface area. Besides, NT array with the unique and highly ordered structure would enable the electrolyte to permeate the entire internal and external surfaces. Therefore, there is a constant electrostatic potential along the length of the tubes. Several methods have been developed to grow TiO_2 NT arrays, such as hydro/-solvothermal techniques [290], template-assisted methods [115,137,291,292], and electrochemical anodization [293–297]. Among these methods, electrochemical anodization is the simplest technique with strong operability in which way the desired controllable nanostructure can be grown by adjusting oxidation parameters. Assefpour-Dezfuly et al. [298] for the first time reported the growth of anodized TiO_2 NT by an alkaline peroxide treatment followed by electrochemical anodization in an electrolyte containing chromic acid. Then, Zwilling et al. [299] produced the first self-organized NT layers on Ti substrate by electrochemical anodization in a chromic acid electrolyte containing fluorine ions. So far, electrochemical anodization has been widely applied to grow TiO_2 NT arrays and most of the TiO_2 NT array photoelectrodes are based on the anodized TiO_2 NT arrays.

Grimes and co-workers for the first time reported formation of uniform TiO_2 NT arrays for PEC application via electrochemical anodization in a hydrofluoric electrolyte [294,295]. Since then, a lot of following works on TiO_2 NT array photoelectrodes for PEC applications have been reported, and most of these works have paid attention on adjusting fabrication processes to obtain optimized TiO_2 NT array photoelectrodes [297,300]. Grimes and co-workers have systematically studied the effects of the anodization voltages, times, nanotube lengths, and annealing temperatures on the PEC performance [295–297,301]. Zhang et al. [302] have optimized the hierarchical top-layer/bottom-tube TiO_2 (TiO_2 NTs) by modifying the voltages during two-step anodization. The morphologies of nanoring/nanotube, nanopore/nanotube, and nanohole–nanocave/nanotube could be finely tuned in their work. The optimized hierarchical TiO_2 NT arrays of nanopore/nanotube achieved a photocurrent density of 1.59 mA cm^{-2} at 1.23 V vs. RHE under standard testing conditions.

Doping strategy has been also used to enhance light absorption for NT array photoelectrodes. Until now, many elements have been used as dopants. N doping could be easily obtained for the anodic TiO_2 NT arrays when NH_4F-contained electrolyte was used [303]. Such N-doped TiO_2 NT arrays extended the photo-response to above 450 nm, which achieved a photocurrent density of 1.51 mA cm^{-2} at 1.23 vs. RHE the 1 mol L^{-1} KOH electrolyte. Besides, post treatment process has also been employed to introduce N element into TiO_2 NT arrays. Sun et al. [304] treated the TiO_2 NT arrays in the presence of trimethylamine in a hydrothermal process to implement N doping, while Beranek et al. [305,306]

fabricated the N-doped TiO_2 NT arrays by heat treatment in the presence of urea. As indicated, nitrogen doping not only leaded to an increase in the photocurrent for both UV and visible regions, but also significantly improves the electrode conductivity and carrier transport. Mor et al. [307] developed Fe-doped TiO_2 NT arrays by the electrochemical anodization using Ti–Fe metal as substrate. Fe doping extended light absorption ranges to 570 nm and boosted the photocurrent density to ~2 mA cm^{-2} at 0.7 V vs. Ag/AgCl in a 1 mol L^{-1} KOH electrolyte under the standard testing conditions. Park et al. [308] have reported the preparation of C-doped TiO_2 NT arrays by annealing TiO_2 nanotube arrays under controlled CO gas flow. Compared to pure TiO_2 NT arrays, C-TiO_2 NT arrays show much higher photocurrent densities and more efficient water splitting under visible-light illumination (>420 nm). Besides, other elements have also been incorporated into TiO_2 NT arrays, such as F [309], S [310], B [311], P [312], Cu [313], Cr [314,315], Pd [316].

Sensitization has also been applied to increase photoresponse in visible wavelength range. Similar to TiO_2 NW arrays, TiO_2 NT arrays have also been widely modified with noble metal nanoparticles for enhancing light utilization. Au nanoparticle is also the most widely studied noble metal nanoparticles [223,317–321]. Zhang et al. [223] coupled plasmonic Au nanocrystals on TiO_2 nanotube photonic crystal (TiO_2 NTPC). Since the SPR wavelength of Au nanoparticles matched the photonic band gap of TiO_2 NTPC, such structure significantly increased the Au SPR intensity and consequently boosted the hot electron injection. As a result, the photocurrent density was significantly improved to 2.25 mA cm^{-2} at 1.23 V vs. RHE under the standard testing conditions. Other nanoparticles, including Ag [317,322–324], Pt [325], Pd [326], have also been adopted to increase light absorption. In addition to noble metal nanoparticles, modification with narrow bandgap semiconductors have also been adopted for TiO_2 NT array photoelectrodes. Tong et al. [250] conformally coated the vertically oriented TiO_2 NT arrays with an ultrathin N-doped carbon film via the carbonization of a polyimide film. The polyimide film was deposited by a molecular layer deposition which was simultaneously hydrogenated. The core/shell nanostructure was obtained with a precisely controllable shell thickness. The thin shell layer well extended the light absorption and utilization to visible region, which significantly increased photocurrent density to 3.6 mA cm^{-2} at 0 V vs. Ag/AgCl under standard testing conditions. As graphene or carbon quantum dots can convert infrared light to visible light, and then to UV light, Zhang et al. [327] loaded carbon quantum dots (CQD) on fabricated TiO_2 NT arrays by electrodeposition, while Song et al. [328] modified TiO_2 NT arrays with graphene oxide (GO) network by a simple impregnation method. Compared with bare TiO_2 NT arrays, both CQD and GO-modified TiO_2 NT arrays could enhance light utilization and PEC performance.

4.1.3. Other nanoarrays

In addition to NW and NT arrays, TiO_2 nanocones, TiO_2 nanowalls or the integration of 1D@3D higher-order architectures was also a feasible and highly efficient strategy to obtain enhanced performance for PEC water splitting [329–331]. By using of an Al nanocone array as a substrate, a well-defined regular array of AZO/TiO_2 core/shell nanocones with uniformly dispersed Au nanoparticles (AZO/TiO_2/Au NCA) is successfully realized by Mi et al. [29] A remarkable PEC performance can be acquired and the photocurrent density of the AZO/TiO_2/Au NCA electrode reaches up to 1.1 mA cm^{-2} at 1.23 V, versus RHE under simulated sunlight illumination, which is five times that of a flat AZO/TiO_2 electrode (0.22 mA cm^{-2}). Afterward, Hoang et al. [331] reported a facile, scalable, and low cost chemical bath deposition of vertically aligned TiO_2 nanoplatelet arrays on FTO substrate. As a photoanode for PEC water splitting, the TiO_2 nanoplatelets show excellent charge separation characteristics with a saturated photocurrent of 0.4 mA cm^{-2} in 1 mol L^{-1} KOH electrolyte at 0.4 V vs. RHE. In addition, heterostructured TiO_2 nanorod@nanobowl (NR@NB) arrays consisting of rutile TiO_2 nanorods grown on the inner surface of arrayed anatase TiO_2 nanobowls are designed and fabricated as a new type of photoanodes for PEC water splitting (Fig. 7a–f). Under AM 1.5 G solar light irradiation, the unmodified TiO_2 NR@NB array photoelectrode yields a photocurrent density of 1.24 mA cm^{-2} at 1.23 V with respect to the RHE (Fig. 7g–i), which is almost two times higher than that of the TiO_2 nanorods grown directly on the FTO substrate, owing to their unique architecture that is beneficial to light harvest and charge separation and transfer [111].

4.2. ZnO photoanodes

ZnO that has similar band structure with TiO_2 is another suitable semiconductor material for PEC application. More promisingly, the electron mobility of ZnO is typically 10–100 folds higher than that of TiO_2, suggesting a much higher charge transport rate. However, due to the higher recombination rate in ZnO (excitonic emission of free exciton recombination (slow) and near surface exciton recombination (fast)), ZnO usually demonstrated an obviously lower PEC performance than TiO_2. To improve the PEC performance of ZnO photoelectrodes, various strategies have been developed. Among these strategies, nanostructuring is the easiest one to nanoarrays is still the most promising photoelectrode structure. So far, NW-based ZnO photoelectrode are the most exploited photoelectrode for water splitting application.

Many methods could be employed to grow NW-based ZnO photoelectrode, such as hydrothermal method, electrodeposition, gas reactions, oxidation of metal, vapor-phase transport via a vapor–liquid–solid mechanism, catalysis-driven molecular beam epitaxy method. However, bare ZnO NW arrays commonly exhibited significantly low photoelectrochemical performance compared with bare TiO_2 NW arrays. For example, the ZnO NW arrays with a length of 1–2 μm prepared by hydrothermal method only exhibited the current density of 17 μA cm^{-2} at 1.0 V (vs. Ag/AgCl) in a PEC cell using a solution of 0.5 mol L^{-1} $NaClO_4$ as electrolyte [70]. The ZnO NW arrays with a length of about 3.6 μm prepared by electrodeposition also obtained a relatively low PEC performance, a photocurrent density of about 20 μA cm^{-2} at 1.0 V (vs. Ag/AgCl) in a 0.1 mol L^{-1} potassium phosphate electrolyte [332]. By increasing the length of ZnO NWs to 13–14 μm, Chen et al. [73] largely promoted the photocurrent density to about 0.3 mA cm^{-2} at 1.23 V (vs. Ag/AgCl). However, the PEC performance of the bare ZnO NW arrays is still very low.

To improve the PEC performance of ZnO NW arrays, some effective strategies have been developed. For example, Yang et al. [70] doped ZnO NW arrays with N element through annealing the samples in ammonia and nitrogen atmosphere. In a PEC using 0.5 mol L^{-1} $NaClO_4$ solution as electrolyte, the ZnO:N NW arrays showed a significant enhancement in photoresponse with a photocurrent density of 400 μA cm^{-2} at 1.0 V (vs. Ag/AgCl), considerably higher than that obtained by ZnO NW arrays (17 μA cm^{-2}). The significant increase of photoresponse in the visible region well accounted for the PEC performance enhancement. Such successful doping strategy has attracted much attention, which resulted in a lots of researches on doped-ZnO NW arrays for PEC application, such as ZnO:N [333,334], ZnO:S [335], ZnO:B [336], ZnO:Co [337], ZnO:Ni [337], ZnO:K [337], ZnO:Na [337,338], ZnO: (Co, N) [339], ZnO: (Al, Cu) [340].

Surface sensitization is also an effective way to enhance the light utilization and PEC performance of ZnO NW arrays photoelectrodes. Among different sensitizers, metal nanoparticle sensitizers are of the most famous one, which not only enhanced light absorption but also improved electrical and surface properties of ZnO NW

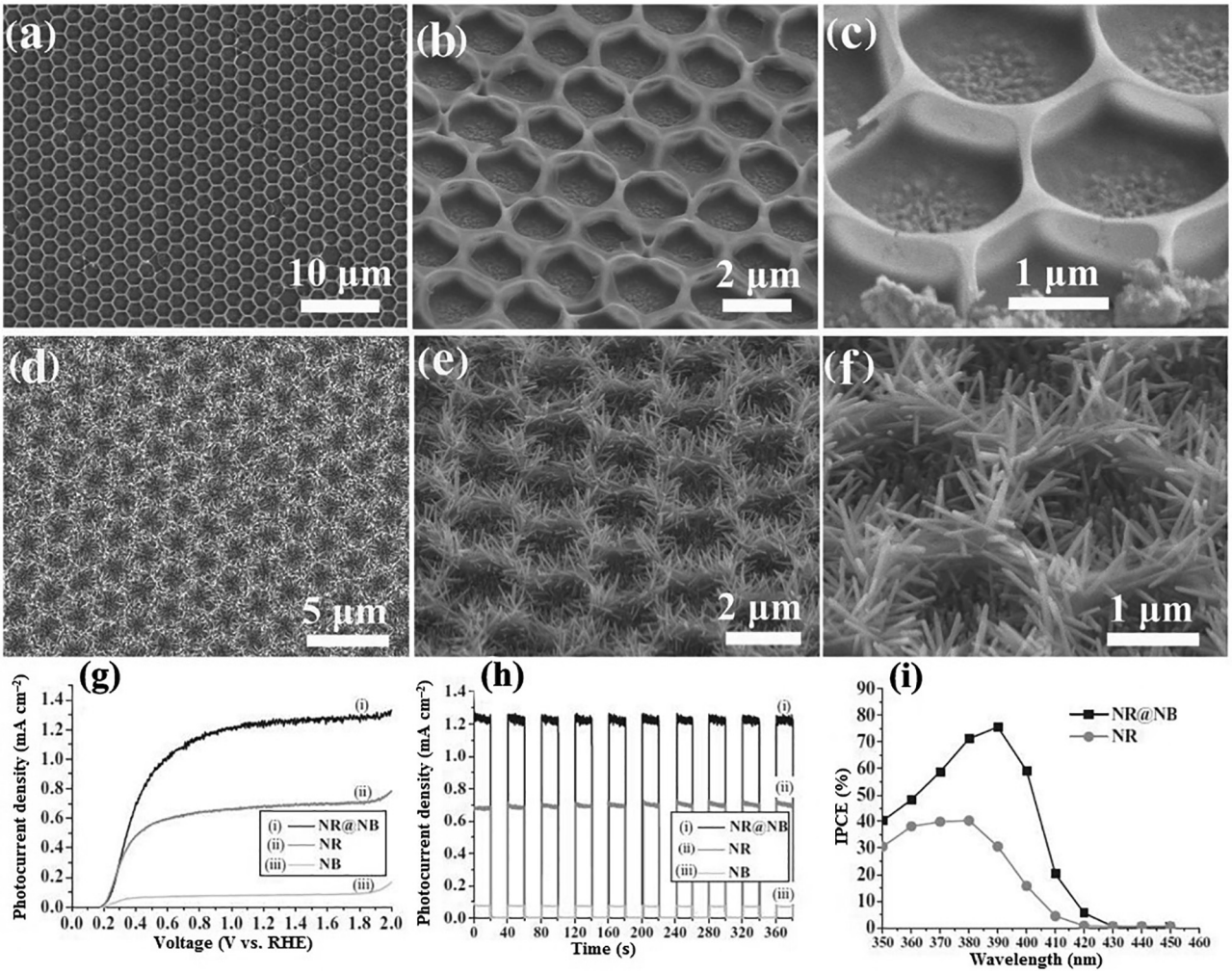

Fig. 7. SEM images of (a–c) TiO_2 NB arrays and (d–f) TiO_2 NR@NB arrays obtained after 5 h of hydrothermal growth. (g) Linear sweep voltammograms of TiO_2 NB, NR, and NR@NB array electrodes recorded in a 1 mol L^{-1} NaOH solution under simulated one sun illumination. (h) Chronoamperometric *I-t* curves for TiO_2 NB, NR, and NR@NB array electrodes collected at 1.23 V vs. RHE under AM 1.5 G illumination. (i) IPCE plots of TiO_2 NR and NR@NB array electrodes collected at 1.23 V vs. RHE [111].

arrays photoelectrodes. Wei et al. [341] applied an electron beam evaporation process to deposit Ag nanoparticles on ZnO NW arrays. For pristine ZnO NW arrays, the short-circuit current density is 0.089 mA cm^{-2}, while it is 0.325 mA cm^{-2} for the ZnO NW arrays/Ag. In addition to Ag nanoparticles [72,341], other metal nanoparticles, such as Au [342–345], Pd [342], Pt [346], have also been used enhance light absorption and photocurrent density. So far, other types of sensitizers have also been developed for the ZnO NW arrays photoelectrodes, such as CdTe [347,348], Fe_2O_3 [349], $ZnIn_2S_4$ [350], graphene quantum dots [351].

Besides enhancing light absorption, suppressing electron–hole recombination in ZnO on semiconductor surfaces by enhancing charge collection and separation is also an effective way to boost PEC performance. As a result, modifying the surface of the ZnO NW arrays with catalysts was commonly exploited to increase PEC performance. Steinmiller et al. [332] reported a photochemical deposition of Co-based oxygen evolution catalysts on ZnO NW arrays. Because both photodeposition of the Co-based catalyst and solar O_2 evolution are photo-oxidation reactions using the photogenerated holes, photodeposition inherently places Co-based OECs at the locations where the holes are most readily available for solar O_2 evolution. The catalyst not only enhanced the anodic photocurrent density of ZnO NW arrays but also shifted the onset potential of the photocurrent by 0.23 V to the negative direction, closer to the flat band potential. Until now, more and more catalysts have been deposited on the ZnO NW arrays to enhance PEC performance, such as such as Co-Pi [352], nickel borate (Ni-B) [352], $Ni(OH)_2$ [145], CoNi-LDH [353], PtO [19].

In addition to ZnO NW arrays, branched-ZnO NW arrays have also been fabricated and tested as water splitting photoelectrodes. Sun et al. [354] have reported a two-step seed-assisted hydrothermal method to grow NR branches on ZnO NW arrays. The ZnO NW/NR photoelectrode exhibited more than twice the photocurrent density of the ZnO NW photoelectrode at 1.2 V (vs. Ag/AgCl) under one-sun illumination. The highest STH value for ZnO NW/NR photoelectrode was 0.299%, obviously higher than that of ZnO NW photoelectrode (0.236%). Therefore, branched-1D nanoarrays have well proved to be promising photoelectrode structures for water splitting. Zhang et al. [163] reported a new seeding strategy to grow branches on ZnO NW arrays (Fig. 8). Firstly, ZnO NW arrays were immersed into 1 mol L^{-1} Na_2S aqueous solution for 3 h to form a ZnS shell layer on ZnO NWs, followed by annealing at 500 °C for 5 h in air to convert the ZnS shell layer into ZnO seeds. Subsequently, the annealed samples were used as substrates for the second hydrothermal growth of nanorod branches on ZnO NWs, in which the aqueous growth solution contained zinc nitrate hydrate (25.0 mmol L^{-1}), hexamethylenetetramine (12.5 mmol L^{-1}), polyethylenimine (5.0 mmol L^{-1}) and aqueous ammonia

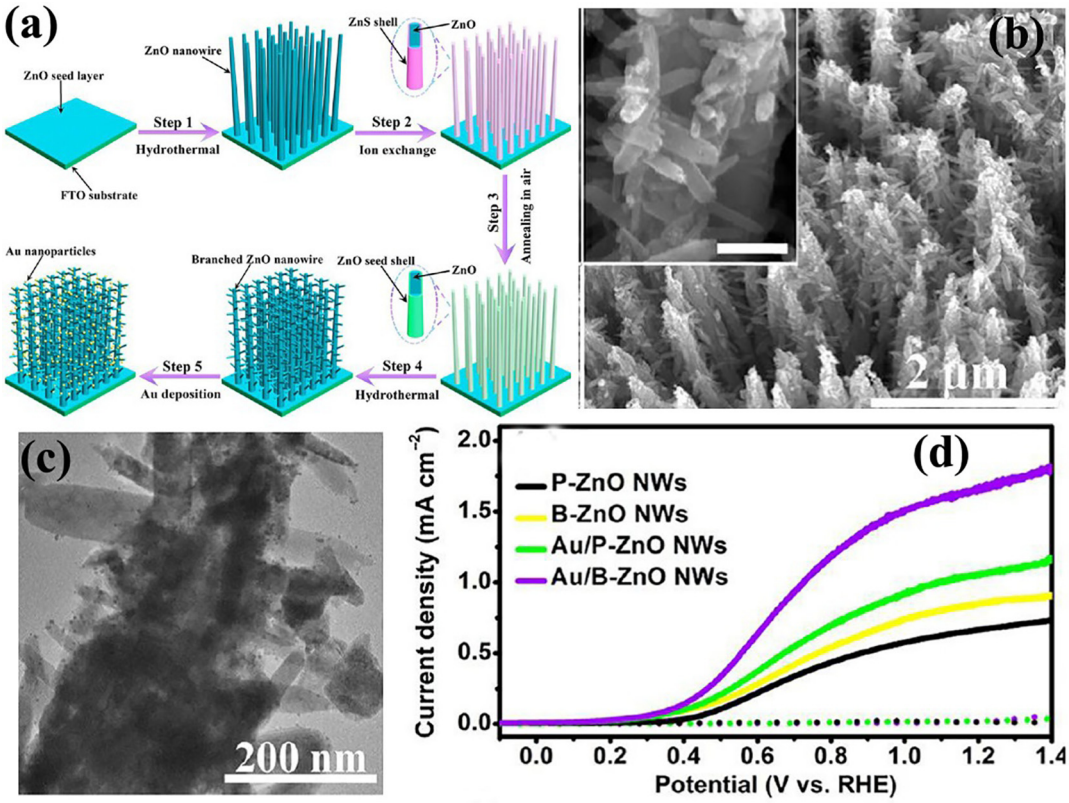

Fig. 8. (Color online) (a) Schematic diagram of the main processes for the fabrication of Au NPs modified B-ZnO NWs arrays photoelectrode. (b) Titled 30° view SEM images of Au NPs modified B-ZnO NWs arrays. (c) Low-magnification TEM images of Au NPs modified B-ZnO NWs. (d) Linear sweep voltammetry of these photoanodes in darkness (dotted lines) and under illumination (solid lines). Reprinted with permission from Ref. [163]. Copyright (2014) American Chemical Society.

(0.5 mol L^{-1}). In a photoelectrochemical cell with a Pt wire, an Ag/AgCl electrode and a 0.5 mol L^{-1} Na_2SO_4 aqueous solution as counter electrode, reference electrode and electrolyte, respectively, the ZnO NW/NR electrodes obtained a photoconversion efficiency of 0.24%, much higher than the ZnO NW photoanodes. Similar to ZnO NW arrays, several strategies have also been employed to promote the PEC performance of branched ZnO NW arrays. For sensitization, Au nanoparticles [163], have been investigated as sensitizers. Though branching NW arrays was an effective approach to promote water splitting performance. However, grain boundaries were present between the trunks and branches, which still limited the charge transport rate. To solve this problem, Chen et al. [73] have exploited an epitaxial growth strategy to eliminate the grain boundary between trunk and branches (Fig. 9). That is, after the growth of ZnO NW arrays, ZnO nanodisks (NDs) were epitaxially grown on the NWs. Such structure well increased the surface area of photoelectrode and enhance light absorption capacity without obviously compromising electron transport rate. The exposed polar facet of ZnO ND further favor the charge separation at the interface, which finally largely improved the PEC performance.

4.3. WO_3 photoanodes

WO_3 exhibits absorption of approximately 12% of the solar spectrum with a band gap of 2.5–2.8 eV, a moderate length of hole diffusion (150 nm) and an electron transport ability of 12 $cm^2 V^{-1} s^{-1}$. As a photoelectrode, WO_3 can achieve a maximum theoretical conversion efficiency of about 4.8%. Though the VB edge position of WO_3 is positive enough for the water oxidation, but its CB is not negative than the H^+/H_2 redox potential. Hence, oxygen can be easily produced, but H_2 can only be generated with the assistant of external bias potential. Similar to TiO_2 and ZnO photoelectrodes, photoelectrode nanostructuring has also been widely employed to improve the PEC performance of WO_3 photoelectrodes, and the photoelectroedes with various nanoarray structures have been well developed.

4.3.1. Nanowire-based arrays

WO_3 NW-based arrays can prove a promising material with which to achieve efficient water photoelectrolysis, as they can offer photogenerated charges direct electrical pathways, with reduced grain boundaries, resulting in superior charge transport properties. Kalanur et al. [355] have prepared WO_3 NW arrays by orthorhombic $WO_3{\cdot}0.33H_2O$ NW arrays as precursors. $WO_3{\cdot}0.33H_2O$ NW arrays were first prepared by a hydrothermal method using an aqueous solution containing ammonium paratungstate, HCl and H_2O_2. After post annealing at 400 °C, $WO_3{\cdot}0.33H_2O$ was converted to hexagonal phase WO_3, while post annealing above 500 °C, monoclinic WO_3 NW arrays were obtained, which is the photoactive phase for water oxidation. Such WO_3 NWs show a single-crystalline structure. The WO_3 NW array photoanode in 0.5 mol L^{-1} Na_2SO_4 exhibited a photocurrent of 2.26 mA cm^{-2} at 1.23 V (vs. RHE) under AM 1.5 G illumination, which produced an IPCE of about 35% at 400 nm. In addition to hydrothermal method, Ding et al. [356] have employed a flame vapor deposition (FVD) technique to grow WO_3 NW arrays. By simply adjusting the growth duration, the length of the NW arrays could be well controlled. For photoelectrochemical cell application, the optimum length was 7.2 μm, which achieved the best water splitting performance, with a photocurrent density of 2.25 mA cm^{-2} (at 1.7 V vs. SCE). Kafizas et al. [357] have applied a CVD technique to synthesize monoclinic WO_3 NW arrays with needle shape at atmospheric pressure, which were highly oriented in the (0 0 2) plane, with the nanoneedle

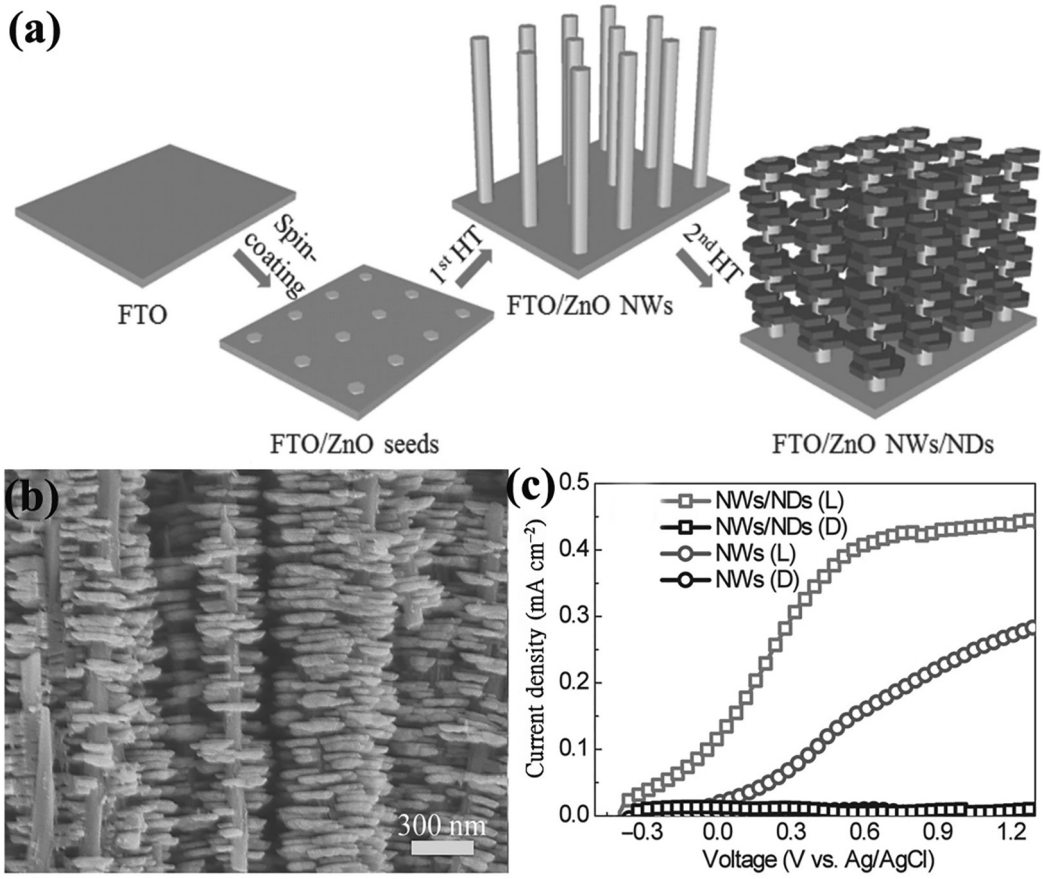

Fig. 9. (a) Schematic illustrating the preparation processes of ZnO NWs/NDs. (b) Close-up cross-sectional image of the as-prepared ZnO NWs/NDs. (c) *J-V* curves of ZnO NWs/NDs and ZnO NWs obtained under dark (D) and light illumination (L) conditions [73].

structures stacking perpendicular to the FTO substrate. The optimized photoanode consists of a ~300 nm WO_3 seed layer and a ~5 μm thick top layer of WO_3 NW arrays. After being applied in photoelectrochemical cells, such photoanode produced a photocurrent density of 1.24 mA cm^{-2} at 1.23 V vs. RHE with the IPCE values of ~35%–45% in the wavelength of 250–375 nm.

Similar to TiO_2 and ZnO, branched WO_3 NW arrays were also reported as photoelectrodes. Zhang et al. [358] reported the WO_3 NW/NR arrays by using $(NH_4)_{0.33}{\cdot}WO_3$ NW/NR arrays as a precursor, which was prepared by a hydrothermal method with ammonium oxalate as a capping agent. The synergistic interaction between ammonium ion (NH_4^+) and acetate ion (–COO–) was proved to the formation mechanism of $(NH_4)_{0.33}{\cdot}WO_3$ NW/NR arrays. After annealing, $(NH_4)_{0.33}{\cdot}WO_3$ NW/NR arrays were converted to WO_3 NW/NR arrays with good morphology preserving. Compared with WO_3 NW arrays, the WO_3 NW/NR arrays showed higher PEC activity, with a maximum photocurrent density of 1.3 mA cm^{-2} at 1.3 V vs. Ag/AgCl. Such high performance improvement was owing to the better light-trapping capability and the increase in active area. Liu et al. [359] have also reported the $(NH_4)_{0.33}{\cdot}WO_3$ NW/NR arrays by one-step hydrothermal method in the reaction solution containing ammonium wolframate, lactic acid, ethanol and L-glutathione reduced ($C_{10}H_{17}N_3O_6S$). After annealing, $(NH_4)_{0.33}{\cdot}WO_3$ was converted to WO_3, but the structure of NW/NR arrays was destroyed and the photoelectrochemical performance of WO_3 electrode was low.

4.3.2. Nanosheet-based arrays

Nanosheet-based arrays have also been widely investigated as the photoelectrodes in PEC cells [360]. Amano et al. [361] for the first time reported the perpendicularly oriented plate-like WO_3 nanostructure on FTO glass by using $WO_3{\cdot}H_2O$ NS arrays as precursor. The $WO_3{\cdot}H_2O$ NS arrays were grown by a solvothermal method in an ethanol solution of WCl_6, which were converted to WO_3 NS arrays by post annealing in air. The WO_3 NS arrays structure was preserved after annealing with the NS thickness of from ca. 95 nm to ca. 80 nm. As a photoelectrode in photoelectrochemical cells, the WO_3 NS arrays exhibited a photocurrent density of around 1.7 mA cm^{-2} at 1.0 V vs. Ag/AgCl in an aqueous electrolyte of 0.1 mol L^{-1} Na_2SO_4. For further improving the performance of WO_3 nanoflakes based electrode, Wang et al. [360] prepared hydrogen-treated WO_3 nanoflakes. Compared to pristine WO_3, the hydrogen-treated WO_3 nanoflakes show an order of magnitude enhanced photocurrent, and more importantly, exhibit extraordinary stability for water oxidation without loss of photoactivity for at least seven hours (Fig. 10a–c). Zheng's group also developed a postgrowth modification method of two-dimensional WO_3 nanoflakes by a simultaneous solution etching and reducing process in a weakly acidic condition (Fig. 10d–f) [93]. The obtained dual etched and reduced WO_3 nanoflakes have a much rougher surface, in which oxygen vacancies are created during the simultaneous etching/reducing process for optimized PEC performance. The obtained photoanodes show an enhanced photocurrent density of ~1.10 mA cm^{-2} at 1.0 V vs. Ag/AgCl, compared to 0.62 mA cm^{-2} of pristine WO_3 nanoflakes. In addition to exploiting $WO_3{\cdot}H_2O$ NS arrays as precursor, W-Fe amorphous NS arrays were electrodeposited and used as precursor for growing WO_3 NS arrays [362,363]. After dealloying in a dilute HNO_3 solution (3.5 wt%) and post annealing in air at 500 °C, WO_3 NS arrays were obtained. In a PEC cell with H_2SO_4 (0.5 mol L^{-1}) as electrolyte, the WO_3 NS

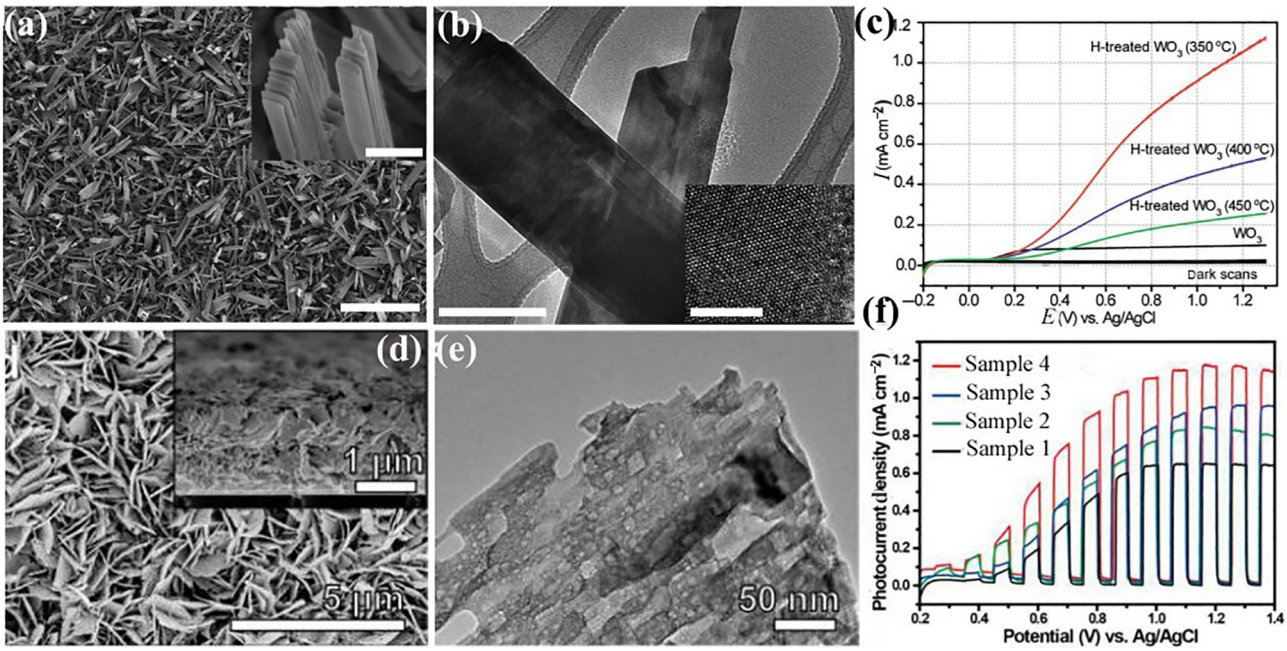

Fig. 10. (Color online) (a) SEM image of WO_3 nanoflakes. (b) TEM images of WO_3 nanoflakes (scale bar: 100 nm). (c) Representative *I-V* curves measured under 100 mW cm^{-2} simulated solar light. Reproduced from Ref. [360] with permission from the Royal Society of Chemistry. (d, e) SEM and (f) HRTEM images of the dual etched/reduced WO_3 nanoflakes. (f) Photocurrent density curves of four types of WO_3 nanoflakes. Reprinted with permission from Ref. [93]. Copyright (2014) American Chemical Society.

arrays achieved a photocurrent density of 2.25 mA cm^{-2} at a bias potential of 1.5 V (vs. SCE) under light illumination of 100 mW cm^{-2}.

In addition to exploiting other NS arrays as precursor, a direct growth of WO_3 NS arrays by hydrothermal methods have also been well developed. Su et al. [89] reported the deposition of WO_3 NS arrays by a hydrothermal method in the acetonitrile solution containing H_2WO_4, oxalic acid, urea and HCl, or the acetonitrile/water solution containing H_2WO_4, oxalic acid and HCl. The WO_3 NS arrays were grown along the (0 0 1) direction by this hydrothermal method. In the PEC with an aqueous solution of 0.1 mol L^{-1} Na_2SO_4 as electrolyte, the WO_3 NS arrays obtained from the acetonitrile/water solution achieved a higher performance with the IPCE values higher than 60% at 400 nm with a photocurrent density of 1.43 mA cm^{-2} under AM 1.5 G illumination. Wang et al. [364] reported a facile 2-step hydrothermal method to grow oriented WO_3 NS arrays in an aqueous precursor solution containing $Na_2WO_4{\cdot}2H_2O$, $H_2C_2O_4{\cdot}2H_2O$ and HCl. By halving solution volume and applying a two-step strategy, the WO_3 NS arrays with (0 0 2) oriented facets were tailored to obtain the preferential growth of WO_3 NS arrays with enriched (0 0 2) facets. These WO_3 NS arrays with enriched (0 0 2) facets exhibited extraordinary PEC performance with a remarkable photocurrent density of 3.7 mA cm^{-2} at 1.23 V vs. RHE under AM 1.5 G illumination, corresponding to ~93% of the theoretical photocurrent density of WO_3 materials. Through combining experimental studies and density functional theory (DFT) calculations, it was revealed that the enhanced photocatalytic activity and photostability of the WO_3 photoelectrodes were attributed to the synergistic effect of highly reactive (0 0 2) facet and NS structure, which promoted charge separation and suppressed the formation of peroxo-species.

The size of the above WO_3 NS is usually large, which would limit the active area of water oxidization. To solve this problem, Li et al. [93] developed an etching strategy to create nanopores in the WO_3 NS by treating the as-deposited WO_3 NS arrays in an aqueous solution containing poly(vinyl pyrrolidone) and ascorbic acid. The obtained WO_3 NS arrays have highly porous structure with a much rougher surface. In addition, a large amount of oxygen vacancies are created during etching. The obtained photoanodes show an enhanced photocurrent density of ~1.10 mA cm^{-2} at ~1.23 V vs. RHE, compared to 0.62 mA cm^{-2} of pristine WO_3 NS arrays.

4.3.3. Other nanoarrays

In addition to NW and NS arrays, some other WO_3 nanoarrays have been also fabricated and applied in PEC, such as NT arrays, nanoflower arrays, nanotree arrays. Rao et al. [41] have synthesized WO_3 NT using FVD method. By controlling the substrate temperature in the range of 530–700 °C, uniform and densely packed WO_3 single and multi-shell NTs, and NWs arrays could be obtained. Due to high areal number density WO_3 NT arrays, such FVD-grown WO_3 NT arrays could efficiently absorb light. As a result, they show superior water splitting performance in photoelectrochemical cells, which generated a maximum photocurrent density of 2.2 mA cm^{-2} at 2 V vs. Pt in 0.5 mol L^{-1} H_2SO_4, with a ABPE η of about 0.21%. The high performance should be assigned to the ability of WO_3 NT arrays to orthogonalize the directions of light absorption and charge transport, which hence leaded to both efficient light absorption and charge carrier collection. Wang et al. [365] have prepared WO_3 nanoflower arrays by a microwave-assisted hydrothermal method in the presence of a series of RCOO- as capping reagents in acidic conditions. The capping reagents of RCOO- served to regulate the uniform architecture of nanoflowers. Without capping agents, only irregular block-like shape was obtained. In the PEC with 1 mol L^{-1} H_2SO_4 as electrolyte, the well oriented WO_3 nanoflowers arrays achieved a higher photocurrent density of 1.3 mA cm^{-2} at 1.4 V vs. SCE, which is much higher than that obtained with irregular block-like photoelectrode. Balandeh et al. [366] have grown WO_3 nanotree array by pulsed laser deposition through a self-assembly process from the gas phase. As a photoelectrode in PEC, the WO_3 nanotree array exhibited an onset potential as low as 0.4 V vs. RHE and a saturation

current density up to 1.85 mA cm^{-2} at 0.8 V vs. RHE. This peculiar performance was attributed to the hyperbranched structure and the excellent optical/electronic properties. Soon after, Shin et al. [367] also reported a WO_3 nanotree array by using a pulsed laser deposition method. Adjusting the oxygen partial pressure during the deposition process well controlled the porosity of the WO_3 nanotree array. The partially preferred alignment of the individual WO_3 nanocrystals greatly improved the charge transport property of the WO_3 nanotree array. Under simulated solar light illumination, such photoelectrode achieved a photocurrent density of 1.8 mA cm^{-2} at 1.23 V vs. RHE, which is 9 times higher than that of a dense WO_3 photoanode.

4.4. $BiVO_4$ photoanodes

$BiVO_4$ with a favorable bandgap of 2.3 eV for efficient light absorption is one of the most promising PEC photoelectrode materials. As the CB is close to 0 V vs. RHE at pH = 0, due to the overlap of empty Bi 6p orbitals with anti-bonding V 3d-O 2p states, the external bias needed for water splitting is well reduced. As a result, its theoretical STH efficiency is as high as 9.2% with a photocurrent density of 7.5 mA cm^{-2} under AM 1.5 G illumination. However, electron transport in $BiVO_4$ is very poor owing to the high recombination rate, affording a short carrier diffusion length of only 70 nm. Besides, hole transfer from $BiVO_4$ to electrolyte is slow. These two drawbacks significantly limited the PEC performance of $BiVO_4$ photoelectrode. So far, many strategies have been employed to improve PEC performance, such as doping, coating catalysts, electrolyte design, developing heterojunction, facet selective deposition, nanostructuring. Among these approaches, nanostructuring has been widely adopted, which would not only offer large active area but also preserving high carrier transfer rate.

4.4.1. Nanowire-based arrays

Due to the short electron transport length, NW or NR arrays are favorable for electron transport in photoelectrodes. However, there are only a few works have been made on the synthesis of $BiVO_4$ 1D nanoarrays. Su et al. [99] have for the first time reported the growth of $BiVO_4$ NW arrays on FTO glass by a seed-mediated growth method in an aqueous suspension. The seed layer was deposited by spin coating an aqueous $BiVO_4$ precursor solution. The $BiVO_4$-coated FTO glass was immersed in a $BiVO_4$ aqueous suspension solution for the growth of $BiVO_4$ NW arrays at the temperature of 40–90 °C. The suspension solution mainly contained $Bi(NO_3)_3$, NH_4VO_3, HNO_3, $NaHCO_3$. The obtained NWs that vertically oriented on the FTO glass show a pyramidal shape. As a photoelectrode in PEC, the $BiVO_4$ NW arrays achieved a photocurrent density of 0.4 mA cm^{-2} at 1 V vs. Ag/AgCl in a 0.5 mol L^{-1} Na_2SO_4 solution. Xiao et al. [101] have applied the similar procedure to grow $BiVO_4$ NW arrays. After optimizing the grow temperature and duration, the photoelectrode obtained a photocurrent density of 0.12 mA cm^{-2} at 1.23 V vs. RHE in a PEC using an aqueous solution containing 0.5 mol L^{-1} Na_2SO_4 as electrolyte. Compared with the state-of-art nanoporous photoelectrodes, the PEC performance obtained by the $BiVO_4$ NW arrays is significantly lower. Some studies indicated that reducing $BiVO_4$ nanosize to be below its hole diffusion length would significantly enhance electron–hole separation [368,369]. Therefore, reducing the diameter of $BiVO_4$ NWs is important to achieve high PEC performance. However, no successful method has been developed for growing thin NWs.

To solve the above problem, some works aimed to make the NWs porous, which preserved the NW structure and reduced the grain size to favor hole transfer. Yoon et al. [287] prepared the $BiVO_4$ NWs with highly porous structure by an electrostatic spray deposition technique. The spray solution contained $BiN_3O_9{\cdot}5H_2O$, $C_{15}H_{21}O_6V$ and CH_3COOH. The NWs were consisted of the nanoparticles about 100 nm in size. After careful optimization on deposition duration, the $BiVO_4$ NWs photoelectrode achieved a photocurrent density of 1.3 mA cm^{-2} at 1.2 V vs. Ag/AgCl. Liu et al. [370] utilized a multistep ion exchange approach to construct the $BiVO_4$ electrodes having a nanorod structure with high porosity. Firstly, SnS_x nanosheets films were deposited by a solvothermal process. Then, the SnS_x nanosheets films were converted to BiS_x nanorod films through a hydrothermal route in the aqueous solution containing $BiCl_3$ and HCl. Finally, $BiVO_4$ porous NWs were obtained via drop casting a dimethyl sulfoxide solution containing $VO(acac)_2$ onto the BiS_x films, followed by annealing at 450 °C in air. The nanoparticles in the NWs were about 100–300 nm in size. Under optimized synthesis conditions, the $BiVO_4$ photoelectrode show a photocurrent density of 1.67 mA cm^{-2} at 1.83 V (vs. RHE) in a 0.5 mol L^{-1} Na_2SO_4 electrolyte solution.

4.4.2. Nanosheet-based arrays

As widely reported, the crystal plane structure of a semiconductor material can influence its photocatalytic and PEC activities. Therefore, increasing the exposed active facets of $BiVO_4$ by forming nanosheet structure is promising. For powdered $BiVO_4$, photocatalytic activity were significantly enhanced with large exposed (0 4 0) facets [371–373]. However, there are only a few reports on $BiVO_4$ photoelectrodes with exposed (0 4 0) facets because the adjacent (0 4 0) facets tend to grow together easily to form a compact structure. With the aid of a $TiCl_3$-structure directing agent (Ti-SDA) and a seed layer, Kim et al. [374] successfully deposited a (0 4 0)-crystal facet engineered $BiVO_4$ nanosheet array by a hydrothermal method. The $BiVO_4$ NSs that show a single-crystalline feature grew vertically/hydrothermally along the (1 2 1) direction, with a large exposure of (0 4 0) facet. It was demonstrated that increasing the concentration of Ti-SDA would increase the exposed lateral side of the nanosheets due to the affinity between SDA and the particular facet. As indicated, the (0 4 0) crystal facets could accumulate photogenerated charges and suppress charge recombination to boost charge separation and transport efficiency. As a result, in a PEC, the (0 4 0)-crystal facet engineered $BiVO_4$ nanosheet array exhibited a considerable performance enhancement, obtaining a photocurrent density of 0.94 mA cm^{-2} at 1.23 vs. RHE under AM 1.5 G illumination. Recently, Xia et al. [375] developed a chemical bath deposition (CBD) method to grow $BiVO_4$ nanosheet arrays by using NaCl as a coordinating agent. Though NS morphology could be observed, the NSs seemed to be stacked compactly with a small film thickness (about 200–300 nm). But the large exposed (0 4 0) facets still afford a higher PEC performance in a 0.1 mol L^{-1} KH_2PO_4 electrolyte, about 1.26 mA cm^{-2} at 1.23 V vs. RHE under AM 1.5 G illumination.

In order to further improve the PEC performance of $BiVO_4$ NS arrays, several new strategies have been developed. Wang et al. [376] have grown a $BiVO_4$ nanosheet array with (0 4 0) facets grown vertically on FTO glass by a seed-assisted hydrothermal method in a reaction solution containing $Bi(NO_3)_3{\cdot}5H_2O$, NH_4VO_3 and HNO_3. A simple electrochemical reduction treatment was conducted to create oxygen vacancies. Compared to pristine $BiVO_4$ nanosheet arrays, electrochemical reduction drastically improved the photocurrent density by 10-fold, reaching 2.5 mA cm^{-2} at 1.23 V vs. RHE under AM 1.5 G illumination. After loading CoBi cocatalyst, the photocurrent density was further promoted to 3.2 mA cm^{-2}, with an ABPE of 1.1%. For PEC photoelectrode, forming a suitable heterojunction is also a promising approach to enhance water splitting performance. With respect to $BiVO_4$, Ag_3PO_4 exhibits a good energy structure match for constructing heterojunction. Recently, the $BiVO_4/Ag_3PO_4$ heterojunction based on $BiVO_4$ nanosheet array was investigated by Gao et al. [377]. $BiVO_4$ NS array was also grown by the seed-assisted hydrothermal

method using the reaction solution containing $Bi(NO_3)_3{\cdot}5H_2O$, NH_4VO_3, NaOH and EDTA. Through photo-deposition and electrodeposition Ag_3PO_4 could be deposited on electron-dominant facets and hole-dominant crystal facets, respectively. Both heterojunctions enhanced PEC performance and the heterojunction on the hole-dominant facet exhibited more obvious enhancement, suggesting a higher charge separation efficiency for these facets.

4.4.3. $WO_3/BiVO_4$ nanoarrays

Though $BiVO_4$ is a very promising photoelectrode materials, their PEC performance is still not very high, which is mainly limited by poor charge separation. To enhance charge separation, an effective way is to construct heterojunction with another semiconductor who has suitable energy level. In the last decade, pairing $BiVO_4$ with WO_3 is proven to be a promising strategy to achieve higher charge separation and improve the overall PEC performance [378]. In 2009, Chatchai et al. [379] reported the first successful demonstration of $WO_3/BiVO_4$ heterojunction PEC photoelectrode. Since then many efforts on improving the efficiency of $WO_3/BiVO_4$ photoelectrodes have been reported. Among various morphologies of $WO_3/BiVO_4$ photoelectrodes, nanoarray photoelectrodes have attracted much attention.

Due to the higher electric conductivity, WO_3 NR/NW arrays have been widely used to support $BiVO_4$ to form heterojunction photoelectrodes. Commonly, WO_3 NR/NW arrays were firstly formed, followed by the deposition of $BiVO_4$ layers. For example, Su et al. [380] have spin coated a $BiVO_4$ layer on the WO_3 NR arrays that were pre-deposited on FTO glass by solvothermal method. Compared to planar $WO_3/BiVO_4$ heterojunction, $WO_3/BiVO_4$ NR photoelectrode exhibited an enhanced photocurrent density of 0.8 mA cm^{-2} at 1 V vs. Pt. Then, Pilli et al. [381] prepared the similar $WO_3/BiVO_4$ heterojunction photoelectrode using Co-Pi as catalyst. The presence of Co-Pi catalyst not only improved the photocurrent density due to the superior kinetics of oxygen evolution, but also shift the onset potential towards lower potential. In addition to solvothermal method, some other methods have been employed to grow WO_3 NR array $WO_3/BiVO_4$ photoelectrode. Rao et al. [204] has employed a flame vapor deposition method to grow WO_3 NR. Such WO_3 NR exhibited superior electrical conductivity, which afford a promising photocurrent density of 3.1 mA cm^{-2} at 1.23 V vs. RHE under standard testing conditions without using any water oxidation catalyst. Pihosh et al. [382] reported the growth of highly vertical WO_3 NR array capped with thin $BiVO_4$ layers by the combination of glancing angle deposition and normal physical sputtering techniques. With the modification of Co-Pi catalyst, the heterojunction photoelectrode show a stable photocurrent density of 3.2 mA cm^{-2} at 1.23 V vs. RHE in 0.5 mol L^{-1} Na_2SO_4 electrolyte under standard testing conditions. Soon afterwards, instead of capping the WO_3 NR arrays with $BiVO_4$ by sputtering, Pihosh et al. [383] have grown a thin $BiVO_4$ layer (thickness: 25 nm) on WO_3 NR arrays to form core-shell structure. The optimized $WO_3/BiVO_4$/CoPi photoelectrode exhibited a record photocurrent density of 6.72 mA cm^{-2} at 1.23 V vs. RHE under standard testing conditions with an IPCE value of about 90% at 510 nm.

In addition to NR arrays, other WO_3 nanoarrays have also been employed to prepare $WO_3/BiVO_4$ photoelectrode. Shi et al. [384] have grown WO_3 helical nanoarrays for the $WO_3/BiVO_4$ photoelectrodes. The WO_3 helical nanoarrays were synthesized on the FTO glass by an oblique angle deposition method, while Mo-doped $BiVO_4$ was deposited on the WO_3 helical nanoarrays by drop casting. Such heterojunction photoelectrode exhibited obvious advantages, including single-like crystallinity for efficient charge transportat, higher light-scattering capability for enhanced light absorption, and large active area for improved charge separation. The optimized $WO_3/BiVO_4$ helical nanoarrays produced a maximum photocurrent density of 5.35 mA cm^{-2} at 1.23 V vs. RHE, respectively. Zeng et al. [385] prepared a WO_3 NS array for $WO_3/BiVO_4$ photoelectrodes by a chemical bath deposition method. The deposition solution contained mainly H_2WO_4, $(NH_4)_2C_2O_4$, HCl (37%) and H_2O_2. Mo:$BiVO_4$ was deposited via a spin-coating process. The WO_3/Mo:$BiVO_4$ photoelectrode exhibited a high photocurrent density of 3.78 mA cm^{-2} at 1.23 V vs. RHE under standard testing conditions, which was further boosted to 5.38 mA cm^{-2} after modification with Co-Pi catalyst.

4.4.4. Other nanoarrays

The high-surface-area, nanoporous $BiVO_4$ electrodes are intended to improve its poor electron-hole separation yield, thus leading to an enhanced STH conversion efficiency. Recently, we have sequentially deposited nanoporous Mo-doped $BiVO_4$ (Mo:$BiVO_4$) and OER catalyst (Fe(Ni)OOH) on a 3D nanocone structure to obtain a novel nanocone/Mo:$BiVO_4$/Fe(Ni)OOH photoanode. The Mo:$BiVO_4$ layer with a larger effective thickness maintains highly efficient charge separation and high light absorption capability, which can be further enhanced by multiple light scattering in the nanocone structure, while the Fe(Ni)OOH catalysts play an important role in the rapid increase in photocurrent at relatively low potential. As a result, the nanocone/Mo:$BiVO_4$/Fe(Ni)OOH photoanode exhibits a high photocurrent of (5.82 ± 0.36) mA cm^{-2} at 1.23 V vs. RHE (Fig. 11) [200].

4.5. Fe_2O_3 photoanodes

α-Fe_2O_3 with a band gap of 2.1 eV has attracted broad interest as a water splitting photoelectrode material because of its low-cost, earth-abundance and high theoretical STH of 14%–17%, corresponding to a photocurrent density of 11–14 mA cm^{-2} under one-sun illumination [386]. However, its disadvantages are also obvious, such as a relatively low absorption coefficient, poor majority carrier conductivity and short diffusion length (L_D = 2–4 nm) of minority carriers, meaning that enhancing light absorption by increasing film thickness would result in serious charge recombination losses [387]. As such, nanostructure design strategy is important to increase light absorption without increasing hole transfer distances and electron transport pathway lengths.

4.5.1. Nanorod arrays

Using NR or NW array structures is an obvious solution to the problems of majority carrier transport and short diffusion length of minority carriers in hematite films. Single-crystal NRs/NWs with small diameter would not only eliminate grain boundaries to provide a direct transport path for electrons, but also allow holes to efficiently the reach reaction sites at surface. Takagi et al. [53] for the first time grew α-Fe_2O_3 NR arrays in an aqueous solution containing ($FeCl_3{\cdot}6H_2O$) and $NaNO_3$ for PEC applications. Through the controlled precipitation of Fe^{3+}, different morphology and sizes of α-Fe_2O_3 NRs could be obtained. However, even though KI has been used as hole scavenger, the PEC performance was very low (IPCE ≈ 5% at 360 nm), which was attributed to the presence of a large amount of that bulk or surface defects.

Although the original α-Fe_2O_3 NR arrays show low PEC performance, the promising structure consideration and its successful growth and application in PEC still draw much attention. As a result, many new methods have been developed to grow α-Fe_2O_3 NR arrays. For examples, many groups have adopted thermal oxidation to grow α-Fe_2O_3 NR arrays on iron foils. Though these NR arrays exhibited attractive morphology with diameters of 20–40 nm and lengths of up to 5 mm, no decent PEC activity towards water oxidation has been reported, which might result from the presence of high defect density or impurity of suboxides.

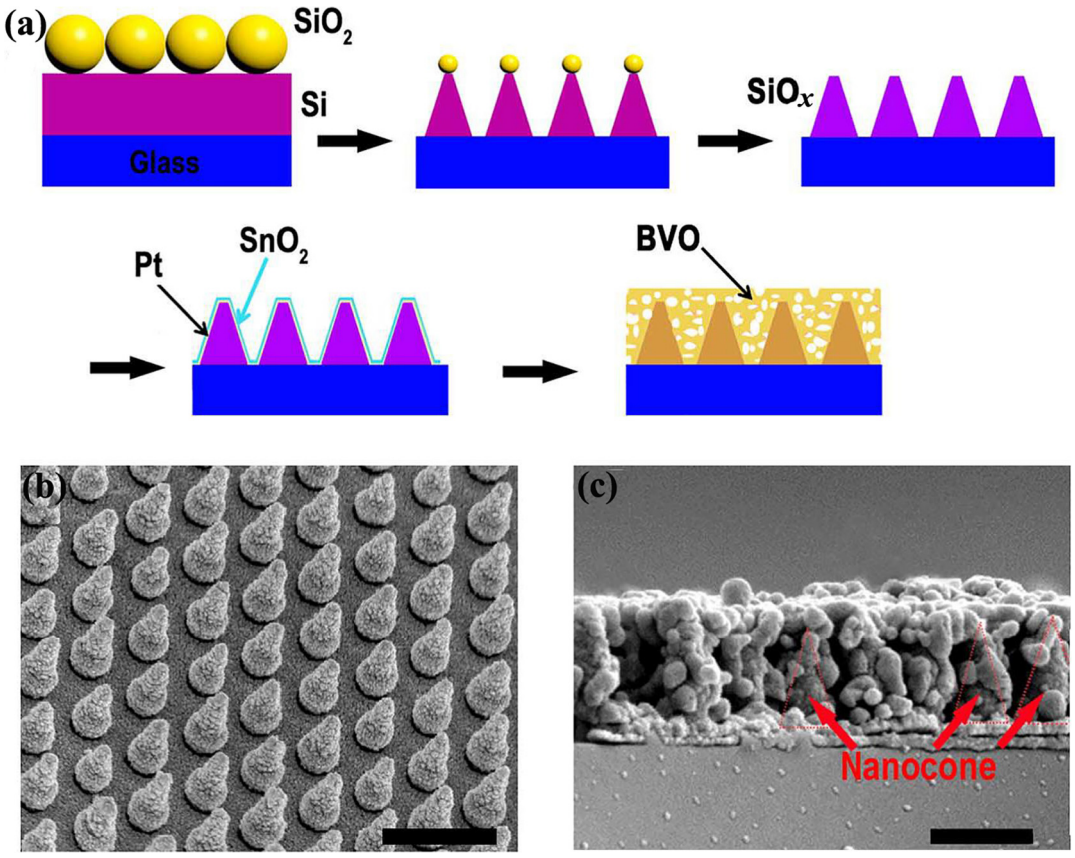

Fig. 11. (Color online) (a) Schematic illustration of the fabrication process of the conductive nanocone substrate and electron microscope images of Mo:$BiVO_4$. (b) Scanning electron microscope (SEM) images (60° tilting) of the final SiO_x/Pt/SnO_2 nanocone arrays. (c) Cross-sectional SEM images of Mo:$BiVO_4$ on the SiO_x/Pt/SnO_2 nanocone substrate. Reprinted with permission from Ref. [200].

Hydrothermal method has been widely used to deposit Fe_2O_3 NR arrays on FTO substrate. Generally, the hydrothermal conditions at low temperature would result in FeOOH, the hydrated phase of iron oxide (akaganeite and/or goethite), and an additional treatment at elevated temperature is necessary to obtain pure and active hematite photoelectrodes. A typical hydrothermal process reported by Vayssieres et al. [388] using an aqueous deposition solution containing $FeCl_3{\cdot}6H_2O$ and $NaNO_3$ set at pH 1.5 (set by HCl). The NR arrays with single-crystalline structure were perpendicularly grown onto the substrate. The diameter of the NRs was typically 5 nm which self-assembled as a bundle of about 50 nm in diameter. Using such vertical NR arrays significantly improved the PEC performance compared with other hematite film morphologies [389–393], which was due to the small NR diameter for efficient hole transfer and rapid electron transport in the well aligned NR arrays. However, the PEC performance of the earliest reported NR arrays was still very low. Until 2011, the PEC performance was significantly improved by activating hematite surfaces using an appropriate annealing treatment [155], and a photocurrent density of around 0.52 mA cm^{-2} at 1.23 vs. RHE was obtained under standard illumination. Then, Ling et al. [394] reported an alternative method for the preparation of highly conductive and photoactive hematite arrays through thermal decomposition of β-FeOOH in an oxygen-deficient atmosphere (N_2^+ air). The photocurrent density was largely improved up to 1.82 mA cm^{-2} at 1.23 vs. RHE under the standard testing conditions. Such promising PEC performance has aroused great interest and as a result, more and more Fe_2O_3 NR arrays have been grown by hydrothermal method for PEC application [151,395,396].

Electrodeposition has also been used to prepare hematite nanorod arrays. Mao et al. [397] have reported the growth of Fe_2O_3 NR arrays by using anodic aluminum oxide (AAO) as a template. A gold layer was sputtered onto one side of the AAO membrane as the growth substrate. The electrodeposition process was conducted in an aqueous solution containing ferrous sulfate, ascorbic acid amidosulfonic acid and boric acid. Following post annealing, the AAO was removed by dissolution in an aqueous NaOH solution. The diameter and the length of the rods were determined by the template diameter and deposition duration, respectively. In PEC, a 10 mm thick NR array showed a water oxidation photocurrent density of about 1 mA cm^{-2} at a potential of 1.5 V vs. RHE under AM 1.5 G illumination. As no defined photocurrent plateau was observed, it was proposed that there was a majority carrier transport limitation in this nanostructure. Spray et al. [398] applied an anodic electrodeposition to grow α-Fe_2O_3 nanostructure in an aqueous solution containing $FeCl_2{\cdot}5H_2O$ and NH_4Cl. The pH values have a great influence on the α-Fe_2O_3 morphology and NR arrays with a diameter of tens of nanometers and a length of 1 μm were obtained. Though such NR arrays were photoactive in an iodide-contained electrolyte, no water oxidation photocurrent was observed, suggesting low material quality.

Similarly, doping is also an effective way to enhance the PEC performance of α-Fe_2O_3 nanorod arrays. However, α-Fe_2O_3 has a more suitable E_g, which exhibits a wide light absorption range for PEC. Therefore, the aim of doping in α-Fe_2O_3 nanorod arrays is not to enhance light absorption but to increase its intrinsically limited conductivity. This could be easily achieved by substitutional doping using the elements in +4 to +6 state, including Ti

[262,399–401], Sn [402–407], Si [408], Zr [404], Ge [409], Se [410], Ta [411,412], W [413], and Nd [412]. Sn-doping could be achieved by simply annealing α-Fe_2O_3 nanorod arrays at a higher temperature (e.g., 800 °C), during which Sn element could diffuse from FTO substrate to the hematite NRs [402,407]. Other doping strategies including the addition of the doping element during the synthesis process (such as in the solution of hydrothermal method) or coating the pre-deposited α-Fe_2O_3 nanorod arrays followed by post annealing for element diffusion. For example, Fu et al. [401] prepared the Ti-doped α-Fe_2O_3 nanorod arrays by hydrothermal method with the addition of $TiCl_4$ in the growth solution of α-Fe_2O_3 NR arrays. Shen et al. [414] grow Zr-doped a-Fe_2O_3 NR arrays by hydrothermal method through adding the Zr doping source ($ZrO(NO_3)_2{\cdot}xH_2O$) into the growth solution ($FeCl_3{\cdot}6H_2O$ and $NaNO_3$). Xi et al. [393] reported the preparation of Sn-doped α-Fe_2O_3 nanorod arrays by dropping $SnCl_4{\cdot}5H_2O$ aqueous solution on hydrothermally grown FeOOH nanorod arrays, followed by annealing in air at 750 °C for 30 min. Wang et al. [399] applied an atomic layer deposition process to deposit a Ti_xO_y coating on a pre-deposited hematite nanorod array, which was converted to Ti-doped α-Fe_2O_3 NR arrays through post annealing at 700 °C.

In order to accelerate the OER kinetics, modifying the α-Fe_2O_3 nanorod arrays with an oxygen evolution catalyst to increasing hole transfer rate to electrolyte is the most effective strategy. The most important result for the modification of catalysts is to negatively shift the onset potential of photocurrent density. The catalysts were usually deposited on the pre-deposited α-Fe_2O_3 nanorod arrays. IrO_x is the most efficient catalyst in terms of OER activity [415,416]. However, due to the high cost of Ir, only a few reports deal with IrO_x-decorated hematite for PEC applications. As a result, many other catalysts for α-Fe_2O_3 photoelectrode include Co-Pi [263,417,418], Ni-Fe- and Zn-Co-based LDH, FeOOH, NiOOH [404], CoOOH [262], $Ni(OH)_2$ [399], and $Ni(OH)_2/IrO_2$ [419]. Among these new catalysts, Co-Pi on α-Fe_2O_3 nanorod arrays not only improved the overall photocurrent density but also significantly shifted the photocurrent onset potential to more negative values [263,417,418]. This mainly benefited from the bridging effect of phosphate ions that would facilitate hole injection from α-Fe_2O_3 to Co ions.

To further enhance light utilization of α-Fe_2O_3 NR arrays, the incorporation of a plasmonic metal nanostructure (e.g., nanoparticles, nanorods, nanopillars) on the photoelectrode surface is desirable. However, Thimsen et al. [396] reported a negative water photooxidation result for the modification of Fe_2O_3 thin film or nanoplatelet photoelectrodes with Au nanoparticles. This was attributed to the presence of surface states at Au–Fe_2O_3 interface, which significantly increased recombination. To overcome this problem, Xu et al. [420] passivated the surface states of Fe_2O_3 NRs with an Al_2O_3 layer to form an effective resonant energy-transfer interface between Ti-doped Fe_2O_3 and Au NPs. The Ti-Fe_2O_3/Al_2O_3/Au photoelectrode well enhanced PEC performance, which was attributed to the passivation of the surface states of Ti-Fe_2O_3, for relaxing Fermi-level pinning and forming an effective SPR energy-transfer interface.

4.5.2. Nanotube arrays

Compared with NR structure, NT structure seems to be more suitable for α-Fe_2O_3 PEC because the thin walls could afford larger active area and shorten the distance for hole to reach the solid/-electrolyte interface. Though hydrothermal methods have been well developed to synthesize randomly oriented α-Fe_2O_3 NTs [421–423], it was still difficult to grow NT array on substrates. In order to grow α-Fe_2O_3 NT arrays, Shen et al. [424] have applied Fe_2O_3 NT arrays by pyrolyzing $Fe(acac)_3$ (Hacac = 2,4-pentanedione) at 300 °C in anodic alumina membranes. The NT arrays have an outer diameter of about 100–300 nm and a length of tens of microns.

So far, electrochemical method has been the most effective technique to grow α-Fe_2O_3 NT arrays. Rangaraju et al. [425] grow a self-ordered and vertically oriented array of iron oxide nanotubes by anodizing a pure iron substrate in an ethylene glycol-based electrolyte containing NH_4F and water. The NTs have the walls of less than 50 nm thick and the lengths of about 1.5 μm. At an optimized annealing treatment, the obtained sample was a mixed phases of hematite and maghemite. However, such photoelectrode had only a small PEC performance (160 μA cm^{-2}, 1.23 V vs. RHE under AM1.5 illumination). By applying a double step anodization procedure with the addition of sodium tripolyphosphate in the electrolyte, a dendrite-like morphology situated over the tube array was created. Such photoelectrode significantly promoted the photocurrent density to about 1 mA cm^{-2} at 1.23 vs. RHE under the same testing conditions, which was owed to the enlarged surface area for water oxidation and the electron transport highway of the vertically orientated NT arrays. Then, the work reported by the same group employed a sono-electrochemical anodization method to grow the NT arrays with 5–7 nm in thick and 3–4 μm in length [426]. Annealing the as-deposted NT arrays led to pure hematite that gave a photocurrent density of about 1 mA cm^{-2} at 1.23 V vs. RHE under the standard testing conditions. As the α-Fe_2O_3 NT arrays grown by electrochemical anodization have a promising structure and have obtained decent PEC performance, more and more works on the growth of the α-Fe_2O_3 NT arrays were reported [427–429].

4.5.3. Nanotree arrays

Nanotree arrays have been found to be the most efficient nanostructure for α-Fe_2O_3 photoelectrodes in PEC. Cesar et al. [430] have grown the promising α-Fe_2O_3 nanotree arrays by chemical vapor deposition at atmospheric pressure. The formation of the treelike structure was realized by the thermal decomposition iron pentacarbonyl, which was highly porous with a minimum feature size of 5–10 nm. It was found that silicon doping strongly influenced the morphology and grain size, and the silicon-doped sample show a preferred orientation with the (0 0 1) basal plane normal to the substrate. When used in PEC, the Si-doped α-Fe_2O_3 nanotree arrays achieved a photocurrent density of 1.45 mA cm^{-2} at 1.23 V vs. RHE under one-sun illumination in 1 mol L^{-1} NaOH. Soon after, Kay et al. [431] made a further optimization, at the substrate temperature of 420 °C and carrier gas flow rate of 2 L min^{-1}, the treelike nanoarrays grew on FTO substrate at a rate of about 100 nm min^{-1} and the pure hematite show a strong preferential orientation with the (1 1 0) axis vertical to the substrate. As a photoelectrode in PEC, the Fe_2O_3 nanotree arrays show promisingly high efficiency (IPCE = 42% at 370 nm and 1.8 mA cm^{-2} at 1.23 vs. RHE under the light illumination of AM 1.5 G 100 mW cm^{-2}). By coating a catalytic cobalt monolayer on the Fe_2O_3 surface, the photocurrent density at 1.23 vs. RHE was further increased to 2.2 mA cm^{-2}.

As reported previously, VPD parameters greatly influenced the oriented attachment of α-Fe_2O_3 nanoparticles. Further optimization indicated that by increasing the air flow rate from the previous 2 L min^{-1} (2L photoelectrode) to 6 L min^{-1} (6L photoelectrode), the gas residence time was shortened and the particle/precursor ratio was reduced, resulting in a better adhesion between the particles while attached to the growing film [416]. Besides, high air flow rate further enhanced the preferential orientation of the basal planes normal to the substrate, which would improve majority carrier transport. At the optimized thickness of 800 nm, the 6 L photoelectrode obtained an obviously enhanced photocurrent density of above 3 mA cm^{-2}. After modification with IrO_2 catalyst, the electrode produced a 200 mV shift in the photocurrent onset potential and the photocurrent density of 3.3 mA cm^{-2} at 1.23 VRHE was

obtained under the light illumination of AM 1.5 G 100 mW cm^{-2}. To further get an insight into structure difference between the 2 L and 6 L photoelectrodes, Warren et al. [432] have studied the spatial distribution of crystalline and current-carrying domains by employing a dark-field TEM (DF-TEM) in combination with conducting atomic force microscopy (C-AFM). It is found that the nanocrystal aggregates in the 2 L photoelectrode had about 75% high-angle grain boundaries, significantly higher than that in 6L photoelectrode (18%). C-AFM measurement demonstrated that the high-angle grain boundaries decreased the photocurrent density by generating a potential barrier for blocking the transport of majority carrier between adjacent crystals. Therefore, reducing the high-angle grain boundaries in nanotree arrays is important to obtain high photocurrent density and hence high PEC performance.

4.5.4. Other nanoarrays

Besides the above widely studied nanoarrays, some other α-Fe_2O_3 nanoarrays have been synthesized for water oxidation application, such as nanosheet arrays, nanospike arrays. Duret et al. [433] for the first time made an attempt to synthesize an ultrathin hematite nanostructure by the ultrasonic spray pyrolysis technique. The obtained Fe_2O_3 layers were mesoscopic consisting mainly of 100 nm-sized platelets with a thickness of 5–10 nm, which are oriented perpendicularly to the FTO substrate with exposing the (0 0 1) facets. Such structure not only allowed for efficient light harvesting, but also reduced hole transport distance before reaching the electrolyte interface. Liu et al. [409] have developed a hydrothermal method to grow highly oriented Ge-doped Fe_2O_3 nanosheet arrays by using β-FeOOH nanorod arrays as sacrificial templates. The nanosheets grow in the (0 0 1) basal plane and aligned vertically on the FTO substrate. These nanosheets were ultrathin with the thicknesses of <10 nm and the highly dense film has an overall thickness of about 430 nm. As a photoelectrode in PEC, the Ge-doped α-Fe_2O_3 nanosheet arrays obtained a photocurrent density of 1.4 mA cm^{-2} at 1.23 V vs. RHE, about 50 times higher than that of the undoped α-Fe_2O_3 nanorod arrays.

Thin hematite layer is beneficial to charge collection. However, the light utilization capacity of the photoelectrode would be sacrificed. To avoid such problem, Qiu et al. [196] fabricated an ultrathin hematite layer on the pre-synthesized regular arrays of 3D conductive nanospikes (Fig. 12). The nanophotonic structures could significantly improve light absorption in the ultrathin hematite active material, where the large surface area accommodates the slow surface water oxidation process and act as an efficient carrier collection path. As a result, a high current density of 3.05 mA cm^{-2} at 1.23 V vs. RHE has been achieved on such

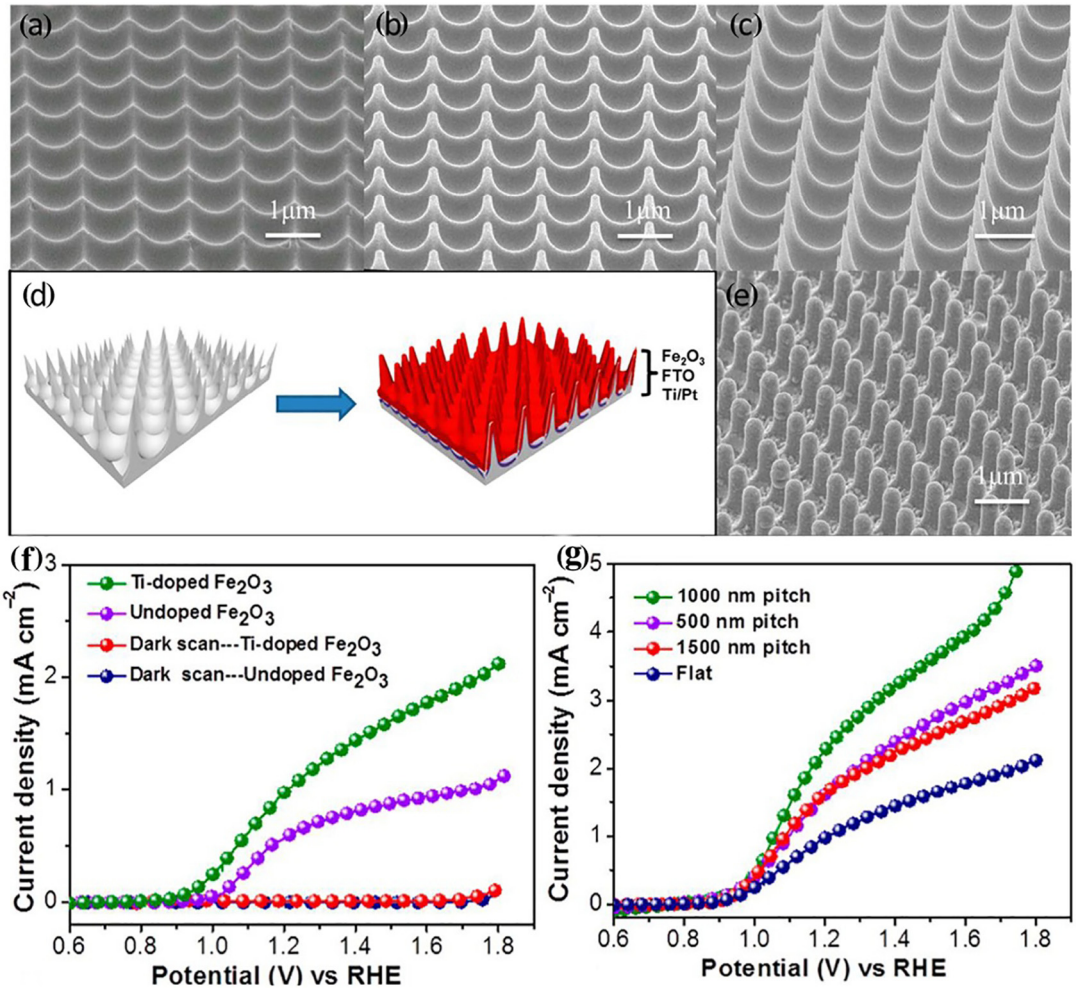

Fig. 12. (Color online) Sixty degree tilted SEM images of 1,000 nm pitch nanospikes with nanospikes height of about (a) 350, (b) 750, and (c) 1,100 nm. (d) Schematic diagram of multiple layers thin film deposition including, Ti/Pt of 100 nm, FTO of 200 nm and α-Fe_2O_3 of 85 nm for water splitting device fabrication. (e) Sixty degree tilted SEM view of α-Fe_2O_3 decorated nanospikes. (f) *J-V* curves of the undoped α-Fe_2O_3 photoelectrode and the Ti-doped α-Fe_2O_3 photoelectrode. (g) *J-V* curves of the Ti-doped α-Fe_2O_3 photoelectrodes based on the three different nanospikes arrays. Reprinted with permission from Ref. [196]. Copyright (2014) American Chemical Society.

nanophotonic structures, which is about three times higher than that of the planar photoelectrode. Then, Li et al. [119] fabricated a 3D hexagonal FTO nanocone array to support the thin Ti-doped hematite with a film thickness of 90–100 nm. The nanocone arrays showed an 86% increment in photocurrent density at 1.23 V vs. RHE compared to the planar counterpart.

4.6. Other metal oxide photoelectrodes

Besides TiO_2, ZnO, WO_3, $BiVO_4$ and α-Fe_2O_3, some other oxide semiconductor photoelectrodes including SnO_2 and Nb_2O_5 have also been explored intensively [149,434,435]. For example, a facile approach for the fabrication of monolayer SnO_2 inversed opals is presented by Chen et al. [434] using polymer colloid monolayer nanofilms from oil-water interface self-assembly as sacrificial templates. Monolayer SnO_2 inversed opals based photoanode presented a high photocurrent 2.1 mA cm^{-2} at 1.23 V vs. RHE and excellent stability. Similar to TiO_2, Nb_2O_5, $SrTiO_3$, $KTaO_3$ and $BaTiO_3$ suffer from low solar conversion performances due to their large band gaps.

5. Conclusion and outlook

In conclusion, we have systematically reviewed the recent progresses on various metal oxide-based nanoarray photoanodes for PEC applications. The structure, work principle and their relevant efficiency calculations of a PEC cell have been firstly and briefly introduced. So far, a lot of methodologies and strategies have been adopted to prepare metal oxide-based nanoarrays for PEC applications, including VLS and VS, SLS, HT/ST, CBD, TB, EC and precursor arrays-based methods. By combining some of these methods, the nanoarray photoelectrodes with various structures could be designed and prepared, such as homo/heterogeneous branching structures, type-II junction, p-n junction, Z-scheme system and hot-electron injection electrode. For different metal oxide (TiO_2, ZnO, WO_3, $BiVO_4$ and Fe_2O_3), NW, NR, NT and nano-branched arrays have been the most commonly developed photoelectrode structures. In addition, nanotree array has been the most effective structure for Fe_2O_3 photoelectrode, while nanosheet arrays have been widely employed for WO_3 photoelectrodes. WO_3/$BiVO_4$ heterojunction nanoarrays have shown much promise to achieve the highest PEC performance. In order to enhance light utilization, doping and sensitization strategies have been widely employed for different photoelectrode, while catalysts have been applied to improve charge transfer at the photoelectrode/electrolyte interface.

For future direction, different photoelectrodes should have relevant strategies for improving their PEC performances. The stable and large photocurrents of the photoanodes are urgent needs for the future. For TiO_2 and ZnO photoelectrodes, the narrow light absorption range due to their large E_g is the main problems. Therefore, element doping and/or surface sensitization should be developed to increase light absorption. Besides, using nanostructures promoting enhanced light scattering is yet another possible way to enhance the conversion efficiency. For WO_3, E_g is slightly smaller than those of TiO_2 and ZnO, but its CB is more positive than the H^+/H_2 redox potential. Therefore, energy level engineering is important to elevate the CB position and element doping should be an effective way, which may further reduce the E_g for enhancing light absorption. The monoclinic $BiVO_4$ material has a narrower E_g of 2.2 eV and hence a high theoretical PEC efficiency. However, low charge transport rate considerably suppresses its PEC performance. To address this issue, designing nanoarray photoelectrode with a more straight transport way will still be urgent. Besides, heterojunction design, just like WO_3/$BiVO_4$, needs much more attention, which has achieved the highest PEC performance so far. α-Fe_2O_3 could absorb a wide light range due to its smaller E_g of 2.1 eV. However, low absorption coefficient, poor majority carrier conductivity and short diffusion length of minority carriers significantly limited its PEC performance. The future research should focus on designing and preparing the high-quality nanoarray photoelectrode with thin nano units, which may accelerate charge transport and enhance charge transfer at the interface with electrolyte. In addition, exploiting more efficient co-catalysts is an another effective way to enhance hole transfer at the interface and hence reduce charge recombination loss. Furthermore, the co-catalysts also help the photoanodes maintain stability under reaction conditions. Therefore, searching co-catalysts with low overpotential and high photocorrosion resistance will be a future research direction for developing high-performance and stable photoanodes. The current STH efficiency for PEC devices is low, the future research should focus on unbiased water splitting systems such as PEC/PV and PEC/PEC system.

Conflict of interest

The authors declare that they have no conflict of interest.

Acknowledgments

This work was supported by the National Key Research and Development Program of China (2018YFA0209600), Shenzhen Peacock Plan (KQTD2016053015544057) and Nanshan Pilot Plan (LHTD20170001).

Author contributions

All the authors discussed the results and commented on the manuscript.

References

[1] Jiang CR, Moniz SJA, Wang AQ, et al. Photoelectrochemical devices for solar water splitting – materials and challenges. Chem Soc Rev 2017;46:4645–60.
[2] Walter MG, Warren EL, McKone JR, et al. Solar water splitting cells. Chem Rev 2010;110:6446–73.
[3] Kang D, Kim TW, Kubota SR, et al. Electrochemical synthesis of photoelectrodes and catalysts for use in solar water splitting. Chem Rev 2015;115:12839–87.
[4] Osterloh FE. Inorganic nanostructures for photoelectrochemical and photocatalytic water splitting. Chem Soc Rev 2013;42:2294–320.
[5] Lin LL, Zhou W, Gao R, et al. Low-temperature hydrogen production from water and methanol using Pt/alpha-MoC catalysts. Nature 2017;544:80–3.
[6] Maeda K, Teramura K, Lu DL, et al. Photocatalyst releasing hydrogen from water – enhancing catalytic performance holds promise for hydrogen production by water splitting in sunlight. Nature 2006;440:295.
[7] Zhu LY, Lu YJ, Shen SH. Solar fuel production at high temperatures using ceria as a dense membrane. Energy 2016;104:53–63.
[8] Han YH, Zhang L, Wang YF, et al. Photoelectrocatalytic activity of an ordered and vertically aligned TiO_2 nanorod array/BDD heterojunction electrode. Sci Bull 2017;62:619–25.
[9] Wang M, Wang M, Fu YM, et al. Cobalt oxide and carbon modified hematite nanorod arrays for improved photoelectrochemical water splitting. Chin Chem Lett 2017;28:2207–11.
[10] Chen XY, Li YR, Shen SH. Surface- and interface-engineered heterostructures for solar hydrogen generation. J Phys D Appl Phys 2018;51:163002.
[11] Fu YM, Cao FR, Wu FL, et al. Phase-modulated band alignment in CdS nanorod/SnS_x nanosheet hierarchical heterojunctions toward efficient water splitting. Adv Funct Mater 2018;28:1706785.
[12] Liu D, Liu B. Novel design of photoelectrochemical device by dual $BiVO_4$ photoelectrode with abundant oxygen vacancy. Sci Bull 2018;63:1027–8.
[13] Liu JQ, Dai MJ, Wu J, et al. Electrochemical hydrogenation of mixed-phase TiO_2 nanotube arrays enables remarkably enhanced photoelectrochemical water splitting performance. Sci Bull 2018;63:194–202.
[14] Lou XW. Double-layered heterojunction nanotubes with spatially separated redox centers for photocatalytic hydrogen generation. Sci Bull 2018;63:599–600.
[15] Shen SH, Chen J, Wang M, et al. Titanium dioxide nanostructures for photoelectrochemical applications. Prog Mater Sci 2018;98:299–385.

[16] Wan XK, Wang L, Dong CL, et al. Activating klaui-type organometallic precursors at metal oxide surfaces for enhanced solar water oxidation. ACS Energy Lett 2018;3:1613–9.
[17] Zhou ZH, Peng P, Xiang ZH. N-rich covalent organic polymer in situ modified TiO_2 for highly efficient photocatalytic hydrogen evolution. Sci Bull 2018;63:369–75.
[18] Fujishima A, Honda K. Electrochemical photolysis of water at a semiconductor electrode. Nature 1972;238:37–8.
[19] Tamirat AG, Rick J, Dubale AA, et al. Using hematite for photoelectrochemical water splitting: a review of current progress and challenges. Nanoscale Horiz 2016;1:243–67.
[20] Scanlon DO, Dunnill CW, Buckeridge J, et al. Band alignment of rutile and anatase TiO_2. Nat Mater 2013;12:798–801.
[21] Chen HN, Yang SH. Hierarchical nanostructures of metal oxides for enhancing charge separation and transport in photoelectrochemical solar energy conversion systems. Nanoscale Horiz 2016;1:96–108.
[22] Yang Y, Niu SW, Han DD, et al. Progress in developing metal oxide nanomaterials for photoelectrochemical water splitting. Adv Energy Mater 2017;7:1700555.
[23] Wang GM, Ling YC, Li Y. Oxygen-deficient metal oxide nanostructures for photoelectrochemical water oxidation and other applications. Nanoscale 2012;4:6682–91.
[24] Kment S, Riboni F, Pausova S, et al. Photoanodes based on TiO_2 and alpha-Fe_2O_3 for solar water splitting – superior role of 1D nanoarchitectures and of combined heterostructures. Chem Soc Rev 2017;46:3716–69.
[25] Wang GM, Ling YC, Wang HY, et al. Chemically modified nanostructures for photoelectrochemical water splitting. J Photochem Photobiol C 2014;19:35–51.
[26] Cheng CW, Fan HJ. Branched nanowires: synthesis and energy applications. Nano Today 2012;7:327–43.
[27] Bae D, Seger B, Vesborg PCK, et al. Strategies for stable water splitting via protected photoelectrodes. Chem Soc Rev 2017;46:1933–54.
[28] Chun JY, Lee JW. Various synthetic methods for one-dimensional semiconductor nanowires/nanorods and their applications in photovoltaic devices. Eur J Inorg Chem 2010:4251–63.
[29] Mi Y, Wen LY, Xu R, et al. Constructing a AZO/TiO_2 core/shell nanocone array with uniformly dispersed Au NPs for enhancing photoelectrochemical water splitting. Adv Energy Mater 2016;6:1501496.
[30] Ai GJ, Mo R, Xu H, et al. Vertically aligned TiO_2/(CdS, CdTe, CdSTe) core/shell nanowire array for photoelectrochemical hydrogen generation. J Power Sources 2015;280:5–11.
[31] Guha P, Chakrabarti S, Chaudhuri S. Synthesis of beta-Ga_2O_3 nanowire from elemental Ga metal and its photoluminescence study. Physica E 2004;23:81–5.
[32] Lu JG, Chang PC, Fan ZY. Quasi-one-dimensional metal oxide materials – synthesis, properties and applications. Mater Sci Eng R 2006;52:49–91.
[33] Devan RS, Patil RA, Lin JH, et al. One-dimensional metal-oxide nanostructures: recent developments in synthesis, characterization, and applications. Adv Funct Mater 2012;22:3326–70.
[34] Barth S, Hernandez-Ramirez F, Holmes JD, et al. Synthesis and applications of one-dimensional semiconductors. Prog Mater Sci 2010;55:563–627.
[35] Park S, Kim S, Kim HJ, et al. Hierarchical assembly of TiO_2-$SrTiO_3$ heterostructures on conductive SnO_2 backbone nanobelts for enhanced photoelectrochemical and photocatalytic performance. J Hazard Mater 2014;275:10–8.
[36] Wagner RS, Ellis W. Vapor-liquid-solid mechanism of single crystal growth. Appl Phys Lett 1964;4:89.
[37] Rao CNR, Deepak FL, Gundiah G, et al. Inorganic nanowires. Prog Solid State Chem 2003;31:5–147.
[38] Zhong M, Sato Y, Kurniawan M, et al. ZnO dense nanowire array on a film structure in a single crystal domain texture for optical and photoelectrochemical applications. Nanotechnology 2012;23:495602.
[39] Zhong M, Li YB, Yamada I, et al. ZnO-$ZnGa_2O_4$ core-shell nanowire array for stable photoelectrochemical water splitting. Nanoscale 2012;4:1509–14.
[40] Chakrapani V, Thangala J, Sunkara MK. WO_3 and W_2N nanowire arrays for photoelectrochemical hydrogen production. Int J Hydrog Energy 2009;34:9050–9.
[41] Rao PM, Cho IS, Zheng XL. Flame synthesis of WO_3 nanotubes and nanowires for efficient photoelectrochemical water-splitting. Proc Combust Inst 2013;34:2187–95.
[42] Park S, Lee CW, Cho IS, et al. Growth of anatase and rutile TiO_2@Sb:SnO_2 heterostructures and their application in photoelectrochemical water splitting. Int J Hydrog Energy 2014;39:17508–16.
[43] Yang J, Bao CX, Yu T, et al. Enhanced performance of photoelectrochemical water splitting with ITO@alpha-Fe_2O_3 core-shell nanowire array as photoanode. ACS Appl Mater Interfaces 2015;7:26482–90.
[44] Han HS, Han GS, Kim JS, et al. Indium-tin-oxide nanowire array based CdSe/CdS/TiO_2 one-dimensional heterojunction photoelectrode for enhanced solar hydrogen production. ACS Sustain Chem Eng 2016;4:1161–8.
[45] Lee S, Park S, Han GS, et al. Transparent-conducting-oxide nanowire arrays for efficient photoelectrochemical energy conversion. Nanoscale 2014;6:8649–55.
[46] Rao PM, Zheng XL. Rapid catalyst-free flame synthesis of dense, aligned alpha-Fe_2O_3 nanoflake and CuO nanoneedle arrays. Nano Lett 2009;9:3001–6.
[47] Rao P, Cho IS, Zheng XL. Flame synthesized metal oxide nanowires as effective photoanodes for photoelectrochemical water-splitting. Proc Combust Inst 2013;34:2187–95.
[48] Cai LL, Rao PM, Feng YZ, et al. Flame synthesis of 1-D complex metal oxide nanomaterials. Proc Combust Inst 2013;34:2229–36.
[49] Cai LL, Rao PM, Zheng XL. Morphology-controlled flame synthesis of single, branched, and flower-like alpha-MoO_3 nanobelt arrays. Nano Lett 2011;11:872–7.
[50] Rao PM, Zheng XL. Flame synthesis of tungsten oxide nanostructures on diverse substrates. Proc Combust Inst 2011;33:1891–8.
[51] Yuan L, Zhou G. The growth of one-dimensional oxide nanostructures by thermal oxidation of metals. Int J Nano Sci Nano Eng Nanotechnol 2012;4:1–23.
[52] Zhang WX, Yang SH. In situ fabrication of inorganic nanowire arrays grown from and aligned on metal substrates. Acc Chem Res 2009;42:1617–27.
[53] Takagi R. Growth of oxide whiskers on metals at high temperature. J Phys Soc Jpn 1957;12:1212–8.
[54] Kargar A, Jing Y, Kim SJ, et al. ZnO/CuO heterojunction branched nanowires for photoelectrochemical hydrogen generation. ACS Nano 2013;7:11112–20.
[55] Sunkara S, Vendra VK, Kim JH, et al. Scalable synthesis and photoelectrochemical properties of copper oxide nanowire arrays and films. Catal Today 2013;199:27–35.
[56] Chernomordik BD, Russell HB, Cvelbar U, et al. Photoelectrochemical activity of as-grown, alpha-Fe_2O_3 nanowire array electrodes for water splitting. Nanotechnology 2012;23:194009.
[57] Li S, Cai JJ, Mei YD, et al. Thermal oxidation preparation of doped hematite thin films for photoelectrochemical water splitting. Int J Photoenergy 2014;8:1–6.
[58] Grigorescu S, Lee CY, Lee K, et al. Thermal air oxidation of Fe: rapid hematite nanowire growth and photoelectrochemical water splitting performance. Electrochem Commun 2012;23:59–62.
[59] Hahn NT, Mullins CB. Photoelectrochemical performance of nanostructured Ti- and Sn-doped alpha-Fe_2O_3 photoanodes. Chem Mater 2010;22:6474–82.
[60] Luo ZB, Li CC, Zhang D, et al. Highly-oriented Fe_2O_3/$ZnFe_2O_4$ nanocolumnar heterojunction with improved charge separation for photoelectrochemical water oxidation. Chem Commun 2016;52:9013–5.
[61] Wolcott A, Smith WA, Kuykendall TR, et al. Photoelectrochemical water splitting using dense and aligned TiO_2 nanorod arrays. Small 2009;5:104–11.
[62] Trentler TJ, Hickman KM, Goel SC, et al. Solution-liquid-solid growth of crystalline III-V semiconductors: an analogy to vapor-liquid-solid growth. Science 1995;270:1791–4.
[63] Wang FD, Dong AG, Buhro WE. Solution-liquid-solid synthesis, properties, and applications of one-dimensional colloidal semiconductor nanorods and nanowires. Chem Rev 2016;116:10888–933.
[64] Pei LZ, Zhao HS, Tan W, et al. Hydrothermal oxidization preparation of ZnO nanorods on zinc substrate. Physica E 2010;42:1333–7.
[65] Mukherjee B, Sarker S, Crone E, et al. Engineered solution-liquid-solid growth of a "Treelike" 1D/1D TiO_2 nanotube-CdSe nanowire heterostructure: photoelectrochemical conversion of broad spectrum of solar energy. ACS Appl Mater Interfaces 2016;8:33280–8.
[66] Shin JH, Park SH, Hyun SM, et al. Electrochemical flow-based solution solid growth of the Cu_2O nanorod array: potential application to lithium ion batteries. Phys Chem Chem Phys 2014;16:18226–32.
[67] Wu MH, Wang YX, Xu Y, et al. Self-supported Bi_2MoO_6 nanowall for photoelectrochemical water splitting. ACS Appl Mater Interfaces 2017;9:23647–53.
[68] Byrappa K, Yoshimura M. Handbook of hydrothermal technology Norwich. New York: Noyes Publications; 2001. ISBN 008094681X Chapter 2: History of Hydrothermal Technology.
[69] Guo M, Diao P, Cai SM. Hydrothermal growth of perpendicularly oriented ZnO nanorod array film and its photoelectrochemical properties. Appl Surf Sci 2005;249:71–5.
[70] Yang XY, Wolcott A, Wang GM, et al. Nitrogen-doped ZnO nanowire arrays for photoelectrochemical water splitting. Nano Lett 2009;9:2331–6.
[71] Yu Q, Cao CB. ZnO nanorod arrays for photoelectrochemical cells. J Nanosci Nanotechnol 2012;12:3984–9.
[72] Wang T, Jiao ZB, Chen T, et al. Vertically aligned ZnO nanowire arrays tip-grafted with silver nanoparticles for photoelectrochemical applications. Nanoscale 2013;5:7552–7.
[73] Chen HN, Wei ZH, Yan KY, et al. Epitaxial growth of ZnO nanodisks with large exposed polar facets on nanowire arrays for promoting photoelectrochemical water splitting. Small 2014;10:4760–9.
[74] Hu YP, Yan XQ, Gu YS, et al. Large-scale patterned ZnO nanorod arrays for efficient photoelectrochemical water splitting. Appl Surf Sci 2015;339:122–7.
[75] Kwiatkowski M, Bezverkhyy I, Skompska M. ZnO nanorods covered with a TiO_2 layer: simple sol-gel preparation, and optical, photocatalytic and photoelectrochemical properties. J Mater Chem A 2015;3:12748–60.
[76] Liu YC, Yan XQ, Kang Z, et al. Synergistic effect of surface plasmonic particles and surface passivation layer on ZnO nanorods array for improved photoelectrochemical water splitting. Sci Rep 2016;6:29907.
[77] Yan L, Zhao W, Liu ZF. 1D ZnO/$BiVO_4$ heterojunction photoanodes for efficient photoelectrochemical water splitting. Dalton Trans 2016;45:11346–52.
[78] Wang GM, Wang HY, Ling YC, et al. Hydrogen-treated TiO_2 nanowire arrays for photoelectrochemical water splitting. Nano Lett 2011;11:3026–33.

[79] Cheng CW, Sun Y. Carbon doped TiO_2 nanowire arrays with improved photoelectrochemical water splitting performance. Appl Surf Sci 2012;263:273–6.
[80] Zhou Q, Yang XF, Zhang SQ, et al. Rutile nanowire arrays: tunable surface densities, wettability and photochemistry. J Mater Chem 2011;21:15806–12.
[81] Wang YC, Zhang YY, Tang J, et al. Simultaneous etching and doping of TiO_2 nanowire arrays for enhanced photoelectrochemical performance. ACS Nano 2013;7:9375–83.
[82] Chen HN, Wei ZH, Yan KY, et al. Unveiling two electron-transport modes in oxygen-deficient TiO_2 nanowires and their influence on photoelectrochemical operation. J Phys Chem Lett 2014;5:2890–6.
[83] Cho IS, Logar M, Lee CH, et al. Rapid and controllable flame reduction of TiO_2 nanowires for enhanced solar water-splitting. Nano Lett 2014;14:24–31.
[84] Lou YB, Chen JX. Recent developments in one dimensional (1D) nanostructured TiO_2 for photoelectrochemical water splitting. Nanosci Nanotechnol Lett 2014;6:361–71.
[85] Wang D, Zhang XT, Sun PP, et al. Photoelectrochemical water splitting with rutile TiO_2 nanowires array: synergistic effect of hydrogen treatment and surface modification with anatase nanoparticles. Electrochim Acta 2014;130:290–5.
[86] Pu YC, Ling YC, Chang KD, et al. Surface passivation of TiO_2 nanowires using a facile precursor-treatment approach for photoelectrochemical water oxidation. J Phys Chem C 2014;118:15086–94.
[87] An GW, Mahadik MA, Chae WS, et al. Enhanced solar photoelectrochemical conversion efficiency of the hydrothermally-deposited TiO_2 nanorod arrays: effects of the light trapping and optimum charge transfer. Appl Surf Sci 2018;440:688–99.
[88] Zhou JC, Lin SW, Chen YJ, et al. Facile morphology control of WO_3 nanostructure arrays with enhanced photoelectrochemical performance. Appl Surf Sci 2017;403:274–81.
[89] Su JZ, Feng XJ, Sloppy JD, et al. Vertically aligned WO_3 nanowire arrays grown directly on transparent conducting oxide coated glass: synthesis and photoelectrochemical properties. Nano Lett 2011;11:203–8.
[90] Chen QP, Li JH, Zhou BX, et al. Preparation of well-aligned WO_3 nanoflake arrays vertically grown on tungsten substrate as photoanode for photoelectrochemical water splitting. Electrochem Commun 2012;20:153–6.
[91] Liu Y, Li J, Li WZ, et al. Enhancement of the photoelectrochemical performance of WO_3 vertical arrays film for solar water splitting by gadolinium doping. J Phys Chem C 2015;119:14834–42.
[92] Xiao YH, Xu CQ, Zhang WD. Facile synthesis of Ni-doped WO_3 nanoplate arrays for effective photoelectrochemical water splitting. J Solid State Electr 2017;21:3355–64.
[93] Li WJ, Da PM, Zhang YY, et al. WO_3 Nanoflakes for enhanced photoelectrochemical conversion. ACS Nano 2014;8:11770–7.
[94] Wang QK, Chen YF, Xu JJ, et al. Morphology-controlled synthesis of Ti-doped alpha-Fe_2O_3 nanorod arrays as an efficient photoanode for photoelectrochemical applications. Res Chem Intermediat 2018;44:2365–78.
[95] Zhang R, Fang YY, Chen T, et al. Enhanced photoelectrochemical water oxidation performance of Fe_2O_3 nanorods array by S doping. ACS Sustain Chem Eng 2017;5:7502–6.
[96] Phuan YW, Ong WJ, Chong MN, et al. Prospects of electrochemically synthesized hematite photoanodes for photoelectrochemical water splitting: a review. J Photochem Photobiol C 2017;33:54–82.
[97] Wang J, Su JZ, Guo LJ. Controlled aqueous growth of hematite nanoplate arrays directly on transparent conductive substrates and their photoelectrochemical properties. Chem Asian J 2016;11:2328–34.
[98] Shen SH, Zhou JG, Dong CL, et al. Surface engineered doping of hematite nanorod arrays for improved photoelectrochemical water splitting. Sci Rep 2014;4:6627.
[99] Su JZ, Guo LJ, Yoriya S, et al. Aqueous growth of pyramidal-shaped $BiVO_4$ nanowire arrays and structural characterization: application to photoelectrochemical water splitting. Cryst Growth Des 2010;10:856–61.
[100] He HC, Berglund SP, Rettie AJE, et al. Synthesis of $BiVO_4$ nanoflake array films for photoelectrochemical water oxidation. J Mater Chem A 2014;2:9371–9.
[101] Xiao BC, Lin LY, Hong JY, et al. Synthesis of a monoclinic $BiVO_4$ nanorod array as the photocatalyst for efficient photoelectrochemical water oxidation. RSC Adv 2017;7:7547–54.
[102] Xia XH, Zhu CR, Luo JS, et al. Synthesis of free-standing metal sulfide nanoarrays via anion exchange reaction and their electrochemical energy storage application. Small 2014;10:766–73.
[103] Zhang JJ, Wang T, Chang XX, et al. Fabrication of porous nanoflake $BiMO_x$ (M = W, V, and Mo) photoanodes via hydrothermal anion exchange. Chem Sci 2016;7:6381–6.
[104] Wang Y, Jiang LX, Liu YK, et al. Facile synthesis and photoelectrochemical characterization of Sb_2O_3 nanoprism arrays. J Alloys Compd 2017;727:469–74.
[105] Oh S, Ryu H, Lee WJ. A systematic study of the relationship among the morphological, structural and photoelectrochemical properties of ZnO nanorods grown using the microwave chemical bath deposition method. J Korean Phys Soc 2017;71:171–7.
[106] Zhang HF, Cheng CW. Three-dimensional FTO/TiO_2/$BiVO_4$ composite inverse opals photoanode with excellent photoelectrochemical performance. ACS Energy Lett 2017;2:813–21.
[107] Zhou SJ, Tang R, Zhang LY, et al. Au nanoparticles coupled three-dimensional macroporous $BiVO_4$/SnO_2 inverse opal heterostructure for efficient photoelectrochemical water splitting. Electrochim Acta 2017;248:593–602.
[108] Yan K, Qiu Y, Xiao S, et al. Self-driven hematite-based photoelectrochemical water splitting cells with three-dimensional nanobowl heterojunction and high-photovoltage perovskite solar cells. Mater Today Energy 2017;6:128–35.
[109] Zhang HF, Zhou WW, Yang YP, et al. 3D WO_3/$BiVO_4$/cobalt phosphate composites inverse opal photoanode for efficient photoelectrochemical water splitting. Small 2017;13:1603840.
[110] Zhou YE, Zhang LY, Lin LH, et al. Highly efficient photoelectrochemical water splitting from hierarchical WO_3/$BiVO_4$ nanoporous sphere arrays. Nano Lett 2017;17:8012–7.
[111] Wang WH, Dong JY, Ye XZ, et al. Heterostructured TiO_2 nanorod@nanobowl arrays for efficient photoelectrochemical water splitting. Small 2016;12:1469–78.
[112] Nan F, Kang ZH, Wang JL, et al. Carbon quantum dots coated $BiVO_4$ inverse opals for enhanced photoelectrochemical hydrogen generation. Appl Phys Lett 2015;106:153901.
[113] Yun G, Arunachalam M, Kim HS, et al. Role of WO_3 layers electrodeposited on SnO_2 inverse opal skeletons in photoelectrochemical water splitting. J Phys Chem C 2018;122:9729.
[114] Huang Q, Kang F, Liu H, et al. Highly aligned Cu_2O/CuO/TiO_2 core/shell nanowire arrays as photocathodes for water photoelectrolysis. J Mater Chem A 2013;1:2418–25.
[115] Yuan LX, Meng SQ, Zhou YY, et al. Controlled synthesis of anatase TiO_2 nanotube and nanowire arrays via AAO template-based hydrolysis. J Mater Chem A 2013;1:2552–7.
[116] Zhou M, Bao J, Xu Y, et al. Photoelectrodes based upon Mo: $BiVO_4$ inverse opals for photoelectrochemical water splitting. ACS Nano 2014;8:7088–98.
[117] Nan F, Cai TY, Ju S, et al. Enhanced photoelectrochemical water splitting of $BiVO_4$ photonic crystal photoanode by decorating with MoS_2 nanosheets. Appl Phys Lett 2018;112:173902.
[118] Lee J, Cho CY, Lee DC, et al. Bilayer quantum dot-decorated mesoscopic inverse opals for high volumetric photoelectrochemical water splitting efficiency. RSC Adv 2016;6:8756–62.
[119] Li JK, Qiu YC, Wei ZH, et al. A three-dimensional hexagonal fluorine-doped tin oxide nanocone array: a superior light harvesting electrode for high performance photoelectrochemical water splitting. Energy Environ Sci 2014;7:3651–8.
[120] Su FY, Zhang WD. Fabrication and photoelectrochemical property of In_2O_3/ZnO composite nanotube arrays using ZnO nanorods as self-sacrificing templates. Mater Lett 2018;211:65–8.
[121] Han H, Riboni F, Karlicky F, et al. alpha-Fe_2O_3/TiO_2 3D hierarchical nanostructures for enhanced photoelectrochemical water splitting. Nanoscale 2017;9:134–42.
[122] Qiu YC, Leung SF, Wei ZH, et al. Enhanced charge collection for splitting of water enabled by an engineered three-dimensional nanospike array. J Phys Chem C 2014;118:22465–72.
[123] Qiu JJ, Yu WD, Gao XD, et al. Sol-gel assisted ZnO nanorod array template to synthesize TiO_2 nanotube arrays. Nanotechnology 2006;17:4695–8.
[124] Wang MY, Ioccozia J, Sun L, et al. Inorganic-modified semiconductor TiO_2 nanotube arrays for photocatalysis. Energ Environ Sci 2014;7:2182–202.
[125] Smith YR, Ray RS, Carlson K, et al. Self-ordered titanium dioxide nanotube arrays: anodic synthesis and their photo/electro-catalytic applications. Materials 2013;6:2892–957.
[126] Shao MH, Xu XJ, Huang JZ, et al. TiO_2 nanotube-based composites: synthesis and applications. Sci Adv Mater 2013;5:962–81.
[127] Mor GK, Prakasam HE, Varghese OK, et al. Vertically oriented Ti-Fe-O nanotube array films: toward a useful material architecture for solar spectrum water photoelectrolysis. Nano Lett 2007;7:2356–64.
[128] LaTempa TJ, Feng XJ, Paulose M, et al. Temperature-dependent growth of self-assembled hematite (alpha-Fe_2O_3) nanotube arrays: rapid electrochemical synthesis and photoelectrochemical properties. J Phys Chem C 2009;113:16293–8.
[129] Qi XP, She GW, Wang M, et al. Electrochemical synthesis of p-type Zn-doped alpha-Fe_2O_3 nanotube arrays for photoelectrochemical water splitting. Chem Commun 2013;49:5742–4.
[130] Peerakiatkhajohn P, Yun JH, Chen HJ, et al. Stable hematite nanosheet photoanodes for enhanced photoelectrochemical water splitting. Adv Mater 2016;28:6405.
[131] Goncalves RV, Migowski P, Wender H, et al. On the crystallization of Ta_2O_5 nanotubes: structural and local atomic properties investigated by EXAFS and XRD. CrystEngComm 2014;16:797–804.
[132] Mor GK, Varghese OK, Paulose M, et al. A review on highly ordered, vertically oriented TiO_2 nanotube arrays: fabrication, material properties, and solar energy applications. Sol Energy Mater Sol C 2006;90:2011–75.
[133] Yang LX, Luo SL, Cai QY, et al. A review on TiO_2 nanotube arrays: fabrication, properties, and sensing applications. Chin Sci Bull 2010;55:331–8.
[134] Morales AGR, Guzman MOC, Arteaga CC. A brief review on fabrication and applications of auto-organized TiO_2 nanotube arrays. Corros Rev 2011;29:105–21.
[135] Pang YL, Lim S, Ong HC, et al. A critical review on the recent progress of synthesizing techniques and fabrication of TiO_2-based nanotubes photocatalysts. Appl Catal A Gen 2014;481:127–42.
[136] Gui QF, Xu Z, Zhang HF, et al. Enhanced photoelectrochemical water splitting performance of anodic TiO_2 nanotube arrays by surface passivation. ACS Appl Mater Interfaces 2014;6:17053–8.

[137] Ge MZ, Li QS, Cao CY, et al. One-dimensional TiO_2 nanotube photocatalysts for solar water splitting. Adv Sci 2017;4:1600152.
[138] Huang JY, Zhang KQ, Lai YK. Fabrication, modification, and emerging applications of TiO_2 nanotube arrays by electrochemical synthesis: a review. Int J Photoenergy 2013;2013:761971.
[139] Wang L, Lee CY, Kirchgeorg R, et al. Anodic self-organized transparent nanotubular/porous hematite films from Fe thin-films sputtered on FTO and photoelectrochemical water splitting. Res Chem Intermediat 2015;41:9333–41.
[140] Wang HW, Tian J, Li WB. Electrochemical deposition of MgO@ZnO shell-core nanorod arrays largely enhances the photoelectrochemical water splitting performance. ChemElectroChem 2017;4:2019–26.
[141] Li HH, Zhang WW, Xu WL, et al. Fabrication of CeO_2@CdS sub-micron rod arrays for enhanced photoelectrochemical performance. Inorg Chem Commun 2017;83:59–61.
[142] Shinde PS, Mahadik MA, Lee SY, et al. Surfactant and TiO_2 underlayer derived porous hematite nanoball array photoanode for enhanced photoelectrochemical water oxidation. Chem Eng J 2017;320:81–92.
[143] Ren X, Sangle A, Zhang SY, et al. Photoelectrochemical water splitting strongly enhanced in fast-grown ZnO nanotree and nanocluster structures. J Mater Chem A 2016;4:10203–11.
[144] Rokade A, Rondiya S, Sharma V, et al. Electrochemical synthesis of 1D ZnO nanoarchitectures and their role in efficient photoelectrochemical splitting of water. J Solid State Electr 2017;21:2639–48.
[145] Mao YC, Yang H, Chen JX, et al. Significant performance enhancement of ZnO photoanodes from $Ni(OH)_2$ electrocatalyst nanosheets overcoating. Nano Energy 2014;6:10–8.
[146] Tena-Zaera R, Elias J, Levy-Clement C. Electrodeposition of ZnO nanowire arrays with tailored dimensions: building blocks for photoelectrochemical devices. Proc SPIE 2007;6650.
[147] Qiu JH, Guo M, Feng YJ, et al. Electrochemical deposition of branched hierarchical ZnO nanowire arrays and its photoelectrochemical properties. Electrochim Acta 2011;56:5776–82.
[148] Han L, Hu P, Xu ZK, et al. Electrodeposition and photoelectrochemical properties of p-type BiOI alpha Cl1-alpha nanoplatelet thin films. Electrochim Acta 2014;115:263–8.
[149] Lu XH, Zheng DZ, Zhang P, et al. Facile synthesis of free-standing CeO_2 nanorods for photoelectrochemical applications. Chem Commun 2010;46:7721–3.
[150] Roza L, Rahman MYA, Umar AA, et al. Direct growth of oriented ZnO nanotubes by self-selective etching at lower temperature for photo-electrochemical (PEC) solar cell application. J Alloys Compd 2015;618:153–8.
[151] Wang P, Wang D, Lin J, et al. Lattice defect-enhanced hydrogen production in nanostructured hematite-based photoelectrochemical device. ACS Appl Mater Interfaces 2012;4:2295–302.
[152] She GW, Zhang XH, Shi WS, et al. Electrochemical/chemical synthesis of highly-oriented single-crystal ZnO nanotube arrays on transparent conductive substrates. Electrochem Commun 2007;9:2784–8.
[153] Li CC, Li A, Luo ZB, et al. Surviving high-temperature calcination: ZrO_2-induced hematite nanotubes for photoelectrochemical water oxidation. Angew Chem Int Ed 2017;56:4150–5.
[154] Luo ZB, Wang T, Zhang JJ, et al. Dendritic hematite nanoarray photoanode modified with a conformal titanium dioxide interlayer for effective charge collection. Angew Chem Int Ed 2017;56:12878–82.
[155] Morrish R, Rahman M, MacElroy JMD, et al. Activation of hematite nanorod arrays for photoelectrochemical water splitting. ChemSusChem 2011;4:474–9.
[156] Qin DD, Tao CL, In SI, et al. Facile solvothermal method for fabricating arrays of vertically oriented alpha-Fe_2O_3 nanowires and their application in photoelectrochemical water oxidation. Energy Fuel 2011;25:5257–63.
[157] Li LS, Yu YH, Meng F, et al. Facile solution synthesis of alpha-FeF_3 center dot $3H_2O$ nanowires and their conversion to alpha-Fe_2O_3 nanowires for photoelectrochemical application. Nano Lett 2012;12:724–31.
[158] Wang CW, Yang S, Jiang HB, et al. Chemical vapor deposition of FeOCl nanosheet arrays and their conversion to porous alpha-Fe_2O_3 photoanodes for photoelectrochemical water splitting. Chem Eur J 2015;21:18024–8.
[159] Qiu YC, Yan KY, Deng H, et al. Secondary branching and nitrogen doping of ZnO nanotetrapods: building a highly active network for photoelectrochemical water splitting. Nano Lett 2012;12:407–13.
[160] Cheng CW, Yan B, Wong SM, et al. Fabrication and SERS performance of silver-nanoparticle-decorated Si/ZnO nanotrees in ordered arrays. ACS Appl Mater Interfaces 2010;2:1824–8.
[161] Dick KA, Deppert K, Larsson MW, et al. Synthesis of branched "nanotrees" by controlled seeding of multiple branching events. Nat Mater 2004;3:380–4.
[162] Park S, Kim HJ, Lee CW, et al. Sn self-doped alpha-Fe_2O_3 nanobranch arrays supported on a transparent, conductive SnO_2 trunk to improve photoelectrochemical water oxidation. Int J Hydrog Energy 2014;39:16459–67.
[163] Zhang X, Liu Y, Kang ZH. 3D branched ZnO nanowire arrays decorated with plasmonic Au nanoparticles for high-performance photoelectrochemical water splitting. ACS Appl Mater Interfaces 2014;6:4480–9.
[164] Hou TF, Boppella R, Shanmugasundaram A, et al. Hierarchically self-assembled ZnO architectures: establishing light trapping networks for effective photoelectrochemical water splitting. Int J Hydrog Energy 2017;42:15126–39.
[165] Liu BK, Sun YJ, Wang DJ, et al. Construction of a branched ZnO-TiO_2 nanorod array heterostructure for enhancing the photovoltaic properties in quantum dot-sensitized solar cells. RSC Adv 2014;4:32773–80.
[166] Gu F, Gai LL, Shao W, et al. Heteroepitaxial growth of ZnO branches selectively on TiO_2 nanorod tips with improved light harvesting performance. Chem Commun 2011;47:8400–2.
[167] Noh SY, Sun K, Choi C, et al. Branched TiO_2/Si nanostructures for enhanced photoelectrochemical water splitting. Nano Energy 2013;2:351–60.
[168] Yuan KP, Cao Q, Li XY, et al. Synthesis of WO_3@$ZnWO_4$@ZnO-ZnO hierarchical nanocactus arrays for efficient photoelectrochemical water splitting. Nano Energy 2017;41:543–51.
[169] Li YG, Wei XL, Zhu BW, et al. Hierarchically branched Fe_2O_3@TiO_2 nanorod arrays for photoelectrochemical water splitting: facile synthesis and enhanced photoelectrochemical performance. Nanoscale 2016;8:11284–90.
[170] Gao CT, Zhang ZM, Li XD, et al. Synergistic effects in three-dimensional SnO_2/TiO_2/CdS multi-heterojunction structure for highly efficient photoelectrochemical hydrogen production. Sol Energy Mater Sol C 2015;141:101–7.
[171] Pan ZH, Qiu YC, Yang J, et al. Synthesis of three-dimensional hyperbranched TiO_2 nanowire arrays with significantly enhanced photoelectrochemical hydrogen production. J Mater Chem A 2015;3:4004–9.
[172] Wang H, Bai YS, Wu QO, et al. Rutile TiO_2 nano-branched arrays on FTO for dye-sensitized solar cells. Phys Chem Chem Phys 2011;13:7008–13.
[173] Wu CT, Liao WP, Wu JJ. Three-dimensional ZnO nanodendrite/nanoparticle composite solar cells. J Mater Chem 2011;21:2871–6.
[174] Cho IS, Chen ZB, Forman AJ, et al. Branched TiO_2 nanorods for photoelectrochemical hydrogen production. Nano Lett 2011;11:4978–84.
[175] Yang XF, Zhuang JL, Li XY, et al. Hierarchically nanostructured rutile arrays. Acid vapor oxidation growth and tunable morphologies. ACS Nano 2009;3:1212–8.
[176] Zhang ZM, Gao CT, Wu ZM, et al. Toward efficient photoelectrochemical water-splitting by using screw-like SnO_2 nanostructures as photoanode after being decorated with CdS quantum dots. Nano Energy 2016;19:318–27.
[177] Yao CZ, Wei BH, Ma HX, et al. Enhanced photoelectrochemical performance of hydrogenated ZnO hierarchical nanorod arrays. J Power Sources 2013;237:295–9.
[178] Zhou W, Cheng C, Liu JP, et al. Epitaxial growth of branched alpha-Fe_2O_3/SnO_2 nano-heterostructures with improved lithium-ion battery performance. Adv Funct Mater 2011;21:2439–45.
[179] Hou Y, Zuo F, Dagg AP, et al. Branched WO_3 nanosheet array with layered C_3N_4 heterojunctions and CoO_x nanoparticles as a flexible photoanode for efficient photoelectrochemical water oxidation. Adv Mater 2014;26:5043–9.
[180] Pathan HM, Lokhande CD. Deposition of metal chalcogenide thin films by successive ionic layer adsorption and reaction (SILAR) method. Bull Mater Sci 2004;27:85–111.
[181] Wang QY, Qiao JL, Zhou J. Fabrication of Ag@Ag_2S core-shell nanoparticles sensitized TiO_2 nanotube arrays with high photoelectrochemical properties. ECS J Solid State Sci Technol 2014;3:Q157–61.
[182] Tang L, Deng YC, Zeng GM, et al. CdS/Cu_2S co-sensitized TiO_2 branched nanorod arrays of enhanced photoelectrochemical properties by forming nanoscale heterostructure. J Alloys Compd 2016;662:516–27.
[183] Zhang XM, Wang B, Liu ZQ. Tuning PbS QDs deposited onto TiO_2 nanotube arrays to improve photoelectrochemical performances. J Colloid Interface Sci 2016;484:213–9.
[184] Ouyang WX, Yu YX, Zhang WD. High and stable photoelectrochemical activity of ZnO/ZnSe/CdSe/Cu_xS core-shell nanowire arrays: nanoporous surface with Cu_xS as a hole mediator. Phys Chem Chem Phys 2015;17:14827–35.
[185] Li C, Zhang HF, Cheng CW. CdS/CdSe co-sensitized 3D SnO_2/TiO_2 sea urchin-like nanotube arrays as an efficient photoanode for photoelectrochemical hydrogen generation. RSC Adv 2016;6:37407–11.
[186] Kim DH, Han HS, Cho IS, et al. CdS-sensitized 1-D single-crystalline anatase TiO_2 nanowire arrays for photoelectrochemical hydrogen production. Int J Hydrog Energy 2015;40:863–9.
[187] Wang GM, Yang XY, Qian F, et al. Double-sided CdS and CdSe quantum dot Co-sensitized ZnO nanowire arrays for photoelectrochemical hydrogen generation. Nano Lett 2010;10:1088–92.
[188] Zhang R, Luo QP, Chen HY, et al. CdS/CdSe Quantum dot shell decorated vertical ZnO nanowire arrays by spin-coating-based SILAR for photoelectrochemical cells and quantum-dot-sensitized solar cells. ChemPhysChem 2012;13:1435–9.
[189] Fan XL, Wang T, Gao B, et al. Preparation of the TiO_2/graphic carbon nitride core-shell array as a photoanode for efficient photoelectrochemical water splitting. Langmuir 2016;32:13322–32.
[190] Zhang J, Bang JH, Tang CC, et al. Tailored TiO_2-$SrTiO_3$ heterostructure nanotube arrays for improved photoelectrochemical performance. ACS Nano 2010;4:387–95.
[191] Yun G, Balarmurugan M, Kim HS, et al. Role of WO_3 layers electrodeposited on SnO_2 inverse opal skeletons in photoelectrochemical water splitting. J Phys Chem C 2016;120:5906–15.
[192] Fu XL, Ji ZB, Li CB, et al. Electrochemical method for synthesis of Cu_2ZnSnS_4 Nanorod/TiO_2 nanotube arrays hybrid structure with enhanced photoelectrochemical properties. J Alloys Compd 2016;688:1013–8.
[193] Liu Q, Cao FR, Wu FL, et al. Interface reacted $ZnFe_2O_4$ on alpha-Fe_2O_3 nanoarrays for largely improved photoelectrochemical activity. RSC Adv 2015;5:79440–6.
[194] Xi LF, Chiam SY, Mak WF, et al. A novel strategy for surface treatment on hematite photoanode for efficient water oxidation. Chem Sci 2013;4:164–9.
[195] Li CC, Wang T, Luo ZB, et al. Enhanced charge separation through ALD-modified Fe_2O_3/Fe_2TiO_5 nanorod heterojunction for photoelectrochemical water oxidation. Small 2016;12:3415.

[196] Qiu YC, Leung SF, Zhang QP, et al. Efficient photoelectrochemical water splitting with ultrathin films of hematite on three-dimensional nanophotonic structures. Nano Lett 2014;14:2123–9.
[197] Hussain S, Hussain S, Waleed A, et al. Fabrication of $CuFe_2O_4$/alpha-Fe_2O_3 composite thin films on FTO coated glass and 3-D nanospike structures for efficient photoelectrochemical water splitting. ACS Appl Mater Interfaces 2016;8:35315–22.
[198] Hussain S, Tayakoli MM, Waleed A, et al. Nanotextured spikes of alpha-Fe_2O_3/$NiFe_2O_4$ composite for efficient photoelectrochemical oxidation of water. Langmuir 2018;34:3555–64.
[199] Hussain S, Hussain S, Waleed A, et al. Spray pyrolysis deposition of $ZnFe_2O_4$/Fe_2O_3 composite thin films on hierarchical 3-D nanospikes for efficient photoelectrochemical oxidation of water. J Phys Chem C 2017;121:18360–8.
[200] Qiu YC, Liu W, Chen W, et al. Efficient solar-driven water splitting by nanocone $BiVO_4$-perovskite tandem cells. Sci Adv 2016;2:e1501764.
[201] Jang JS, Ahn CW, Won SS, et al. Vertically aligned core-shell $PbTiO_3$@TiO_2 heterojunction nanotube array for photoelectrochemical and photocatalytic applications. J Phys Chem C 2017;121:15063–70.
[202] Liu CH, Wang F, Zhang J, et al. Efficient photoelectrochemical water splitting by g-C_3N_4/TiO_2 nanotube array heterostructures. Nano-Micro Lett 2018;10:37.
[203] Xiao YH, Zhang WD. MoS_2 quantum dots interspersed WO_3 nanoplatelet arrays with enhanced photoelectrochemical activity. Electrochim Acta 2017;252:416–23.
[204] Rao PM, Cai LL, Liu C, et al. Simultaneously efficient light absorption and charge separation in WO_3/$BiVO_4$ core/shell nanowire photoanode for photoelectrochemical water oxidation. Nano Lett 2014;14:1099–105.
[205] Balamurugan M, Yun G, Ahn KS, et al. Revealing the beneficial effects of $FeVO_4$ nanoshell layer on the $BiVO_4$ inverse opal core layer for photoelectrochemical water oxidation. J Phys Chem C 2017;121:7625–34.
[206] Hou Y, Zuo F, Dagg A, et al. A three-dimensional branched cobalt-doped alpha-Fe_2O_3 nanorod/$MgFe_2O_4$ heterojunction array as a flexible photoanode for efficient photoelectrochemical water oxidation. Angew Chem Int Ed 2013;52:1248–52.
[207] Luo JS, Ma L, He TC, et al. TiO_2/(CdS, CdSe, CdSeS) nanorod heterostructures and photoelectrochemical properties. J Phys Chem C 2012;116:11956–63.
[208] Zhou J, Zhou AW, Shu L, et al. Cellular heterojunctions fabricated through the sulfurization of MOFs onto ZnO for high-efficient photoelectrochemical water oxidation. Appl Catal B Environ 2018;226:421–8.
[209] Luo JS, Steier L, Son MK, et al. Cu_2O nanowire photocathodes for efficient and durable solar water splitting. Nano Lett 2016;16:1848–57.
[210] Yuan WY, Yuan J, Xie JL, et al. Polymer-mediated self-assembly of TiO_2@Cu_2O core-shell nanowire array for highly efficient photoelectrochemical water oxidation. ACS Appl Mater Interfaces 2016;8:6082–92.
[211] Yan J, Yang SY, Xie ZK, et al. Heterostructured CoO/3D-TiO_2 nanorod arrays for photoelectrochemical water splitting hydrogen production. J Solid State Electr 2017;21:455–61.
[212] Hao CC, Wang WZ, Zhang R, et al. Enhanced photoelectrochemical water splitting with TiO_2@Ag_2O nanowire arrays via p-n heterojunction formation. Sol Energy Mater Sol C 2018;174:132–9.
[213] Lakehal S, Achour S, Ferrari C, et al. Photoelectrochemical properties of ZnO nanorods decorated with Cu and Cu_2O nanoparticles. Superlattice Microstruct 2014;72:253–61.
[214] Kang Z, Yan XQ, Wang YF, et al. Electronic structure engineering of Cu_2O film/ZnO nanorods array all-oxide p-n heterostructure for enhanced photoelectrochemical property and self-powered biosensing application. Sci Rep 2015;5:7882.
[215] Ahn HJ, Yoon KY, Kwak MJ, et al. MoS_x supported hematite with enhanced photoelectrochemical performance. J Mater Chem A 2015;3:21444–50.
[216] Huang B, Yang WJ, Wen YW, et al. Co_3O_4-modified TiO_2 nanotube arrays via atomic layer deposition for improved visible-light photoelectrochemical performance. Acs Appl Mater Interfaces 2015;7:422–31.
[217] Zhou FQ, Fan JC, Xu QJ, et al. $BiVO_4$ nanowires decorated with CdS nanoparticles as Z-scheme photocatalyst with enhanced H_2 generation. Appl Catal B Environ 2017;201:77–83.
[218] Cho KH, Sung YM. The formation of Z-scheme CdS/CdO nanorods on FTO substrates: the shell thickness effects on the flat band potentials. Nano Energy 2017;36:176–85.
[219] Hwang YJ, Boukai A, Yang PD. High density n-Si/n-TiO_2 core/shell nanowire arrays with enhanced photoactivity. Nano Lett 2009;9:410–5.
[220] Li YG, Feng J, Li HJ, et al. Photoelectrochemical splitting of natural seawater with alpha-Fe_2O_3/WO_3 nanorod arrays. Int J Hydrog Energy 2016;41:4096–105.
[221] Wang L, Zhou XM, Nguyen NT, et al. Plasmon-enhanced photoelectrochemical water splitting using Au nanoparticles decorated on hematite nanoflake arrays. ChemSusChem 2015;8:618–22.
[222] Feng DY, Rui ZB, Lu YB, et al. A simple method to decorate TiO_2 nanotube arrays with controllable quantity of metal nanoparticles. Chem Eng J 2012;179:363–71.
[223] Zhang ZH, Zhang LB, Hedhili MN, et al. Plasmonic gold nanocrystals coupled with photonic crystal seamlessly on TiO_2 nanotube photoelectrodes for efficient visible light photoelectrochemical water splitting. Nano Lett 2013;13:14–20.
[224] Chen JN, Yu M, Wang YH, et al. Au@SiO_2 core/shell nanoparticle-decorated TiO_2 nanorod arrays for enhanced photoelectrochemical water splitting. Chin Sci Bull 2014;59:2191–8.
[225] Xiao FX. Layer-by-layer self-assembly construction of highly ordered metal-TiO_2 nanotube arrays heterostructures (M/TNTs, M = Au, Ag, Pt) with tunable catalytic activities. J Phys Chem C 2012;116:16487–98.
[226] Guo K, Liu ZF, Han JH, et al. Higher-efficiency photoelectrochemical electrodes of titanium dioxide-based nanoarrays sensitized simultaneously with plasmonic silver nanoparticles and multiple metal sulfides photosensitizers. J Power Sources 2015;285:185–94.
[227] Yang L, Chu DL, Chen Y, et al. Photoelectrochemical properties of Ag/TiO_2 electrodes constructed using vertically oriented two-dimensional TiO_2 nanosheet array films. J Electrochem Soc 2016;163:H180–5.
[228] Li HX, Li ZD, Yu YH, et al. Surface-plasmon-resonance-enhanced photoelectrochemical water splitting from Au-nanoparticle-decorated 3D TiO_2 nanorod architectures. J Phys Chem C 2017;121:12071–9.
[229] Xu F, Mei JJ, Zheng MQ, et al. Au nanoparticles modified branched TiO_2 nanorod array arranged with ultrathin nanorods for enhanced photoelectrochemical water splitting. J Alloys Compd 2017;693:1124–32.
[230] Fang LL, Wang XZ, Wang Z, et al. Heterostructured TiO_2 nanotree arrays with silver quantum dots loading for enhanced photoelectrochemical properties. J Alloys Compd 2018;730:110–8.
[231] Zhang CL, Shao MF, Ning FY, et al. Au nanoparticles sensitized ZnO nanorod@nanoplatelet core-shell arrays for enhanced photoelectrochemical water splitting. Nano Energy 2015;12:231–9.
[232] Lu Y, Zhang JL, Ge L, et al. Synthesis of novel AuPd nanoparticles decorated one-dimensional ZnO nanorod arrays with enhanced photoelectrochemical water splitting activity. J Colloid Interface Sci 2016;483:146–53.
[233] Yang XG, Liu R, He YM, et al. Enabling practical electrocatalyst-assisted photoelectron-chemical water splitting with earth abundant materials. Nano Res 2015;8:56–81.
[234] Zhang ZH, Dua R, Zhang LB, et al. Carbon-layer-protected cuprous oxide nanowire arrays for efficient water reduction. ACS Nano 2013;7:1709–17.
[235] Shalom M, Dor S, Ruhle S, et al. Core/CdS quantum dot/Shell mesoporous solar cells with improved stability and efficiency using an amorphous TiO_2 coating. J Phys Chem C 2009;113:3895–8.
[236] Campet G, Puprichitkun C, Sun ZW. Protection of photoanodes against photocorrosion by surface deposition of oxide films: criteria for choosing the protective coating. J Electroanal Chem Interfacial Electrochem 1989;29:435–45.
[237] Cheng Q, Benipal MK, Liu QL, et al. Al_2O_3 and SiO_2 atomic layer deposition layers on ZnO photoanodes and degradation mechanisms. ACS Appl Mater Interfaces 2017;9:16138–47.
[238] Hwang YJ, Hahn C, Liu B, et al. Photoelectrochemical properties of TiO_2 nanowire arrays: a study of the dependence on length and atomic layer deposition coating. ACS Nano 2012;6:5060–9.
[239] Le Formal F, Tetreault N, Cornuz M, et al. Passivating surface states on water splitting hematite photoanodes with alumina overlayers. Chem Sci 2011;2:737–43.
[240] Chen YW, Prange JD, Duhnen S, et al. Atomic layer-deposited tunnel oxide stabilizes silicon photoanodes for water oxidation. Nat Mater 2011;10:539–44.
[241] Hu S, Shaner MR, Beardslee JA, et al. Amorphous TiO_2 coatings stabilize Si, GaAs, and GaP photoanodes for efficient water oxidation. Science 2014;344:1005–9.
[242] Kenney MJ, Gong M, Li YG, et al. High-performance silicon photoanodes passivated with ultrathin nickel films for water oxidation. Science 2013;342:836–40.
[243] Lin CY, Lai YH, Mersch D, et al. Cu_2O vertical bar NiO_x nanocomposite as an inexpensive photocathode in photoelectrochemical water splitting. Chem Sci 2012;3:3482–7.
[244] Martinez-Garcia A, Vendra VK, Sunkara S, et al. Tungsten oxide-coated copper oxide nanowire arrays for enhanced activity and durability with photoelectrochemical water splitting. J Mater Chem A 2013;1:15235–41.
[245] Li X, Liu SW, Fan K, et al. MOF-based transparent passivation layer modified ZnO nanorod arrays for enhanced photo-electrochemical water splitting. Adv Energy Mater 2018;8:1800101.
[246] Hernandez S, Cauda V, Chiodoni A, et al. Optimization of 1D ZnO@TiO_2 core-shell nanostructures for enhanced photoelectrochemical water splitting under solar light illumination. ACS Appl Mater Interfaces 2014;6:12153–67.
[247] Kwiatkowski M, Chassagnon R, Heintz O, et al. Improvement of photocatalytic and photoelectrochemical activity of ZnO/TiO_2 core/shell system through additional calcination: insight into the mechanism. Appl Catal B Environ 2017;204:200–8.
[248] Sarkar A, Singh AK, Khan GG, et al. TiO_2/ZnO core/shell nano-heterostructure arrays as photo-electrodes with enhanced visible light photoelectrochemical performance. RSC Adv 2014;4:55629–34.
[249] Shi WN, Zhang XF, Li SH, et al. Carbon coated Cu_2O nanowires for photo-electrochemical water splitting with enhanced activity. Appl Surf Sci 2015;358:404–11.
[250] Tong XL, Yang P, Wang YW, et al. Enhanced photoelectrochemical water splitting performance of TiO_2 nanotube arrays coated with an ultrathin nitrogen-doped carbon film by molecular layer deposition. Nanoscale 2014;6:6692–700.
[251] Dasgupta NP, Lee HBR, Bent SF, et al. Recent advances in atomic layer deposition. Chem Mater 2016;28:1943–7.
[252] Liu R, Zheng Z, Spurgeon J, et al. Enhanced photoelectrochemical water-splitting performance of semiconductors by surface passivation layers. Energy Environ Sci 2014;7:2504–17.

[253] Shin SW, Suryawanshi MP, Hong HK, et al. Strategy for enhancing the solar-driven water splitting performance of TiO_2 nanorod arrays with thin Zn(O, S) passivated layer by atomic layer deposition. Electrochim Acta 2016;219:470–81.

[254] Singh T, Lehnen T, Leuning T, et al. Atomic layer deposition grown MO_x thin films for solar water splitting: prospects and challenges. J Vac Sci Technol A 2015;33:010801.

[255] Li XL, Bassi PS, Boix PP, et al. Revealing the role of TiO_2 surface treatment of hematite nanorods photoanodes for solar water splitting. ACS Appl Mater Interfaces 2015;7:16960–6.

[256] Schiper DE, Zhao ZH, Leitner AP, et al. A TiO_2/FeMnP core/shell nanorod array photoanode for efficient photoelectrochemical oxygen evolution. ACS Nano 2017;11:4051–9.

[257] Liu CH, Wang F, Qiu YY, et al. Facile electrodeposition of cobalt hydroxide on anodic TiO_2 nanotubes arrays for enhanced photoelectrochemical application. J Photochem Photobiol A 2018;353:200–5.

[258] Shao MF, Ning FY, Wei M, et al. Hierarchical nanowire arrays based on ZnO core-layered double hydroxide shell for largely enhanced photoelectrochemical water splitting. Adv Funct Mater 2014;24:580–6.

[259] Davi M, Mann M, Ma ZL, et al. An MnNCN-derived electrocatalyst for $CuWO_4$ photoanodes. Langmuir 2018;34:3845–52.

[260] Mao YC, Cheng YG, Wang JQ, et al. Amorphous NiO electrocatalyst overcoated ZnO nanorod photoanodes for enhanced photoelectrochemical performance. New J Chem 2016;40:107–12.

[261] Feng KJ, Li W, Xie SL, et al. Nickel hydroxide decorated hydrogenated zinc oxide nanorod arrays with enhanced photoelectrochemical performance. Electrochim Acta 2014;137:108–13.

[262] Ye KH, Wang ZL, Li HB, et al. A novel CoOOH/(Ti, C)-Fe_2O_3 nanorod photoanode for photoelectrochemical water splitting. Sci China Mater 2018;61:887–94.

[263] Ai GJ, Mo R, Li HX, et al. Cobalt phosphate modified TiO_2 nanowire arrays as co-catalysts for solar water splitting. Nanoscale 2015;7:6722–8.

[264] Trzcinski K, Szkoda M, Siuzdak K, et al. Electrochemical and photoelectrochemical characterization of photoanodes based on titania nanotubes modified by a $BiVO_4$ thin film and gold nanoparticles. Electrochim Acta 2016;222:421–8.

[265] Yin RY, Liu MY, Tang R, et al. CdS nanoparticle-modified alpha-Fe_2O_3/TiO_2 nanorod array photoanode for efficient photoelectrochemical water oxidation. Nanoscale Res Lett 2017;12.

[266] Zhang Y, Nie JT, Wang Q, et al. Synthesis of Co_3O_4/Ag/TiO_2 nanotubes arrays via photo-deposition of Ag and modification of Co_3O_4 (3 1 1) for enhancement of visible-light photoelectrochemical performance. Appl Surf Sci 2018;427:1009–18.

[267] Luo J, Li DL, Yang Y, et al. Preparation of Au/reduced graphene oxide/hydrogenated TiO_2 nanotube arrays ternary composites for visible-light-driven photoelectrochemical water splitting. J Alloys Compd 2016;661:380–8.

[268] Peng Q, Wang J, Feng ZJ, et al. Enhanced photoelectrochemical water oxidation by fabrication of p-$LaFeO_3$/n-Fe_2O_3 heterojunction on hematite nanorods. J Phys Chem C 2017;121:12991–8.

[269] Feng X, Shankar K, Varghese OK, et al. Vertically aligned single crystal TiO_2 nanowire arrays grown directly on transparent conducting oxide coated glass: synthesis details and applications. Nano Lett 2008;8:3781–6.

[270] Mao C, Zuo F, Hou Y, et al. In situ preparation of a Ti^{3+} self-doped TiO_2 film with enhanced activity as photoanode by N_2H_4 reduction. Angew Chem Int Ed 2014;53:10485–9.

[271] Hoang S, Guo SW, Hahn NT, et al. Visible light driven photoelectrochemical water oxidation on nitrogen-modified TiO_2 nanowires. Nano Lett 2012;12:26–32.

[272] Hoang S, Berglund SP, Hahn NT, et al. Enhancing visible light photo-oxidation of water with TiO_2 nanowire arrays via cotreatment with H_2 and NH_3: synergistic effects between Ti^{3+} and N. J Am Chem Soc 2012;134:3659–62.

[273] Qin DD, Wang QH, Chen J, et al. Phosphorus-doped TiO_2 nanotube arrays for visible-light-driven photoelectrochemical water oxidation. Sust Energy Fuels 2017;1:248–53.

[274] Gopal NO, Lo HH, Ke TF, et al. Visible light active phosphorus-doped TiO_2 nanoparticles: an EPR evidence for the enhanced charge separation. J Phys Chem C 2012;116:16191–7.

[275] Fang WQ, Huo ZY, Liu PR, et al. Fluorine-doped porous single-crystal rutile TiO_2 nanorods for enhancing photoelectrochemical water splitting. Chem Eur J 2014;20:11439–44.

[276] Xu M, Da PM, Wu HY, et al. Controlled Sn-doping in TiO_2 nanowire photoanodes with enhanced photoelectrochemical conversion. Nano Lett 2012;12:1503–8.

[277] Wang C, Chen Z, Jin H, et al. Enhancing visible-light photoelectrochemical water splitting through transition-metal doped TiO_2 nanorod arrays. J Mater Chem A 2014;2:17820–7.

[278] Tian Z, Cui H, Xu J, et al. Efficient charge separation of in-Situ Nb-doped TiO_2 nanowires for photoelectrochemical water-splitting. ChemistrySelect 2017;2:2822–7.

[279] Cho IS, Lee CH, Feng Y, et al. Codoping titanium dioxide nanowires with tungsten and carbon for enhanced photoelectrochemical performance. Nat Commun 2013;4:1723.

[280] Aragaw BA, Pan C-J, Su W-N, et al. Facile one-pot controlled synthesis of Sn and C codoped single crystal TiO_2 nanowire arrays for highly efficient photoelectrochemical water splitting. Appl Catal B Environ 2015;163:478–86.

[281] Pu Y-C, Wang G, Chang K-D, et al. Au nanostructure-decorated TiO_2 nanowires exhibiting photoactivity across entire UV-visible region for photoelectrochemical water splitting. Nano Lett 2013;13:3817–23.

[282] Sudhagar P, Song T, Devadoss A, et al. Modulating the interaction between gold and TiO_2 nanowires for enhanced solar driven photoelectrocatalytic hydrogen generation. Phys Chem Chem Phys 2015;17:19371–8.

[283] Peng C, Wang W, Zhang W, et al. Surface plasmon-driven photoelectrochemical water splitting of TiO_2 nanowires decorated with Ag nanoparticles under visible light illumination. Appl Surf Sci 2017;420:286–95.

[284] Youngblood WJ, Lee S-HA, Maeda K, et al. Visible light water splitting using dye-sensitized oxide semiconductors. Accounts Chem Res 2009;42:1966–73.

[285] Swierk JR, Mallouk TE. Design and development of photoanodes for water-splitting dye-sensitized photoelectrochemical cells. Chem Soc Rev 2013;42:2357–87.

[286] Resasco J, Zhang H, Kornienko N, et al. TiO_2/$BiVO_4$ nanowire heterostructure photoanodes based on type II band alignment. ACS Central Sci 2016;2:80–8.

[287] Yoon H, Mali MG, Choi JY, et al. Nanotextured pillars of electrosprayed bismuth vanadate for efficient photoelectrochemical water splitting. Langmuir 2015;31:3727–37.

[288] Su J, Geng P, Li X, et al. Graphene-linked graphitic carbon nitride/TiO_2 nanowire arrays heterojunction for efficient solar-driven water splitting. J Appl Electrochem 2016;46:807–17.

[289] Wei Q, Yan X, Kang Z, et al. Carbon quantum dots decorated C_3N_4/TiO_2 heterostructure nanorod arrays for enhanced photoelectrochemical performance. J Electrochem Soc 2017;164:H515–20.

[290] Liu N, Chen X, Zhang J, et al. A review on TiO_2-based nanotubes synthesized via hydrothermal method: formation mechanism, structure modification, and photocatalytic applications. Catal Today 2014;225:34–51.

[291] Hoyer P. Formation of a titanium dioxide nanotube array. Langmuir 1996;12:1411–3.

[292] Lee J-H, Leu I-C, Hsu M-C, et al. Fabrication of aligned TiO_2 one-dimensional nanostructured arrays using a one-step templating solution approach. J Phys Chem B 2005;109:13056–9.

[293] Chen S, Thind SS, Chen A. Nanostructured materials for water splitting – state of the art and future needs: a mini-review. Electrochem Commun 2016;63:10–7.

[294] Zhou M, Lou XW, Xie Y. Two-dimensional nanosheets for photoelectrochemical water splitting: possibilities and opportunities. Nano Today 2013;8:598–618.

[295] Mor GK, Shankar K, Paulose M, et al. Enhanced photocleavage of water using titania nanotube arrays. Nano Lett 2005;5:191–5.

[296] Gong D, Grimes CA, Varghese OK, et al. Titanium oxide nanotube arrays prepared by anodic oxidation. J Mater Res 2001;16:3331–4.

[297] Paulose M, Prakasam HE, Varghese OK, et al. TiO_2 Nanotube arrays of 1000 μm length by anodization of titanium foil: phenol red diffusion. J Phys Chem C 2007;111:14992–7.

[298] Assefpour-Dezfuly M, Vlachos C, Andrews EH. Oxide morphology and adhesive bonding on titanium surfaces. J Mater Sci 1984;19:3626–39.

[299] Zwilling V, Darque-Ceretti E, Boutry-Forveille A, et al. Structure and physicochemistry of anodic oxide films on titanium and TA6V alloy. Surf Interface Anal 1999;27:629–37.

[300] Macak JM, Tsuchiya H, Ghicov A, et al. TiO_2 nanotubes: self-organized electrochemical formation, properties and applications. Curr Opin Solid State Mater 2007;11:3–18.

[301] Varghese OK, Paulose M, Grimes CA. Long vertically aligned titania nanotubes on transparent conducting oxide for highly efficient solar cells. Nat Nanotechnol 2009;4:592–7.

[302] Zhang ZH, Wang P. Optimization of photoelectrochemical water splitting performance on hierarchical TiO_2 nanotube arrays. Energy Environ Sci 2012;5:6506–12.

[303] Wu H, Zhang Z. High photoelectrochemical water splitting performance on nitrogen doped double-wall TiO_2 nanotube array electrodes. Int J Hydrog Energy 2011;36:13481–7.

[304] Sun L, Cai J, Wu Q, et al. N-doped TiO_2 nanotube array photoelectrode for visible-light-induced photoelectrochemical and photoelectrocatalytic activities. Electrochim Acta 2013;108:525–31.

[305] Beranek R, Kisch H. Tuning the optical and photoelectrochemical properties of surface-modified TiO_2. Photochem Photobiol Sci 2008;7:40–8.

[306] Beranek R, Kisch H. Surface-modified anodic TiO_2 films for visible light photocurrent response. Electrochem Commun 2007;9:761–6.

[307] Mor G, Prakasam H, Varghese O, et al. Vertically oriented Ti−Fe−O nanotube array films: toward a useful material architecture for solar spectrum water photoelectrolysis. Nano Lett 2007;7:2356–64.

[308] Park JH, Kim S, Bard AJ. Novel carbon-doped TiO_2 nanotube arrays with high aspect ratios for efficient solar water splitting. Nano Lett 2006;6:24–8.

[309] Yamaki T, Umebayashi T, Sumita T, et al. Fluorine-doping in titanium dioxide by ion implantation technique. Nucl Instrum Methods Phys Res Sect B Beam Interact Mater Atoms 2003;206:254–8.

[310] Ohno T, Mitsui T, Matsumura M. Photocatalytic activity of S-doped TiO_2 photocatalyst under visible light. Chem Lett 2003;32:364–5.

[311] Zhao W, Ma W, Chen C, et al. Efficient degradation of toxic organic pollutants with Ni_2O_3/$TiO_{2-x}B_x$ under visible irradiation. J Am Chem Soc 2004;126:4782–3.

[312] Anpo M. Photocatalysis on titanium oxide catalysts: approaches in achieving highly efficient reactions and realizing the use of visible light. Catal Surv Asia 1997;1:169–79.

[313] Momeni MM, Ghayeb Y, Ghonchegi Z. Fabrication and characterization of copper doped TiO_2 nanotube arrays by in situ electrochemical method as efficient visible-light photocatalyst. Ceram Int 2015;41:8735–41.
[314] Ghicov A, Schmidt B, Kunze J, et al. Photoresponse in the visible range from Cr doped TiO_2 nanotubes. Chem Phys Lett 2007;433:323–6.
[315] Momeni MM, Ghayeb Y. Photoelectrochemical water splitting on chromium-doped titanium dioxide nanotube photoanodes prepared by single-step anodizing. J Alloys Compds 2015;637:393–400.
[316] Allam NK, Poncheri AJ, El-Sayed MA. Vertically oriented Ti–Pd mixed oxynitride nanotube arrays for enhanced photoelectrochemical water splitting. ACS Nano 2011;5:5056–66.
[317] Paramasivam I, Macak JM, Schmuki P. Photocatalytic activity of TiO_2 nanotube layers loaded with Ag and Au nanoparticles. Electrochem Commun 2008;10:71–5.
[318] Lee K, Hahn R, Altomare M, et al. Intrinsic Au decoration of growing TiO_2 nanotubes and formation of a high-efficiency photocatalyst for H_2 production. Adv Mater 2013;25:6133–7.
[319] Nguyen NT, Altomare M, Yoo J, et al. Efficient photocatalytic H_2 evolution: controlled dewetting–dealloying to fabricate site-selective high-activity nanoporous Au particles on highly ordered TiO_2 nanotube Arrays. Adv Mater 2015;27:3208–15.
[320] Liu Z, Hou W, Pavaskar P, et al. Plasmon resonant enhancement of photocatalytic water splitting under visible illumination. Nano Lett 2011;11:1111–6.
[321] Wang H, You T, Shi W, et al. Au/TiO_2/Au as a plasmonic coupling photocatalyst. J Phys Chem C 2012;116:6490–4.
[322] Ge M-Z, Cao C-Y, Li S-H, et al. In situ plasmonic Ag nanoparticle anchored TiO_2 nanotube arrays as visible-light-driven photocatalysts for enhanced water splitting. Nanoscale 2016;8:5226–34.
[323] Sun L, Li J, Wang C, et al. Ultrasound aided photochemical synthesis of Ag loaded TiO_2 nanotube arrays to enhance photocatalytic activity. J Hazard Mater 2009;171:1045–50.
[324] Wu F, Hu X, Fan J, et al. Photocatalytic activity of Ag/TiO_2 nanotube arrays enhanced by surface plasmon resonance and application in hydrogen evolution by water splitting. Plasmonics 2013;8:501–8.
[325] Zhang L, Pan N, Lin S. Influence of Pt deposition on water-splitting hydrogen generation by highly-ordered TiO_2 nanotube arrays. Int J Hydrog Energy 2014;39:13474–80.
[326] Ye M, Gong J, Lai Y, et al. High-efficiency photoelectrocatalytic hydrogen generation enabled by palladium quantum dots-sensitized TiO_2 nanotube arrays. J Am Chem Soc 2012;134:15720–3.
[327] Zhang X, Wang F, Huang H, et al. Carbon quantum dot sensitized TiO_2 nanotube arrays for photoelectrochemical hydrogen generation under visible light. Nanoscale 2013;5:2274–8.
[328] Song P, Zhang X, Sun M, et al. Graphene oxide modified TiO_2 nanotube arrays: enhanced visible light photoelectrochemical properties. Nanoscale 2012;4:1800–4.
[329] Feng S, Yang J, Zhu H, et al. Synthesis of single crystalline anatase TiO_2 (0 0 1) tetragonal nanosheet-array films on fluorine-doped tin oxide substrate. J Am Chem Soc 2011;94:310–5.
[330] Wu J, Yu C. Aligned TiO_2 nanorods and nanowalls. J Phys Chem B 2004;108:113377–9.
[331] Hoang S, Berglund SP, Fullon RR, et al. Chemical bath deposition of vertically aligned TiO_2 nanoplatelet arrays for solar energy conversion applications. J Mater Chem A 2013;1:4307–15.
[332] Steinmiller EM, Choi KS. Photochemical deposition of cobalt-based oxygen evolving catalyst on a semiconductor photoanode for solar oxygen production. Proc Natl Acad Sci USA 2009;106:20633–6.
[333] Wang M, Ren F, Zhou J, et al. N doping to ZnO nanorods for photoelectrochemical water splitting under visible light: engineered impurity distribution and terraced band structure. Sci Rep 2015;5:12925.
[334] Allami S, Abid Ali ZD, Li Y, et al. Photoelectrochemical performance of N-doped ZnO branched nanowire photoanodes. Heliyon 2017;3:e00423.
[335] Khan A, Ahmed MI, Adam A, et al. A novel fabrication methodology for sulfur-doped ZnO nanorods as an active photoanode for improved water oxidation in visible-light regime. Nanotechnology 2017;28:055602.
[336] Sharma A, Chakraborty M, Thangavel R, et al. Hydrothermal growth of undoped and boron doped ZnO nanorods as a photoelectrode for solar water splitting applications. J Sol-Gel Sci Technol 2018;85:1–11.
[337] Lee WC, Canciani GE, Alwhshe BO, et al. Enhanced photoelectrochemical water oxidation by Zn_xM_yO (M = Ni Co, K, Na) nanorod arrays. Int J Hydrog Energy 2016;41:123–31.
[338] Qiu Z, Yang X, Han J, et al. Sodium-doped ZnO nanowires grown by high-pressure PLD and their acceptor-related optical properties. J Am Ceram Soc 2014;97:2177–84.
[339] Patel PP, Hanumantha PJ, Velikokhatnyi OI, et al. Nitrogen and cobalt co-doped zinc oxide nanowires – viable photoanodes for hydrogen generation via photoelectrochemical water splitting. J Power Sources 2015;299:11–24.
[340] Chakraborty M, Mahapatra P, Thangavel R. Hydrothermal growth and conductivity enhancement of (Al, Cu) co-doped ZnO nanorods thin films. AIP Conf Proc 2016;1731:120004.
[341] Wei YF, Ke L, Kong JH, et al. Enhanced photoelectrochemical water-splitting effect with a bent ZnO nanorod photoanode decorated with Ag nanoparticles. Nanotechnology 2012;23:235401.
[342] Moakhar RS, Kushwaha A, Jalali M, et al. Enhancement in solar driven water splitting by Au–Pd nanoparticle decoration of electrochemically grown ZnO nanorods. J Appl Electrochem 2016;46:819–27.
[343] Wang T, Lv R, Zhang P, et al. Au nanoparticle sensitized ZnO nanopencil arrays for photoelectrochemical water splitting. Nanoscale 2015;7:77–81.
[344] Chen HM, Chen CK, Chen C-J, et al. Plasmon inducing effects for enhanced photoelectrochemical water splitting: X-ray absorption approach to electronic structures. ACS Nano 2012;6:7362–72.
[345] Thiyagarajan P, Ahn H-J, Lee J-S, et al. Hierarchical metal/semiconductor nanostructure for efficient water splitting. Small 2013;9:2341–7.
[346] Hsu Y-K, Fu S-Y, Chen M-H, et al. Facile synthesis of Pt nanoparticles/ZnO nanorod arrays for photoelectrochemical water splitting. Electrochim Acta 2014;120:1–5.
[347] Chen HM, Chen CK, Chang Y-C, et al. Quantum dot monolayer sensitized ZnO nanowire-array photoelectrodes: true efficiency for water splitting. Angew Chem Int Ed 2010;49:5966–9.
[348] Liu Z-Q, Xie X-H, Xu Q-Z, et al. Electrochemical synthesis of ZnO/CdTe core-shell nanotube arrays for enhanced photoelectrochemical properties. Electrochim Acta 2013;98:268–73.
[349] Hsu Y-K, Chen Y-C, Lin Y-G. Novel ZnO/Fe_2O_3 core–shell nanowires for photoelectrochemical water splitting. ACS Appl Mater Interfaces 2015;7:14157–62.
[350] Bai Z, Yan X, Kang Z, et al. Photoelectrochemical performance enhancement of ZnO photoanodes from $ZnIn_2S_4$ nanosheets coating. Nano Energy 2015;14:392–400.
[351] Guo CX, Dong Y, Yang HB, et al. Graphene quantum dots as a green sensitizer to functionalize ZnO nanowire arrays on F-doped SnO_2 glass for enhanced photoelectrochemical water splitting. Adv Energy Mater 2013;3:997–1003.
[352] Wang S, Sakurai T, Wen W, et al. Energy level alignment at interfaces in metal halide perovskite solar cells. Adv Mater Interafces 2018;5:1800260.
[353] Shao M, Ning F, Wei M, et al. Hierarchical nanowire arrays based on ZnO core-layered double hydroxide shell for largely enhanced photoelectrochemical water splitting. Adv Funct Mater 2014;24:580–6.
[354] Sun X, Li Q, Jiang J, et al. Morphology-tunable synthesis of ZnO nanoforest and its photoelectrochemical performance. Nanoscale 2014;6:8769–80.
[355] Kalanur SS, Hwang YJ, Chae SY, et al. Facile growth of aligned WO_3 nanorods on FTO substrate for enhanced photoanodic water oxidation activity. J Mater Chem A 2013;1:3479–88.
[356] Ding J-R, Kim K-S. Facile growth of 1-D nanowire-based WO_3 thin films with enhanced photoelectrochemical performance. AIChE J 2016;62:421–8.
[357] Kafizas A, Francàs L, Sotelo-Vazquez C, et al. Optimizing the activity of nanoneedle structured WO_3 photoanodes for solar water splitting: direct synthesis via chemical vapor deposition. J Phys Chem C 2017;121:5983–93.
[358] Zhang T, Wang L, Su J, et al. Branched tungsten oxide nanorod arrays synthesized by controlled phase transformation for solar water oxidation. ChemCatChem 2016;8:2119–27.
[359] Liu Y, Zhao L, Su J, et al. Fabrication and properties of a branched $(NH_4)_xWO_3$ nanowire array film and a porous WO_3 nanorod array film. ACS Appl Mater Interfaces 2015;7:3532–8.
[360] Wang GM, Ling YC, Wang HY, et al. Hydrogen-treated WO_3 nanoflakes show enhanced photostability. Energy Environ Sci 2012;5:6180–7.
[361] Amano F, Li D, Ohtani B. Fabrication and photoelectrochemical property of tungsten(vi) oxide films with a flake-wall structure. Chem Commun 2010;46:2769–71.
[362] Zhang J, Ling Y, Gao W, et al. Enhanced photoelectrochemical water splitting on novel nanoflake WO_3 electrodes by dealloying of amorphous Fe–W alloys. J Mater Chem A 2013;1:10677–85.
[363] Yu SQ, Ling Y, Zhang J, et al. Efficient photoelectrochemical water splitting and impedance analysis of WO_{3-x} nanoflake electrodes. Int J Hydrog Energy 2017;42:20879–87.
[364] Wang S, Chen H, Gao G, et al. Synergistic crystal facet engineering and structural control of WO_3 films exhibiting unprecedented photoelectrochemical performance. Nano Energy 2016;24:94–102.
[365] Wang N, Wang D, Li M, et al. Photoelectrochemical water oxidation on photoanodes fabricated with hexagonal nanoflower and nanoblock WO_3. Nanoscale 2014;6:2061–6.
[366] Balandeh M, Mezzetti A, Tacca A, et al. Quasi-1D hyperbranched WO_3 nanostructures for low-voltage photoelectrochemical water splitting. J Mater Chem A 2015;3:6110–7.
[367] Shin S, Han H, Kim J, et al. A tree-like nanoporous WO_3 photoanode with enhanced charge transport efficiency for photoelectrochemical water oxidation. J Mater Chem A 2015;3:12920–6.
[368] Pala RA, Leenheer AJ, Lichterman M, et al. Measurement of minority-carrier diffusion lengths using wedge-shaped semiconductor photoelectrodes. Energy Environ Sci 2014;7:3424–30.
[369] Kang D, Park Y, Hill JC, et al. Preparation of Bi-based ternary oxide photoanodes $BiVO_4$, Bi_2WO_6, and $Bi_2Mo_3O_{12}$ using dendritic Bi metal electrodes. J Phys Chem Lett 2014;5:2994–9.
[370] Liu C, Su J, Zhou J, et al. A multistep ion exchange approach for fabrication of porous $BiVO_4$ nanorod arrays on transparent conductive substrate. ACS Sust Chem Eng 2016;4:4492–7.
[371] Li H, Sun Y, Cai B, et al. Hierarchically Z-scheme photocatalyst of Ag@AgCl decorated on $BiVO_4$ (040) with enhancing photoelectrochemical and photocatalytic performance. Appl Catal B Environ 2015;170–171:206–14.

[372] Xi G, Ye J. Synthesis of bismuth vanadate nanoplates with exposed 0 0 1 facets and enhanced visible-light photocatalytic properties. Chem Commun 2010;46:13–5.
[373] Li J, Zhou J, Hao H, et al. Exposed specific (0 4 0) and (1 1 0) facets of $BiVO_4$ with Bi_2WO_6 nanoparticles for enhanced photocatalytic performance. New J Chem 2017;41:6922.
[374] Kim CW, Son YS, Kang MJ, et al. (0 4 0)-Crystal facet engineering of $BiVO_4$ plate photoanodes for solar fuel production. Adv Energy Mater 2016;6:1501754.
[375] Xia LG, Li JH, Bai J, et al. $BiVO_4$ photoanode with exposed (0 4 0) facets for enhanced photoelectrochemical performance. Nano-Micro Lett 2017;10:11.
[376] Wang S, Chen P, Yun J-H, et al. An electrochemically treated $BiVO_4$ photoanode for efficient photoelectrochemical water splitting. Angew Chem Int Ed 2017;56:8500–4.
[377] Gao B, Wang T, Fan X, et al. Selective deposition of Ag_3PO_4 on specific facet of $BiVO_4$ nanoplate for enhanced photoelectrochemical performance. Solar RRL 2018;2:1800102.
[378] Kalanoor BS, Seo H, Kalanur SS. Recent developments in photoelectrochemical water-splitting using $WO_3/BiVO_4$ heterojunction photoanode: a review. Mater Sci Energy Technol 2018;1:49–62.
[379] Chatchai P, Murakami Y, Kishioka S, et al. Efficient photocatalytic activity of water oxidation over $WO_3/BiVO_4$ composite under visible light irradiation. Electrochim Acta 2009;54:1147–52.
[380] Su J, Guo L, Bao N, et al. Nanostructured $WO_3/BiVO_4$ heterojunction films for efficient photoelectrochemical water splitting. Nano Lett 2011;11:1928–33.
[381] Pilli SK, Janarthanan R, Deutsch TG, et al. Efficient photoelectrochemical water oxidation over cobalt-phosphate (Co-Pi) catalyst modified $BiVO_4$/1D-WO_3 heterojunction electrodes. Phys Chem Chem Phys 2013;15:14723–8.
[382] Pihosh Y, Turkevych I, Mawatari K, et al. Nanostructured $WO_3/BiVO_4$ photoanodes for efficient photoelectrochemical water splitting. Small 2014;10:3692–9.
[383] Pihosh Y, Turkevych I, Mawatari K, et al. Photocatalytic generation of hydrogen by core-shell $WO_3/BiVO_4$ nanorods with ultimate water splitting efficiency. Sci Rep 2015;5:11141.
[384] Shi X, Choi IY, Zhang K, et al. Efficient photoelectrochemical hydrogen production from bismuth vanadate-decorated tungsten trioxide helix nanostructures. Nat Commun 2014;5:4775.
[385] Zeng Q, Li J, Li L, et al. Synthesis of $WO_3/BiVO_4$ photoanode using a reaction of bismuth nitrate with peroxovanadate on WO_3 film for efficient photoelectrocatalytic water splitting and organic pollutant degradation. Appl Catal B Environ 2017;217:21–9.
[386] Marusak LA, Messier R, White WB. Optical absorption spectrum of hematite, α-Fe_2O_3 near IR to UV. J Phys Chem Solids 1980;41:981–4.
[387] Sivula K, Le Formal F, Grätzel M. Solar water splitting: progress using hematite (α-Fe_2O_3) photoelectrodes. ChemSusChem 2011;4:432–49.
[388] Vayssieres L, Beermann N, Lindquist S-E, et al. Controlled aqueous chemical growth of oriented three-dimensional crystalline nanorod arrays: application to iron(III) oxides. Chem Mater 2001;13:233–5.
[389] Beermann N, Vayssieres L, Lindquist SE, et al. Photoelectrochemical studies of oriented nanorod thin films of hematite. J Electrochem Soc 2000;147:2456–61.
[390] Lindgren T, Wang H, Beermann N, et al. Aqueous photoelectrochemistry of hematite nanorod array. Sol Energy Mater Sol C 2002;71:231–43.
[391] Kennedy JH, Frese KW. Photooxidation of water at α-Fe_2O_3 electrodes. J Electrochem Soc 1978;125:709–14.
[392] Bjoerksten U, Moser J, Graetzel M. Photoelectrochemical studies on nanocrystalline hematite films. Chem Mater 1994;6:858–63.
[393] Xi L, Chiam SY, Mak WF, et al. A novel strategy for surface treatment on hematite photoanode for efficient water oxidation. Chem Sci 2013;4:164–9.
[394] Ling Y, Wang G, Reddy J, et al. The influence of oxygen content on the thermal activation of hematite nanowires. Angew Chem Int Ed 2012;124:4150–5.
[395] Ferraz LC, Carvalho Jr WM, Criado D, et al. Vertically oriented iron oxide films produced by hydrothermal process: effect of thermal treatment on the physical chemical properties. ACS Appl Mater Interfaces 2012;4:5515–23.
[396] Thimsen E, Formal F, Grätzel M, et al. Influence of plasmonic Au nanoparticles on the photoactivity of Fe_2O_3 electrodes for water splitting. Nano Lett 2011;11:35–43.
[397] Mao A, Han GY, Park JH. Synthesis and photoelectrochemical cell properties of vertically grown α-Fe_2O_3 nanorod arrays on a gold nanorod substrate. J Mater Chem 2010;20:2247–50.
[398] Spray RL, Choi K-S. Photoactivity of transparent nanocrystalline Fe_2O_3 electrodes prepared via anodic electrodeposition. Chem Mater 2009;21:3701–9.
[399] Wang D, Chen H, Chang G, et al. Uniform doping of titanium in hematite nanorods for efficient photoelectrochemical water splitting. ACS Appl Mater Interfaces 2015;7:14072–8.
[400] Li Q, Bian J, Zhang N, et al. Loading $Ni(OH)_2$ on the Ti-doped hematite photoanode for photoelectrochemical water splitting. Electrochim Acta 2015;155:383–90.
[401] Fu Z, Jiang T, Liu Z, et al. Highly photoactive Ti-doped α-Fe_2O_3 nanorod arrays photoanode prepared by a hydrothermal method for photoelectrochemical water splitting. Electrochim Acta 2014;129:358–63.
[402] Bohn CD, Agrawal AK, Walter EC, et al. Effect of tin doping on α-Fe_2O_3 photoanodes for water splitting. J Phys Chem C 2012;116:15290–6.
[403] Ling Y, Li Y. Review of Sn-doped hematite nanostructures for photoelectrochemical water splitting. Part Part Syst Charact 2014;31:1113–21.
[404] Tamirat AG, Su W-N, Dubale AA, et al. Photoelectrochemical water splitting at low applied potential using a NiOOH coated codoped (Sn, Zr) α-Fe_2O_3 photoanode. J Mater Chem A 2015;3:5949–61.
[405] Park S, Kim HJ, Lee CW, et al. Sn self-doped α-Fe_2O_3 nanobranch arrays supported on a transparent, conductive SnO_2 trunk to improve photoelectrochemical water oxidation. Int J Hydrog Energy 2014;39:16459–67.
[406] Annamalai A, Shinde PS, Jeon TH, et al. Fabrication of superior α-Fe_2O_3 nanorod photoanodes through ex-situ Sn-doping for solar water splitting. Sol Energy Mater Sol C 2016;144:247–55.
[407] Ling Y, Wang G, Wheeler DA, et al. Sn-doped hematite nanostructures for photoelectrochemical water splitting. Nano Lett 2011;11:2119–25.
[408] Lukowski MA, Jin S. Improved synthesis and electrical properties of Si-doped α-Fe_2O_3 nanowires. J Phys Chem C 2011;115:12388–95.
[409] Liu J, Cai YY, Tian ZF, et al. Highly oriented Ge-doped hematite nanosheet arrays for photoelectrochemical water oxidation. Nano Energy 2014;9:282–90.
[410] Zhang R, Yang L, Huang X, et al. Se doping: an effective strategy toward Fe_2O_3 nanorod arrays for greatly enhanced solar water oxidation. J Mater Chem A 2017;5:12086–90.
[411] Fu Y, Dong C-L, Zhou Z, et al. Solution growth of Ta-doped hematite nanorods for efficient photoelectrochemical water splitting: a tradeoff between electronic structure and nanostructure evolution. Phys Chem Chem Phys 2016;18:3846–53.
[412] Chang HW, Fu YM, Lee WY, et al. Visible light-induced electronic structure modulation of Nb- and Ta-doped α-Fe_2O_3 nanorods for effective photoelectrochemical water splitting. Nanotechnology 2018;29:064002.
[413] Shen S, Kronawitter CX, Jiang J, et al. Surface tuning for promoted charge transfer in hematite nanorod arrays as water-splitting photoanodes. Nano Res 2012;5:327–36.
[414] Shen S, Guo P, Wheeler DA, et al. Physical and photoelectrochemical properties of Zr-doped hematite nanorod arrays. Nanoscale 2013;5:9867–74.
[415] Badia-Bou L, Mas-Marza E, Rodenas P, et al. Water oxidation at hematite photoelectrodes with an iridium-based catalyst. J Phys Chem C 2013;117:3826–33.
[416] Tilley SD, Cornuz M, Sivula K, et al. Light-induced water splitting with hematite: improved nanostructure and iridium oxide catalysis. Angew Chem Int Ed 2010;49:6405–8.
[417] Fu L, Yu H, Zhang C, et al. Cobalt phosphate group modified hematite nanorod array as photoanode for efficient solar water splitting. Electrochim Acta 2014;136:363–9.
[418] Klahr B, Gimenez S, Fabregat-Santiago F, et al. Photoelectrochemical and impedance spectroscopic investigation of water oxidation with "Co–Pi"-coated hematite electrodes. J Am Chem Soc 2012;134:16693–700.
[419] Wang Z, Liu G, Ding C, et al. Synergetic effect of conjugated $Ni(OH)_2/IrO_2$ cocatalyst on titanium-doped hematite photoanode for solar water splitting. J Phys Chem C 2015;119:19607–12.
[420] Xu Z, Fan Z, Shi Z, et al. Interface manipulation to improve plasmon-coupled photoelectrochemical water splitting on α-Fe_2O_3 photoanodes. ChemSusChem 2018;11:237–44.
[421] Fan HM, You GJ, Li Y, et al. Shape-controlled synthesis of single-crystalline Fe_2O_3 hollow nanocrystals and their tunable optical properties. J Phys Chem C 2009;113:9928–35.
[422] Lu J, Qi D, Deng C, et al. Hydrothermal synthesis of α-Fe_2O_3@SnO_2 core–shell nanotubes for highly selective enrichment of phosphopeptides for mass spectrometry analysis. Nanoscale 2010;2:1892–900.
[423] Jia C-J, Sun L-D, Yan Z-G, et al. Single-crystalline iron oxide nanotubes. Angew Chem Int Ed 2005;44:4328–33.
[424] Shen XP, Liu HJ, Pan L, et al. An efficient template pathway to synthesis of ordered metal oxide nanotube arrays using metal acetylacetonates as single-source molecular precursors. Chem Lett 2004;33:1128–9.
[425] Rangaraju RR, Panday A, Raja KS, et al. Nanostructured anodic iron oxide film as photoanode for water oxidation. J Phys D Appl Phys 2009;42:135303.
[426] Mohapatra SK, John SE, Banerjee S, et al. Water photooxidation by smooth and ultrathin α-Fe_2O_3 nanotube arrays. Chem Mater 2009;21:3048–55.
[427] LaTempa TJ, Feng X, Paulose M, et al. Temperature-dependent growth of self-assembled hematite (α-Fe_2O_3) nanotube arrays: rapid electrochemical synthesis and photoelectrochemical properties. J Phys Chem C 2009;113:16293–8.
[428] Prakasam HE, Varghese OK, Paulose M, et al. Synthesis and photoelectrochemical properties of nanoporous iron (III) oxide by potentiostatic anodization. Nanotechnology 2006;17:4285.
[429] Qi X, She G, Wang M, et al. Electrochemical synthesis of p-type Zn-doped α-Fe_2O_3 nanotube arrays for photoelectrochemical water splitting. Chem Commun 2013;49:5742–4.
[430] Cesar I, Kay A, Gonzalez Martinez JA, et al. Translucent thin film Fe_2O_3 photoanodes for efficient water splitting by sunlight: nanostructure-directing effect of Si-doping. J Am Chem Soc 2006;128:4582–3.
[431] Kay A, Cesar I, Grätzel M. New benchmark for water photooxidation by nanostructured α-Fe_2O_3 films. J Am Chem Soc 2006;128:15714–21.
[432] Warren SC, Voitchovsky K, Dotan H, et al. Identifying champion nanostructures for solar water-splitting. Nat Mater 2013;12:842–9.

[433] Duret A, Grätzel M. Visible light-induced water oxidation on mesoscopic α-Fe_2O_3 films made by ultrasonic spray pyrolysis. J Phys Chem B 2005;109:17184–91.
[434] Chen H, Hu LF, Fang XS, et al. General fabrication of monolayer SnO_2 nanonets for high-performance ultraviolet photodetectors. Adv Funct Mater 2012;22:1229–35.
[435] Lin HY, Yang HC, Wang WL. Synthesis of mesoporous Nb_2O_5 photocatalysts with Pt, Au, Cu and NiO cocatalyst for water splitting. Catal Today 2011;174:106–13.

Yongcai Qiu is a Professor at School of Environment and Energy, South China University of Technology. He received his Ph.D. degree (2012) in the Nano Science and Technology Program at Hong Kong University of Science and Technology (HKUST). He then did his postdoctoral research at HKUST in 2013–2014 and joint postdoctoral research at Chinese Academy of Sciences and Stanford University in 2015–2016. His current research interests cover the preparation, understanding, and applications of functional nanomaterials in energy storage and conversion devices.

Lin Guo is a professor and vice dean of School of Chemistry and Environment in Beihang University. He received his Ph.D. degree in Materials Science and Engineering from Beijing University of Institute of Technology (BIT) in 1997. He worked as a visiting scholar in Hong Kong University of Science and Technology (HKUST) in 1999. He worked in Dresden Technology University with Humboldt Fellowship for 2 years. His research interests include synthesis and characterization of sophisticated nanomaterials, high-strength nanomaterials with light weight and functional nanomaterials for energy storage.

Zhiyong Fan received his B.S. and M.S. degrees in Physical Electronics from Fudan University, Shanghai, China, in 1998 and 2001. He received his Ph.D. degree from the University of California, Irvine, in 2006 in Materials Science. From 2007 to 2010 he worked in the University of California, Berkeley, as a postdoctoral fellow in the Department of Electrical Engineering and Computer Sciences, with a joint appointment with Lawrence Berkeley National Laboratory. In May 2010, he joined Hong Kong University of Science and Technology as an assistant professor. His research interests include engineering novel nanostructures with functional materials, for technological applications including energy conversation, electronics and sensors, etc.

Shihe Yang is a full Professor at The Hong Kong University of Science and Technology and Peking University Shenzhen Graduate school. His long-standing interest spans chemistry, physics, and functions of multiscale material systems encom-passing, inter alia, molecular, nanoscopic, and mesoscopic regimes. His current research interest is focused on energy material science, technology and physical chemistry by drawing on the understanding, manipulation and applications of low-dimensional materials.